Electrochemical Impedance Spectroscopy on ageing Lithium-Ion Batteries

Von der Fakultät für Maschinenbau
der Technischen Universität Carolo-Wilhelmina zu Braunschweig
zur Erlangung der Würde
eines Doktor-Ingenieurs (Dr.-Ing.)
genehmigte Dissertation

von: Marco Heinrich
aus (Geburtsort): Göttingen

eingereicht am: 19.03.2020
mündliche Prüfung am: 13.07.2020

Gutachter: Prof. Dr.-Ing. Ulrike Krewer,
Prof. Dr. rer nat. habil. Uwe Schröder

2020

Acknowledgements

Being able to finish a PhD thesis requires suitable conditions: Initially, I had the privilege to be born in a rich country and being raised in a wonderful family by parents who supported my education and enabled me to evolve freely. Secondly, significant progress during scientific work is not possible without mentoring. In my case Professor Ulrike Krewer and Dr.-Ing. Steffen Seitz have pushed me forward whenever their limited time allowed it. Last but not least, the personal and working environment has a significant impact on success or failure. I was lucky to find encouragement by my best friends Uta and Patrick Poggemann during my free time and also lucky to be part of two working groups which supported me in many ways: Fridolin Röder, Vincent Laue and Nina Harting often helped me during scientific discussions and without Ralf Eberhardt I would not have been able to set up my measurements. Nicolas Wolff not only helped me whenever I faced an scientific issue but also became a good friend. Without Nico and our cooperative work this thesis probably would not exist. Thanks to everyone else in the working groups who are not named personally and to Thore Peyk, Nathalie Szycher and Maren Hain who will save the world with me some day.

Abstract

The change of **L**ithium-**i**on **B**attery (LiB) model parameters during cyclic ageing is analysed in order to relate it to the capacity of the cell. Therefore, approaches to distinguish between anode and cathode contributions to the full cell impedance spectrum are developed. The results from a new measurement routine, using temperature gradients across a full cell, show that a successful assignment of the charge transfer processes at the cathode and anode is possible. For the analysed cell the cathode charge transfer processes occur at a lower time constant than the related anode processes. With the information of such an assignment, ageing of a 30 mAh pouch cell is analysed with **E**lectrochemical **I**mpedance **S**pectroscopy (EIS). A Newman-type LiB-model for this cell is extended by a physical ageing model including a **S**olid **E**lectrolyte **I**terphase (SEI), loss of active surface area and loss of active material. The simulation results of this model in combination with the related measurement results are used with a parameter identification algorithm to quantify the thickness of the SEI, the amount of isolated surface area and the loss of active material. The results show that the impedance increase is caused by a decrease of active surface area while the capacity decrease is caused by a loss of active material at the anode and cathode. The SEI thickness has found to increase to 45 nm while the active surface areas of the anode and cathode decrease by 20% and 57% respectively until the **E**nd **O**f **L**ife (EOL) of the cell after 400 cycles. The change of the ageing parameters occurs in correlation to the decrease of the capacity of the analysed cell. Finally, the identifiability of kinetic, transport and ageing parameters, identified using this approach, has been quantified using **F**isher-**I**nformation-**M**atrices (FIMs) showing that the impedance spectra are sensitive enough to the ageing parameters to ensure their precise identifiability.

Kurzfassung

Die Veränderung von Parametern eines Lithium-Ionen Batteriemodels während zyklischer Alterung wird analysiert, um Rückschlüsse auf die Kapazität der Zelle zu ziehen. Hierfür werden Ansätze vorgestellt, die es ermöglichen zwischen den Beiträgen von Anode und Kathode zur Vollzellimpedanz zu unterscheiden. Die Ergebnisse einer neuen Messroutine, bei der ein Temperaturgradient auf die Vollzelle aufgeprägt wird, zeigen, dass eine erfolgreiche Zuordnung der Ladungstransferprozesse an Anode und Kathode möglich ist. Für die untersuchte Zelle finden die Ladungstransferprozesse an der Kathode mit einer kleineren Zeitkonstante statt als die entsprechenden Prozesse an der Anode. Mit der Information einer solchen Zuordnung wird die Alterung einer 30 mAh Pouchzelle mit der **E**lektrochemischen **I**mpedanz **S**pektroskopie (EIS) analysiert. Hierfür wird ein Newman-Model einer LiB um ein physikalisches Alterungsmodel erweitert, das eine **S**olid **E**lectrolyte **I**nterphase (SEI), den Verlust von aktiver Oberfläche und den Verlust von Aktivmaterial enthält. Die Ergebnisse zeigen, dass der Impedanzanstieg durch einen Verlust an aktiver Oberfläche und der Kapazitätsverlust durch einen Verlust an Aktivmaterial in Anode und Kathode verursacht wird. Bis zum Ende der Lebensdauer der Batterie nach 400 Zyklen, erhöht sich die Dicke der SEI auf 45 nm, während die aktiven Oberflächen von Anode und Kathode um 20% und 57% abnehmen. Die Veränderung der Alterungsparameter ist bei der untersuchten Zelle mit der Abnahme der Zellkapazität korreliert. Abschließend wurde die Identifizierbarkeit von kinetischen-, Transport- und Alterungsparametern mathematisch mit Fischerinformationsmatrizen untersucht und gezeigt, dass die Impedanzspektren sensitiv genug auf eine Änderung der Alterungsparameter reagieren, um diese präzise zu identifizieren.

Publications within Research of this Thesis

Journal Publications

- M. Heinrich, N. Wolff, N. Harting, V. Laue, F. Röder and U. Krewer, "Physico-Chemical Modeling of a Lithium-Ion Battery: An Ageing Study with Electrochemical Impedance Spectroscopy," *Batteries and Supercaps*, vol. 2, pp. 530-540, 2019

- M. Heinrich, N. Wolff, S. Seitz and U. Krewer, "Identifying anode and cathode contributions to Li-Ion full cell impedance spectra," *in preparation*

- N. Wolff, N. Harting, M. Heinrich, F. Röder and U. Krewer, "Nonlinear Frequency Response Analysis on Lithium-Ion Batteries: A Model-Based Assessment," *Electrochimica Acta*, no. 260, pp. 614-622, 2018

- N. Wolff, N. Harting, M. Heinrich, U. Krewer, "Nonlinear Frequency Response Analysis on Lithium-Ion Batteries: Process Identification and Differences between Transient and Steady-State Behaviour," *Electrochimica Acta*, vol. 298, pp. 788-798, 2019

- N. Wolff, N. Harting, F. Röder, M. Heinrich and U. Krewer, "Understanding nonlinearities in electrochemical systems," *The European Physical Journal Special Topics*, vol. 227, no. 18, pp. 2617-2640, 2019

Conference Contributions

- Heinrich, M., Röder, F, Wolff, N., Seitz, S., Krewer, U.
  Parameter sensitivity analysis of EIS in full cell batteries based on electrochemical modeling, Presentation, *10th International Symposium on Electrochemical Impedance Spectroscopy*, 2016

- Heinrich, M., Wolff, N, Heine, J., Seitz, S., Krewer, U.
  Ageing induced changes of charge distributions in a LIB analysed by correlating EIS simulations and experiments, Presentation, *14th Symposium on Fuel Cell and Battery Modelling and Experimental Validation*, 2017

Contents

List of Figures

List of Tables

1 Introduction

Electrochemical **I**mpedance **S**pectroscopy (EIS) is a non-destructive measurement technique which enables insight into electrochemical systems such as **L**ithium-**i**on **B**atteries (LiBs). Being able to relate the change of an impedance spectrum of a LiB during ageing to the actual **S**tate **o**f **H**ealth (SoH) of the cell is a huge step to a save usage of LiBs. For example, including an EIS measurement instead of a capacity measurement into the **B**attery **M**anagement **S**ystem (BMS) of an **E**lectric **V**ehicle (EV) would provide a fast option to determine if the LiB is save for further use or if it should be replaced for safety reasons. One important step is to show that there are not only correlations between changes in the impedance spectrum and the SoH of a LiB but also causal connections. As a suitable approach, a model representing the physics within the battery can be set up. If an impedance simulation on such a model can be brought into agreement with a measured spectrum, parameters and equations chosen for the model might represent the examined LiB. Analysing the change of identified parameters during ageing can give insight about the remaining capacity of a cell or even predict the EOL of it. Nevertheless, even if a simulated spectrum matches the measured one, uniqueness of the identified parameters is not necessarily given. Various challenges of EIS have to be overcome before the identified parameters can be verified. The first issue which applies is the fact that processes in anode and cathode of LiBs usually occur at similar characteristic time constants which makes a separation and assignment of their impact on the impedance spectrum difficult or even impossible. Therefore, changes in the impedance spectrum during ageing can not be assigned to anode or cathode parameters unambiguously. Sections 3.1 and 3.2 of this thesis elucidate these issues and chapter 4 demonstrates an approach to overcome them. The second issue applies for the feasibility to identify unknown parameters using impedance data. If a parameter does not sufficiently affect the impedance

spectrum or if another parameter affects the spectrum in a similar way, parameter identification might not be possible. In order to evaluate the identifiability of parameters Fisher Information Matrices have been calculated and evaluated. Conclusively, the research summarised in this thesis shows specific scenarios where the current challenges of EIS, when it is applied to LiBs to relate the change of impedance spectra during ageing to the current SoH, can be overcome and how they can be overcome. Chapter 2 briefly summarises the fundamentals of LiBs and EIS. Afterwards, chapter 3 outlines the challenges of EIS and highlights the scope of this thesis. In chapter 4, a measurement set-up and routine is introduced to overcome the main issue of overlapping impedance contributions of anode and cathode to the full cell spectrum. Based on a possible assignment of anode and cathode contributions to the impedance spectrum, parameter identification is performed in chapter 5. A new detailed ageing model is introduced to extend the Doyle-Newman model. Ageing parameters of this model are determined using a parameter identification algorithm and the change of the identified parameters during cycling of a cell are related to its decreasing SoH. All parameter identifications made in chapter 5 are evaluated mathematically in the last chapter 6 to ensure the identifiability and to quantify the uncertainty of the determined parameters.

In summary, this thesis first outlines how EIS is envisioned to support save usage of LiBs in the near future. Secondly, it describes the challenges of EIS which have to be overcome for an economic and reliable application. A huge part of the thesis deals with possible solutions to overcome the described issues and challenges. One solution is finally applied in order to reliably identify ageing parameters which can be analysed to get insight into the state of LiBs.

2 Fundamentals

This chapter aims to provide a brief overview about the fundamentals for LiBs, EIS and the simulation of EIS with physico-chemical Lithium-ion battery models. First, section 2.1 gives an introduction on LiBs. In the second section 2.2, EIS as a measurement technique to analyse electrochemical systems is explained. In the third section 2.4, the equations used in a physico-chemical battery model and their contribution to the resulting impedance spectra are presented. The last section 2.5 introduces the **F**isher **I**nformation **M**etric (FIM) used for sensitivity analysis.

2.1 Lithium-Ion Batteries

Lithium-ion batteries are everywhere. Almost every rechargeable device currently on the market uses the Lithium-ion technology to store electric energy as chemical energy. Due to their low costs and high energy and power density, LiBs are the state of the art for mobile phones, laptops, cars and many other electrical devices. In the near future, LiBs will most probably also be used to buffer energy produced by renewable energy systems [1].

2.1.1 Materials and Composition

Before discussing materials and composition of LiBs, it is important to note that usually in electrochemistry the electrode where the oxidation reaction takes place is defined as the anode. Vice versa, the electrode where the reduction reaction takes place is defined as the cathode. Since this definition is leading to a varying assignment when switching a LiB from charge to discharge or vice versa, it is common in LiB research to assign the electrode with the lower **O**pen **C**urcuit **V**oltage (OCV) as anode and the electrode with the higher OCV as the cathode.
The first LiB commercially available and produced by Sanyo used lithium

as anode and manganese dioxide as cathode material [1]. During discharge the lithium anode dissolves and the battery can not be charged again (primary battery). A rechargeable (secondary) LiB can be realised if graphite is chosen as anode material which is able to host lithium. Since graphite does not bring any lithium into the system, the cathode has to be exchanged as well. The current state of the art is Lithium-Nickel-Manganese-Cobald (NMC) which, in combination with the graphite anode, enables cell potentials of 2.9 V - 4.2 V. Due to the different potentials of anode and cathode, different materials are used for the related current collectors. For the anode copper is been used, while for the cathode side aluminium is chosen. Between the two electrodes an electrolyte is needed to provide the transport of lithium-ions and to electrically insulate the electrodes from each other. Extensive studies [2, 3, 4] have been conducted to find electrochemically stable electrolytes which, at the same time, have low resistances and low costs. In addition, the composition of the electrolyte has a significant impact on the properties of the layers which form on the electrodes during use [2]. Systems analysed in this work use the common mixture of **E**thylene **C**arbonate (EC) and **D**i**M**ethyl **c**arbonate (DMC) in a weight ratio of 3:7 in which 1 M to 1.2 M lithium-hexafluorophosphate is dissociated into lithium cations and hexafluorophosphate anions. Additionally, a porous separator is used to prevent electrical short circuits between anode and cathode.

2.1.2 Working Principle

If an electrode is placed in an electrolyte, electrochemical double layers charge in order to compensate the difference between the chemical potentials of electrode and electrolyte [5, 6]. Placing two electrodes of different materials or different compositions in the same electrolyte leads to two different potential differences at the electrode-electrolyte interfaces and therefore to an electrical potential between the two electrodes. If the electrolyte and at least one electrode comprises lithium, the electrical potential can be used by connecting both electrodes with an external

conductor. In this case, Lithium in the anode deintercalates into the electrolyte to an lithium ion releasing a free electron which is conducted as electrical current through the external conductor to the cathode where it reacts with an lithium ion during the intercalation of lithium into the cathode. Both reactions and the concluding total reaction are shown in equations 2.1 - 2.3.

$$\text{Cathode side:} \quad \mathrm{Li_{1-x}MO_2} + x\mathrm{Li^+} + x\mathrm{e^-} \rightleftharpoons \mathrm{LiMO_2} \tag{2.1}$$

$$\text{Anode side:} \quad \mathrm{Li_xC_6} \rightleftharpoons x\mathrm{Li^+} + x\mathrm{e^-} + \mathrm{C_6} \tag{2.2}$$

$$\text{Total:} \quad \mathrm{Li_{1-x}} + \mathrm{Li_xC_6} \rightleftharpoons \mathrm{LiMO_2} + \mathrm{C_6} \tag{2.3}$$

Reaction arrows from left to right show the reactions during discharge while arrows from right to left show the corresponding reactions during charging. Increasing the amount of lithium in an electrode decreases its potential and vice versa. Therefore, the cell potential Φ_{Cell} increases during charge and decreases during discharge depending overpotentials and on the OCV of the anode and cathode:

$$\Phi_{cell} = \Phi_{OCV,c} - \Phi_{OCV,a} - \sum \eta \tag{2.4}$$

with $\Phi_{OCV,c}$, $\Phi_{OCV,a}$ and $\sum \eta$ for the open circuit voltage of the cathode and anode and the sum of all occurring overpotentials, respectively. A selection of the main processes with their overpotentials is shown in figure 2.1. Degradation processes cause additional overpotentials reducing the cell potential but are not shown in this example. Note, that the charges in the solid are transported solely by migration while the transport of Lithium-ions in the electrolyte is caused by migration and diffusion. Migration is induced by potential gradients and diffusion by concentration gradients. Therefore, the migration overpotentials depend on the conductivities of solid and electrolyte phases while the diffusion overpotentials depend on the related diffusion coefficients. Reaction overpotentials are dependent on the related reaction rate constants. Due to equation 2.4,

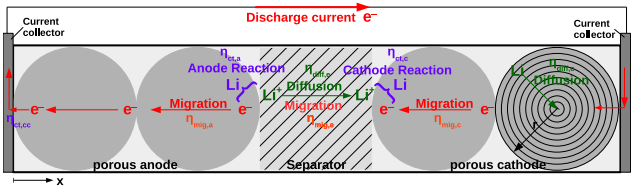

Figure 2.1: Schematic illustration of the main processes in a LiB with the related overpotentials

the discharge reaction will proceed until the electrical potential difference between the electrodes equals the overpotentials within the cell and the cell potential drops to zero.

2.1.3 Ageing in LiBs

Lithium-Ion Batteries suffer degradation during their lifetime. Due to undesired side reactions, mechanical stress or external impacts, the impedance of the cell rises and the power- and energy capabilities decrease. The aim of this section is to provide a brief overview of processes which lead to degradation of LiBs. The list is not complete but focused on the most relevant processes which have been considered in this work. A more detailed overview has been presented by Vetter et al. [7].

Solid Electrolyte Interphase: The Solid Electrolyte Interphase (SEI) forms on the anode during the first cycles. Due to the low anode potential, components of the electrolyte are being reduced and the reaction products deposit on the anode and form a layer [8]. Therefore, the properties of the SEI highly depend on the composition of the electrolyte and its additives [9]. In an optimal case, the resulting layer is insulating against electrons to avoid further reduction of the electrolyte but provides sufficient transport properties for Lithium-ions. Additionally, the layer should not break due to swelling and contraction of the anode particles during charge or discharge to avoid further side reactions. Since the reaction consumes Lithium, the capacity of the cell is being reduced because Lithium within the SEI is not available for the main charge trans-

fer reaction any more. In addition, the resistance of the cell rises because the Lithium has to pass through an additional layer when transported from one electrode to the other. Since the SEI is the most crucial factor to the ageing of LiBs it has been subject to numerous studies. An extensive overview is given in the book by Balbuena and Wang [10].

Particle Cracking: As mentioned above, particles of the electrodes change their size during charge and discharge of the cell. Since they are forced in a strict structure and on the current collectors, mechanical stresses occur that may lead to a cracking of particles [11, 12]. In general, smaller particles offer higher surfaces than large particles and therefore promote high power densities. But the additional surface is also exposed to the electrolyte and further SEI formation occurs. In addition, parts of the active material might loose the connection to the rest of the electrode due to particle cracking, causing a reduction of active material as well as a reduction of surface area available for reaction. Exfoliation of the current collectors due to the mechanical stresses has also been reported [13]. Therefore, the cracking can cause a loss of capacity and an increase of the impedance of the cell which will reduce the power- and energy density of the cell.

Lithium plating: During charge of a LiB, a specific rate of Lithium is forced to be transported from the cathode to the graphite anode. In case the transport from the cathode to the anode is significantly faster than the intercalation of Lithium into the anode, Lithium might deposit on the anode instead of intercalating. This process is promoted by high charging rates and low temperatures [14]. Since the plated Lithium forms dendrites which can pierce through the separator and cause internal short circuits, Lithium plating does not only increase the impedance of the cell and reduces its capacity but also causes severe safety issues [15].

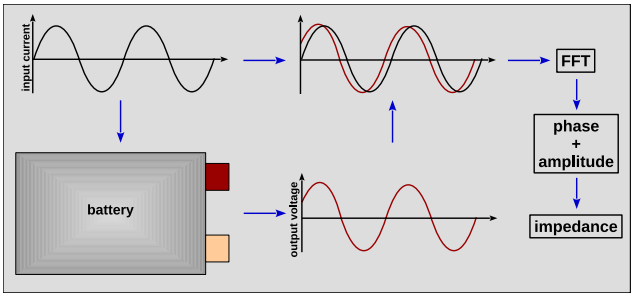

Figure 2.2: Schematic illustration of the galvanostatic EIS routine

2.2 Electrochemical Impedance Spectroscopy

Orazem and Tribollet start their book on Electrochemical Impedance Spectroscopy with a Buddhist parable about blind men and an elephant to sensitise the reader about possible misinterpretations of impedance results [16]. The blind men touch different parts of the elephant and therefore come to various conclusions about the likeness of the elephant. In the same manner, characteristics of an impedance spectrum might be related to physical processes which have not occurred during the measurement. Still EIS has become a widely spread dynamic measurement technique which enables a non-destructive characterisation of electrochemical systems [17]. Within this section, the fundamentals of EIS are briefly outlined and applied exemplary on Lithium-ion batteries. The working principle of EIS is depicted in figure 2.2. For a galvanostatic EIS, a sinusoidal input current is applied to the system under test. Due to this excitation the voltage of the system will swing sinusoidally with the same frequency. If energy is temporarily saved due to capacitive or inductive processes, input current and output voltage are phase-shifted. The phase shift between the two signals and the amplitude of the output signal can be calculated by Fourier transforming the output time domain data into the frequency domain. Using the amplitudes of the input and output signals as well as the phase shift provides all necessary values to apply equations 2.5 and 2.6

to calculate the real and imaginary part of the impedance of the system at this frequency. Real and imaginary parts can be used to calculate the magnitude of the impedance via equation 2.7.

$$\mathrm{Re}(\mathrm{Z}(\omega)) = \frac{\hat{\Phi}(\omega)}{\hat{I}(\omega)} \cdot \cos(\varphi(\omega)) \tag{2.5}$$

$$\mathrm{Im}(\mathrm{Z}(\omega)) = \frac{\hat{\Phi}(\omega)}{\hat{I}(\omega)} \cdot \sin(\varphi(\omega)) \tag{2.6}$$

$$|\mathrm{Z}((\omega))| = \sqrt{\mathrm{Re}(Z(\omega))^2 + \mathrm{Im}(Z(\omega))^2} \tag{2.7}$$

With Z, Φ, I, φ and ω being the impedance, voltage, current, phase difference and angular frequency ($\omega = 2\pi f$), respectively. Usually, the described routine is repeated for a wide range of frequencies until a complete spectrum is measured. For Lithium-ion batteries it is common to choose a frequency range of 100 kHz to 0.1 mHz. This frequency range includes all processes typically occurring in a LiB. Besides the galvanostatic EIS the potentiostatic EIS is often used. Here, as input signal a sinusoidal voltage is applied and the resulting current is measured.

2.2.1 Preconditions for EIS

In order to realise reliable EIS measurements, three conditions have to be fulfilled. These conditions are linearity, causality and stationarity and will be explained on the example of a LiB.

Linearity: EIS is a linear analysis technique and therefore can only be applied if the system under test is linear or exited in a linear range. For a linear system or a system excited in a linear range the maximum amplitude of the output signal always changes proportionally to the maximum of the input amplitude which means that the measured impedance is independent of the amplitude of the input signal. If this is the case then the measured impedance is independent of the input amplitude, because it is divided by the output amplitude as shown in equations 2.5 and 2.6. Since LiBs are highly nonlinear systems, the input amplitude has to be chosen as small as possible in order to ensure quasi linear conditions. If linearity

is not enforced, the output signal will be distorted by higher harmonics [18].

Causality: Causality means that there is a causal correlation between the output signal and the input signal. Each property of the output signal has to be caused by the input signal and not by any artefacts caused by the measurement device or the measurement setup. If causality is not ensured the resulting properties of the spectrum can not be clearly assigned to physical processes.

Stationarity: Before an EIS measurement can be performed, the system under test has to reach stationary conditions. All system variables like temperature or the State of Charge have to be constant and must stay constant during the whole measurement. Non stationary conditions can be identified if the sinusoidal output signal drifts either to higher or to lower values [19].

2.2.2 Impedance Spectroscopy on LiBs

If an impedance spectrum is measured, the results are typically displayed in either Nyquist or Bode plots. Bode plots show either the real part, the imaginary part, the magnitude or the phase shift of the impedance over the frequency on a logarithmic axis. Therefore, Bode plots are preferable if the assignment of a process to the related frequency is of importance. The Nyquist diagram lacks exactly this information, but displays real part, imaginary part, magnitude and phase of the impedance in one diagram. In Lithium-ion battery research it is more common to display results in a Nyquist diagram than in a Bode diagram [20, 21, 22]. In a Nyquist diagram of a LiB, typically four regions can be distinguished which are depicted in figure 2.3. Displayed is the negative imaginary part of the impedance over the real part of the impedance. The real part of the impedance quantifies the amount of dissipated energy while the imaginary part quantifies energy which is saved temporarily within the system due to capacitive or inductive processes. Since more of the processes in a LiB induce negative rather than positive imaginary parts, the imaginary part of the impedance

of a LiB is negative for the whole frequency range except for very high frequencies. Therefore, negative values of the imaginary part are commonly displayed in positive direction in Nyquist plots. The four characteristic parts of the spectrum are enumerated and explained starting from high and going to low frequencies.

(1) inductive: At high frequencies ($> 10^5$ Hz) no significant processes within a LiB are excited. Still, the spectrum shows an inductive behaviour in this frequency range, because the leads, required to connect the system to the measurement device, may induce magnetic fields which violate the causality requirement and therefore distort the measurement result. The effect occurs more significantly for cells with high capacities since the applied current during the measurement is higher. To reduce the effect the leads in use are often twisted and as short as possible.

(2) charge transfer and double layer: In the mid-frequency range (1 Hz – 10^4 Hz) the impedance spectrum often shows one or more semicircles which are often flattened and overlapping. In the second case the semicircle at lower frequencies is usually assigned to a superposition of the charge transfer of the main reaction (equation 2.3) at the two electrodes and the related charging and discharging of electrochemical double layers, while the high frequency semicircle is assigned to charge transfer or polarisation processes in or at surface layers [23] or to processes at the current collectors [24]. If only one semicircle is present it is assigned to a undistinguishable superposition of the main charge transfer reaction in anode and cathode.

(3) diffusive: At low frequencies (< 1 Hz) the spectrum shows an increase with approximately $45\,^\circ$. The actual slope varies due to the underlying geometry for the diffusion process which means the shape of particles or pores [25]. If the frequency is reduced to low values, the periodic time increases and the main charge transfer reaction will occur long enough causing concentration changes at the surface of the particles. Therefore diffusion will occur to compensate the generated concentration difference. The change of the concentrations affects the reaction in

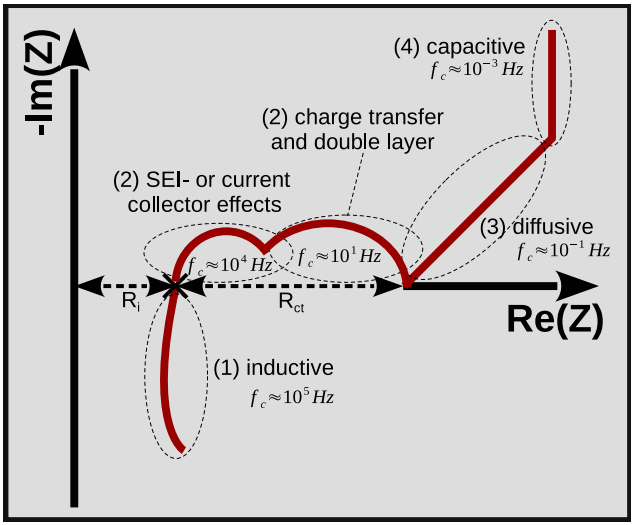

Figure 2.3: Exemplary EIS Spectrum of a LiB in a Nyquist diagram. R_i and R_{ct} indicate the internal and charge transfer reaction respectively

equation 2.3 and diffusion overpotentials increase. This affects the output signal of the impedance measurement which can be seen in the characteristic 45° increase of the impedance. Further details about the effect of boundary conditions for various types of diffusion and its impact on the impedance are outlined in section 2.4.4.

(4) capacitive: If the frequency is reduced even further, the battery reacts similar as to a direct current input. The corresponding real part provides information about the resistance of the cell and the vertical increase indicates the capacitive behaviour of the cell. Since the cell is significantly charged and discharged if imprinted with such a low frequency, stationarity of the system can not be ensured any more. In addition, measuring those frequencies takes a lot of time. Therefore, this frequency range is usually not measured although a method to analyse this frequency range has been presented by Schmidt et al. [26].

2.3 Equivalent Circuit Modelling

The evaluation of impedance measurement data using **E**quivalent **C**ircuit **M**odels (ECMs) can be done by interconnecting electrical circuit elements and adjusting their parameters in order to minimise the difference between measured and simulated impedance spectra. The most common circuit elements used to simulate the impedance spectra of LiBs are Resistors (R), Capacitors (C), Inductors (L), Constant Phase Elements (CPEs) (Q) and Warburg (W) (either infinite-length or finite-length with "open" of "close" terminal) elements [17, 27, 28]. Here R, C, L, and W have well-defined electrical circuit analogs of lumped and distributed elements but Q or CPE is an expression of impedance $Z(\omega) = 1/C(j\omega)^{\alpha}$ which becomes R, C, L, and W (infinite length) for α=0, 1, -1, and 1/2, respectively. Higher extents of association of circuit are also considered for impedance evaluation, for example, a series of three parallel connections of a resistor and a capacitor, as shown in figure 4.4a is called third order Voigt type element circuit [29]. Also, if CPEs are used instead of capacitors the circuits are called fractional order circuit models [30]. This is exemplary shown in figure 4.4b. In general, the ECM are applied considering three different regions of the impedance spectrum [31, 32, 33]. Each area is assigned to a frequency range as follow:

1. High frequency range: Inductive effects of the connecting wires modeled with an inductance and cell resistance (at about 10 kHz)

2. Mid frequency range: Parallel connections of resistors and capacities or CPEs used to model charge transfer reactions and double layer effects at anodes, cathodes and surface layers

3. Low frequency range: Diffusion processes modelled with Warburg elements

The fundamentals for the ECMs used today have been explored by Kohlrausch [34] and Heaveside [35]. Warburg integrated Ficks second law and found the 45° phase angle for diffusion processes which is characteristic for the

Warburg element [36]. The fundamental research for the CPE has been done by Cole and Cole in 1941. It should be noted that CPE with α close to 0 was first introduced for non-ideal R in the Debye dielectric response. Shortly after, the Randles circuit was introduced [37] which is the most used ECM in battery research so far. Since then, numerous variations of the Randles circuit with various complexity have been used in order to evaluate raw impedance data. The state of the art are either complex variations of the Randles circuit, so called Transmission Line Models or a combination of both. A comparison of both model types has been done bei Osaka et al. [38].

ECMs are nowadays frequently used because they are easy to set up and have low computational costs compared to physico-chemical models [39]. Therefore, they are suitable for the application in Battery Management Systems (BMSs). Furthermore, the analysis of various states of an LiB can be easily done by evaluating the change of identified parameters due to changes for example of the SoC, SoH or temperature. To this end, some research groups use SoH and temperature dependent circuit elements [40, 41, 42]. A good overview about the techniques to identify parameters of ECMs is given by Fleischer et al. [43]. The drawback of the ECMs, especially most elaborated ones, is the lack of correlation between the circuit elements applied and the physical processes happening in the LiB. This relevant aspect can make the interpretation of the identified parameters ambiguous.

Indeed, since various ECMs can produce the same impedance spectrum, choosing a physically-based ECM is essential for an appropriate evaluation of impedance data. In general, to minimise the risk of over fitting, it is suggested to reduced to a minimum number the circuit elements used in the ECM. It is also advisable to use the impedance spectra of the anode and cathode in combination with the full cell spectra in order to be able to assign the circuit elements to processes in the anode or in the cathode. Numerous research groups use either three-electrode (half of full cell) setups or two-electrode symmetrical cells to validate the chosen ECM for

the LiB cell under test. Analysing the impedance contributions of anode and cathode separately is often the only way to determine their contributions to the internal resistance, the diffusion impedance and to the impedance induced by charge transfer and double layer. Such an analysis is limited to research studies and can not be applied to practical applications of LiBs. In addition, it has to be considered that even a reference electrode might affect the impedance spectrum [44] and that the results from symmetrical cells, which are usually coin cells with electrodes harvested from commercial full cells, are not suitable to analyse surface films [45].

In many cases the measured impedance spectra of a commercial LiB cell does not follow the characteristics of ideal circuit elements [46]. Depending on the experimental investigation carried out, many research groups have presented modified ECMs. The most significant modification is the replacement of capacitors by CPEs in order to regard experimentally observed depressed semicircles or arcs [47]. Huang et al. give a good overview of such modified ECMs [48]. Adjustment of the ECMs are extensively reported in literature. For example, in the case of the high frequency range the inductance is sometimes placed in parallel to a resistance if the resistance of the inductive arc of the measured spectrum increases with increasing frequencies. Xiong et al. [49] have even replaced the inductance by a CPE to improve the quality of the resulting fit. In the mid frequency range the capacities in the Randles circuit or in other $R||C$ elements are often replaced by CPEs. Since the simulated arc of a parallel connection of R and CPE or $R||Q$ connection is depressed compared to the semicircle of a $R||C$ connection, the parallel connection of resistor and CPE is called Z_{ARC} which means an arc-shaped impedance trace. In case of degradation processes such as the SEI deterioration, the capacity of the SEI is sometimes placed in parallel to the Z_{ARC} elements as shown in figure 4.4d [50, 51]. To model diffusion processes, the Warburg element is either placed in serial to the other circuit elements or included in the Randles circuit (figure 4.4c). The effect of this simplification has

been analysed by Huang et al. [52]. From a physical point of view placing the Warburg element in parallel to the double layer capacitance, is to be preferred because the solid diffusion processes are induced by the charge transfer reaction and is unaffected by the charging and discharging of double layers. However, if impedance contributions from various processes should be separated for example to reduce the spectrum to its polarisation effects for further DRT analysis, placing the Warburg element in serial is recommended [53]. Some research groups replace the Warburg element completely by a CPE because the measured slope of the diffusion impedance often deviates from the inclination angle 45°. Oldenburger et al. [54] have explained this behaviour with the hysteresis of the OCV curve which effects the internal capacity which in turn effects the slope of the diffusion impedance. Other physical explanations state that the slope is effected by anisotropic diffusion in the particles and by the particle size distribution [55, 56].

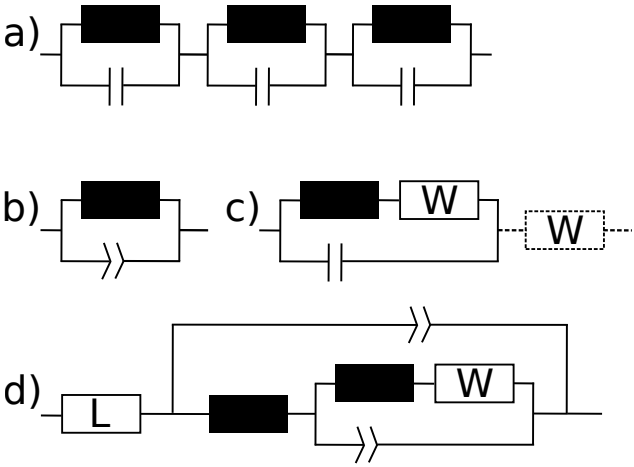

Figure 2.4: a) third order Voigt-type element, b) tractional order Voigt-type element, c) Randles circuit with alternative position of the Warburg element indicated with dashed lines, d) ECM with parallel CPE to regard the SEI as proposed in [50]

2.4 Reproduction of EIS features via physico-chemical Equations

In the previous section, equivalent circuit elements and equivalent circuit models have been discussed in detail. The equations underlying the equivalent circuit elements are similar to the equations used in physico-chemical models but reduced in their complexity. The aim of this section is to provide the reader an idea on the contribution of various equations on an impedance simulation. In the upcoming subsections all important equations are explained and their contribution on the impedance evaluated.

2.4.1 Physical Origin of the internal Resistance

Figure 2.3 shows an impedance spectrum of a LiB. The internal resistance R_i can be seen at the intersection of the spectrum with the real part axis. Its magnitude depends on the conductivities of the electrodes, the electrolyte, leads and current collectors. In Equivalent Circuit Models (ECMs) the internal resistance is modelled by a single ohmic resistance but the measured one is actually the sum of several contributions. The internal resistance is effected by all migration processes. Migration is usually described by Ohms law. Since the current in the solid and in the electrolyte phases are correlated by the main charge transfer reaction, Ohms law has to be combined with Faradays law. Due to Faradays law the amount of species taking part in the main reaction of a LiB is proportional to the electric charges which are applied to the electrode. The proportionality constant is the Faraday constant F. For the charges in a one dimensional Lithium-ion system follows for Faradays law:

$$\frac{\partial J_s}{\partial x} = j_{Li} \tag{2.8}$$

The change of the current per electrode area in the solid phase J_s in the direction of x depends on the reaction current density j_{Li} which quantifies

how many charges are generated with the main charge transfer reaction related to the volume of the active material. Ohms law can be written as

$$J_s = -\frac{\partial \Phi_s}{\partial x} \cdot \sigma_s \tag{2.9}$$

with σ_s for the electric conductivity of the solid. Combining equation 2.8 and equation 2.9 gives:

$$\frac{\partial^2 \Phi_s}{\partial x^2} = \frac{j_{Li}}{\sigma_s} \tag{2.10}$$

Equation 2.10 clarifies that the impedance contribution from the migration in the solid phase of the battery is dependent on the flux through the solid and reciprocal to the conductivity of the active material. Since the equation does not include any time derivatives no phase shifts between current and voltage will be calculated and therefore the impedance will be frequency independent and its imaginary part always zero. Equations to describe the potential in the electrolyte or in the SEI can be deduced in a similar manner but concentration gradients of the Lithium-ions have to be additionally regarded. The respective derivations are not emphasised here because the important fact to be highlighted at this point is the lack of time derivatives in all these equations which means that they all solely contribute to the calculated internal resistance.

2.4.2 Effect of Charge Transfer and Double Layers

The semicircle visible in the impedance spectra for most LiBs can be modelled with a parallel combination of a resistor and a capacitor in an ECM. Physico-chemical models use the same assumption that the total current i_{tot} is split into a reaction part i_{Li} and a capacitive double layer part i_{DL}:

$$i_{tot} = i_{Li} + i_{DL} \tag{2.11}$$

Most commonly the Butler-Volmer equation is used to calculate the reaction current in an exponential dependency of the overpotential η:

$$i_{Li} = a_s i_0 (exp(\frac{F\alpha_o}{RT}\eta) - exp(-\frac{F\alpha_r}{RT}\eta)) \tag{2.12}$$

Since the system will only be exited linearly when low amplitudes are used during impedance measurements, the Butler-Volmer equation can be linearised to

$$i_{Li} = a_s i_0 (\frac{F\alpha_o}{RT}\eta + \frac{F\alpha_r}{RT}\eta). \tag{2.13}$$

For the case of a symmetrical reaction $\alpha_r = \alpha_o = 0.5$ applies and the equation simplifies to

$$i_{Li} = a_s i_0 \frac{F}{RT}\eta. \tag{2.14}$$

The charge transfer resistance R_{ct} can be calculated with the derivative $\partial i_{Li}/\partial\eta$:

$$\frac{\partial i_{Li}}{\partial \eta} = a_s i_0 \frac{F}{RT} = \frac{1}{R_{ct}} \tag{2.15}$$

The charging and discharging of double layers can be calculated as follows:

$$i_{DL} = a_s C_{DL} \frac{\partial \Delta\Phi}{\partial t} \tag{2.16}$$

C_{DL} is the double layer capacitance and $\Delta\Phi$ the potential difference between the solid phase and the electrolyte phase. The impedance contribution of this equation can be deduced if the Laplace transformation is applied:

$$\mathcal{L}(i_{DL}) = \mathcal{L}(a_s C_{DL} \cdot \frac{\partial \Delta\Phi}{\partial t}) = a_s C_{DL} s \cdot \mathcal{L}(\Delta\Phi) \tag{2.17}$$

In the present case $s = 2\pi f i$ with f for the frequency and i for the imaginary unit. The Laplace transformation of the potential divided by the Laplace transformation of the current equals the complex impedance

for the present case:

$$\frac{\mathcal{L}(\Delta\Phi)}{\mathcal{L}(i_{DL})} = Z_{cap}(f) = \frac{1}{a_s C_{DL} 2\pi f i} \tag{2.18}$$

The complex impedance of the capacitor Z_{cap} has no real part and is frequency dependent. Combining the charge transfer resistance R_{ct} in parallel with the impedance of the capacitor Z_{cap} gives the total impedance:

$$Z_{tot}(f) = \frac{R_{ct}}{1 + a_s C_{DL} 2\pi f i} \tag{2.19}$$

For high frequencies, the impedance tends to zero, because the circuit is short circuited via the capacitor and for low frequencies the capacitive part can be neglected and the total impedance equals the reaction part of the impedance R_{CT}. Therefore the corresponding impedance spectrum shows a semicircle from zero at high frequencies to R_{CT} at low frequencies as can be seen in figure 2.3. It has to be emphasised at this point, that the presented equations do not represent the exact processes within a LiB. In physico chemical battery models the discretisation [57] as well as the particle size distribution and agglomerates [58] are regarded which flattens the resulting semicircle.

2.4.3 Temperature- and SoC-Dependence of the Charge Transfer Resistance

Measurement results show that the semicircles in Nyquist plots change their diameters with temperature [59, 60] and SoC [61, 62]. The temperature dependency is caused by the underlying charge transfer processes which are highly temperature dependent. In addition, these charge transfer processes are dependent on the Lithium loading of the two electrodes as well which causes a nonlinear SoC dependency. Therefore, it is desirable to model this dependence with physico-chemical models. The Butler-Volmer equation which describes the charge transfer reaction includes the temperature as a variable, but increasing its value does not decrease the

resulting charge transfer reaction as can be seen in equation 2.15. Since electrochemical reactions occur at lower overpotentials when the temperature is increased, it is obvious that the Butler-Volmer equation, as introduced in equation 2.12, does not represent the actual temperature behaviour of the impedance of a charge transfer. If this behaviour should be included in a physico-chemical model, the exchange current density i_0 has to be included as a function of the temperature which is commonly done with the Arrhenius equation.

In order to be able to consider various SoCs of a LiB, the exchange current density has to be concentration dependent as well. Depending on the cell chemistry various empirical equations based on the Nernst equation have been introduced [63, 64, 65] which only vary slightly with their impact on the simulated impedance.

2.4.4 From Ficks Law to a Diffusion Impedance

The process of diffusion is mathematically described with Ficks second law, a combination of Ficks first law and the continuum equation. For the diffusion in the direction of r in a solid spherical material it writes as [66]:

$$\frac{\partial c_s}{\partial t} = \frac{1}{r^2}\frac{\partial}{\partial r}\left(D_s r^2 \frac{\partial c_s}{\partial r}\right) \tag{2.20}$$

c_s is the concentration in the solid phase and D_s the corresponding diffusion coefficient. Equation 2.20 can be either solved analytically using the Laplace transformation [25] or numerically [57]. In any way boundary conditions are needed to solve the derivatives in space. The resulting impedance response depends on the chosen boundary condition [25]. If a Dirichlet boundary condition is chosen, which in this case means a concentration at the boundary fixed to a specific value, the resulting impedance is called Nernst impedance and shows a semicircle at low frequencies. For a Neumann boundary condition the flux at the boundary is fixed, for example to zero at the inner of a active material particle. The resulting impedance is called Warburg impedance. As can be seen in figure

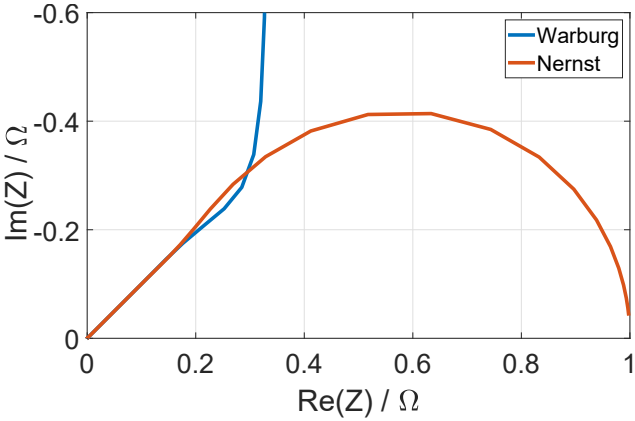

Figure 2.5: Nyquist diagram of Nernst and Warburg impedances calculated with the analytically deduced equations presented in [25]

2.5 Warburg and Nernst impedance show identical behaviour at high frequencies when the change of the concentrations is not yet affected by the chosen boundary condition. As soon as the concentrations are affected by the boundary conditions, the Nernst impedance shows a semicircle while the Warburg impedance shows capacitive behaviour. For LiBs Warburg impedances are present since the core of the active material particles acts like a Neumann boundary with a flux fixed to zero. Nernst impedances on the other hand are used for the modelling of fuel cells because the continuous supply of reactants leads to the constant concentration assumed for the Nernst impedance.

2.4.5 Impact of Ageing on the Impedance of LiBs

In EIS-Simulations, the effect of ageing can either be reproduced by adjusting the values of battery model parameters [67, 68] which change during ageing or by implementing additional ageing processes into the model [69, 70]. Adjusting the parameters is often done by parameter identification algorithms for conductivities, diffusion coefficients, reaction rate constants, double layer capacitances and geometrical parameters which

have a direct impact on the impedance through the model equations. A second option is to calculate the change of ageing parameters. For example the growth of the SEI can be calculated starting with an equation for a reduction reaction [20]:

$$i_{SEI} = -a_s i_{0,SEI} exp(-\frac{F\alpha_r}{RT}\eta_{SEI}) \tag{2.21}$$

With i_{SEI}, $i_{0,SEI}$ and eta_{SEI} being the charge, exchange current density and the overpotential of the side reaction causing the growth of the SEI. Degradation is usually too slow and the overpotential η_{SEI} too low to have a direct impact on the impedance of the cell, because the impedance is measured in stationary conditions, but the calculated current i_{SEI} can be used to calculate the change of the thickness of the SEI. Using the thickness of the SEI, directly lead to the increase of the impedance rise and the capacity loss caused by the SEI [71]. Similar approaches can be used for lithium plating or surface films on the cathode. If additional polarisation at the surface layer interfaces have to be considered, equation 2.11 can be applied again assuming an additional charge transfer reaction and a related double layer causing the described effects on the impedance of the cell which is further explained in [71].

2.5 Sensitivity and Identifiability of Parameters

Sensitivity analysis is used to determine how various input parameters of a model affect its output parameters. The sensitivity can be used to evaluate the identifiability of parameters. First of all, it has to be checked if the parameters of a model are structurally identifiable [72]. If this is the case, for the practical identifiability it must be distinguished between a global and a local identifiability. If a parameter can only identified with a single value, the parameter is globally identifiable. Often, the value of the identified parameter depends on the initial values of the state variables of the model and multiple solutions for the identification of the parameter exist. In this case the parameter is only locally identifiable. [73] Sensi-

tivity analysis can be applied to identify the complete variance of model outputs due to a variance of input parameters of a wide range of the absolute value of the input parameter even with nonlinear parameter correlations. A local sensitivity analysis also analyses the impact of the variance of an input to the variance of an output but focusses on a single absolute value of the input parameters which greatly reduces the complexity of the problem [74]. For LiBs, parameter identification algorithms are often used in combination with LiB models and discharge curves or impedance measurements in order to determine unknown kinetic or transport parameters of the model. In this case the input parameters are predefined and a global sensitivity analysis is not necessary. In this work the Fisher Information Metric is used which is a method to evaluate the identifiability, the standard deviation and the correlations of such estimated parameters. It has already been applied to batteries [75, 76, 77, 78, 79, 80, 81] and even to ECM modelling on LiBs [82, 83] but not for EIS simulations on physico chemical LiB models yet. The FIM is the standard tool to evaluate the practical identifiability of parameters because it is easier to apply than Monte Carlo simulations or Bootstrapping [84]. It has been shown that the FIM has weaknesses if simulations are carried out in the time domain, if limited measurement data is available or if the analysed system is highly nonlinear [85]. Since all these points do not apply for the linear EIS, the FIM has been chosen to evaluate the identifiability of parameters. The aim of the upcoming section is to deduce the numerical form of the Fisher Information Metric which is used in sections 6.1 and 6.2 on kinetic, transport and ageing parameters.

2.5.1 Fisher Information Metric

A LiB can be simplified to a **S**ingle-**I**nput **S**ingle-**O**utput (SISO) system with the current as imput and the voltage as output signal or vice versa. In control engineering a SISO system can be described with two differential

equations in the following form [86]:

$$\frac{d\vec{x}(t)}{dt} = f(\vec{x}(t), u(t), \vec{\theta}) \tag{2.22}$$

$$y(t) = g(\vec{x}(t), u(t), \vec{\theta}) \tag{2.23}$$

The change of the state variables $\vec{x}(t)$ with time as well as the output signal $y(t)$ depend on the state variables itself, the input signal $u(t)$ and the model parameters $\vec{\theta}$. For a number of k parameters, the parameter vector can be defined as $[\theta_1, \theta_2, \ldots, \theta_k]$. If the parameters are known and the initial values for the state variables $\vec{x}(t_0)$ and the input signal are given, equations 2.22 and 2.23 can be solved to calculate the output signal $y(t)$. The aim of parameter identification algorithms is to adjust the parameters θ_k until the difference between the model output $y(t)$ and the corresponding measurement output $\hat{y}(t)$ is at an minimum. $\hat{y}(t) - y(t, \vec{\theta})$ is defined as the model error. If it is assumed that the model error is only caused by the noise of the measurement sensor $\epsilon(t)$, then the related normal distribution with its expected value μ_ϵ and its standard derivation σ_ϵ can be introduced. The assumption that the model error is solely caused by the uncertainties of the measurement sensor is common [82, 83]. The properties of the introduced normal distribution affect how precise the parameters of the model can be identified. In order to describe the probability that the model error $\epsilon(t)$ can be attributed to the normal distribution of the noise of the measurement sensor the Likelihood function $L_1(\vec{\theta})$ can be introduced. In practical, the Likelyhood function quantifies how likely an assumed set of battery model parameters is true for the measured output. For the given case of an impedance spectrum as measurement data for each measured frequency i the Likelihood function can be calculated as [83]:

$$L_i(\vec{\theta}) = \frac{1}{\sqrt{2\pi}\sigma_\epsilon} \exp\left(- \frac{((\hat{y}(t_1) - y(t_1, \vec{\theta}) - \mu_\epsilon))^2}{2\sigma_\epsilon^2} \right) \tag{2.24}$$

If it is assumed that the normal distribution of the uncertainty of the measurement sensor is symmetric the expected value of the noise of the measurement sensor is zero and equation 2.24 simplifies to

$$L_i(\vec{\theta}) = \frac{1}{\sqrt{2\pi}\sigma_\epsilon} \exp\left(- \frac{(\hat{y}(t_1) - y(t_1, \vec{\theta}))^2}{2\sigma_\epsilon^2} \right). \tag{2.25}$$

If the noise of the measurement sensor is independent and equally normally distributed at all frequencies, the corresponding Likelihood functions can be summarised as follows:

$$L(\vec{\theta}) = \prod_{i=1}^{N} L_i(\vec{\theta}) = \left(\frac{1}{\sqrt{2\pi}\sigma_\epsilon} \right)^N \prod_{i=1}^{N} \exp\left(- \frac{(\hat{y}(t_i) - y(t_i, \vec{\theta}))^2}{2\sigma_\epsilon^2} \right), \tag{2.26}$$

with N for the number of analysed frequencies. Equation 2.26 shows that the model error $\epsilon(t)$ has to be minimised in order to maximise the function value of the Likelihood function. A maximum of the Likelihood function shows the best possible identification of the related parameter and frequency. These maxima can be calculated for each parameter and frequency with the first derivative of the Likelihood function with respect to the related parameter. Since the Logarithm function is monotonous and the maximum of the logarithm of the Likelihood function can be calculated more easily $\ln(L(\vec{\theta}))$ instead of $L(\vec{\theta})$ is maximised. If a monotonous function is logarithmised, the position of its maxima and minima does not change. For the deduction of the FIM the absolute value at the maxima of the Likelihood function is not needed. Therefore the logarithmised function can be used. This leads to the following equation:

$$\ln L(\vec{\theta}) = -\frac{N}{2} \ln(2\pi\sigma_\epsilon^2) - \frac{1}{2\sigma_\epsilon^2} \sum_{i=1}^{N} (\hat{y}(t_i) - y(t_i, \vec{\theta}))^2 \tag{2.27}$$

The first derivatives of equation 2.27 with respect to every parameter can be displayed in a matrix:

$$\frac{\partial}{\partial\theta}\ln L(\vec{\theta}) = \begin{pmatrix} \frac{\partial}{\partial\theta_1}\ln L(\vec{\theta}) \\ \frac{\partial}{\partial\theta_2}\ln L(\vec{\theta}) \\ \vdots \\ \frac{\partial}{\partial\theta_k}\ln L(\vec{\theta}) \end{pmatrix} = \begin{pmatrix} \frac{1}{\sigma_\varepsilon^2}\sum_{i=1}^{N}(\hat{y}(t_i) - y(t_i,\vec{\theta}))\frac{\partial y(t,\vec{\theta})}{\partial\theta_1} \\ \frac{1}{\sigma_\varepsilon^2}\sum_{i=1}^{N}(\hat{y}(t_i) - y(t_i,\vec{\theta}))\frac{\partial y(t,\vec{\theta})}{\partial\theta_2} \\ \vdots \\ \frac{1}{\sigma_\varepsilon^2}\sum_{i=1}^{N}(\hat{y}(t_i) - y(t_i,\vec{\theta}))\frac{\partial y(t,\vec{\theta})}{\partial\theta_j} \end{pmatrix}$$

$$= \begin{pmatrix} \frac{\partial y(t,\vec{\theta})}{\partial\theta_1}\Big|_{t=t_1} & \frac{\partial y(t,\vec{\theta})}{\partial\theta_1}\Big|_{t=t_2} & \cdots & \frac{\partial y(t,\vec{\theta})}{\partial\theta_1}\Big|_{t=t_N} \\ \frac{\partial y(t,\vec{\theta})}{\partial\theta_2}\Big|_{t=t_1} & \frac{\partial y(t,\vec{\theta})}{\partial\theta_2}\Big|_{t=t_2} & \cdots & \frac{\partial y(t,\vec{\theta})}{\partial\theta_2}\Big|_{t=t_N} \\ \vdots & \vdots & \ddots & \vdots \\ \frac{\partial y(t,\vec{\theta})}{\partial\theta_k}\Big|_{t=t_1} & \frac{\partial y(t,\vec{\theta})}{\partial\theta_k}\Big|_{t=t_2} & \cdots & \frac{\partial y(t,\vec{\theta})}{\partial\theta_k}\Big|_{t=t_N} \end{pmatrix} \begin{pmatrix} \frac{\hat{y}(t_1)-y(t_1,\vec{\theta})}{\sigma_\varepsilon^2} \\ \frac{\hat{y}(t_2)-y(t_2,\vec{\theta})}{\sigma_\varepsilon^2} \\ \vdots \\ \frac{\hat{y}(t_N)-y(t_N,\vec{\theta})}{\sigma_\varepsilon^2} \end{pmatrix} \tag{2.28}$$

Each derivative in equation 2.28 is defined as S_{ij} and describes the local sensitivity of the model output with respect to the parameter θ_j at a given frequency i.

$$S_{ij} = \frac{\partial y(t,\vec{\theta})}{\partial\theta_j}\Big|_{t=t_i} \tag{2.29}$$

The Log-Likelihood function can be used to calculate the Fisher Information Metric [86]:

$$\mathbf{F} = \mathrm{E}\left[\left(\frac{\partial}{\partial\theta}\ln L(\vec{\theta})\right)\left(\frac{\partial}{\partial\theta}\ln L(\vec{\theta})\right)^{\mathrm{T}}\right] \tag{2.30}$$

$\mathbf{F}$ is the Fisher Information Metric, $\mathrm{E}[\cdot]$ is an operator to calculate the estimated value and T stands for the transposition of the matrix. The Fisher Information Metric formalism is used to predict how well an experiment will be able to constrain the model parameters. Combining the equations 2.28, 2.29 and 2.30 gives the numerical equation for the calculation

of the Fisher Information Metric:

$$\mathbf{F} = \frac{1}{\sigma_e^2} \begin{pmatrix} \sum_{i=1}^{N} S_{i1}^2 & \sum_{i=1}^{N} S_{i1}S_{i2} & \cdots & \sum_{i=1}^{N} S_{i1}S_{ik} \\ \sum_{i=1}^{N} S_{i2}S_{i1} & \sum_{i=1}^{N} S_{i2}^2 & \cdots & \sum_{i=1}^{N} S_{i2}S_{ik} \\ \vdots & \vdots & \ddots & \vdots \\ \sum_{i=1}^{N} S_{ik}S_{i1} & \sum_{i=1}^{N} S_{ik}S_{i2} & \cdots & \sum_{i=1}^{N} S_{ik}^2 \end{pmatrix} \tag{2.31}$$

If the Fisher Information Metric is invertible the resulting matrix is called covariance matrix because its entries describe the correlation between all considered parameters and the variance of them. Due to the Cramér-Rao-inequality

$$\mathrm{Cov}(\vec{\theta}) \geq \mathbf{F}^{-1}, \tag{2.32}$$

with $\mathrm{Cov}(\vec{\theta})$ for the covariance matrix of the identified parameters, these variance values are best possible minimum values, because they only regard for the uncertainty of the measurement sensor. If the uncertainty is increased by additional factors the variance of the identified parameters will increase as well [87]. Within this work it is assumed that the model error is caused by the noise of the measurement sensor and therefore the inverse of the Fisher Information Metric equals the covariance matrix. If two parameters affect the impedance spectrum exactly in the same way their covariance will become 1 and their variance infinity. In this case the Fisher Information Metric is not invertible and the corresponding parameters can not be identified.

In practical applications the values on the diagonal of the covariance matrix are used to calculate the standard deviation of each parameter which is the square root of the related variance. In order to relate this standard deviation to the absolute value of the parameter, the relative error can be calculated. If multiples of the standard deviation are used for the calculation, the related confidence interval indicates the percental chance that parameters are within this interval:

$$\text{relative error} = \frac{3\sigma}{\text{parameter value}} \times 100\% \tag{2.33}$$

For the 3σ-confidence interval, used in this work, the identified parameters have a chance of 99.73% that the actual error is not greater than the calculated relative error. Instead of the covariances shown in the remaining entries of the covariance matrix, the related correlation coefficients are calculated:

$$\rho(X_1, X_2) = \frac{Cov(X_1, X_2)}{\sigma_{X_1}\sigma_{X_2}} \tag{2.34}$$

With X_1 and X_2 being two exemplary random variables. The equation normalises the covariances to values between -1 and 1. A correlation coefficient of 1 or -1 shows a complete positive or negative correlation, respectively. Correlation coefficients of zero indicate that the related parameters do not correlate at all.

In this work the Fisher Information Metric is used to quantify covariances between identified model parameters and to determine how precise these model parameters can be identified.

3 Extended Motivation and Scope of Thesis

EIS is a measurement technique where a single input is applied to a system and a single output is measured. Therefore different processes within the system can only be detected if they affect the output signal and they can only be separated if they occur at different time constants. If processes occur on very similar time constants they effect the output signal at the same frequencies and distinction between them is often impossible or at least difficult. This issue applies for LIBs in multiple cases, since the diffusion as well as the reactions often have similar time constants in the two electrodes. In order to identify the change of battery parameters precisely to be able to correlate this change to the SoH of a cell, these issues have to be overcome. Therefore, in the upcoming sections 3.1 and 3.2, the feasibility to distinguish between anode and cathode processes are discussed for the main charge transfer reaction and for the diffusion in the active material particles, respectively. In section 3.3 the issue of unambiguous parameter identification is discussed and methods to quantify the identifiability of processes and parameters using EIS are introduced. It must be clarified that unambiguous parameter identification as shown in chapter 5 is only possible if a clear assignment of the changes of the impedance spectrum to the underlying physical processes can be made.

3.1 Reactions with similar Time Constants

As discussed for figure 2.3, a typical impedance spectrum of a LiB has a semi circle in the mid frequency range which is a superposition of the charge transfer processes in anode and cathode coupled with the related charging and discharging of electrochemical double layers. Depending on the resulting characteristic time constants τ_a and τ_c the semi circle is either round, depressed or split into two semi circles. Figure 3.1 illustrates

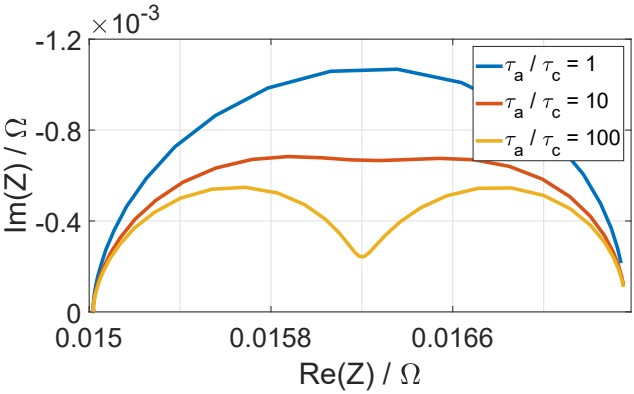

Figure 3.1: Charge transfer resistance of anode and cathode. Time constants of anode and cathode are equal (blue) or differ by 10 (red) or 100 (yellow).

these three cases and emphasises that the time constants of the two processes have to be different by a factor of one hundred (yellow) to receive two separated semi circles or at least to differ by a factor of ten (red) to even have the possibility of identifying the two processes. The equations and parameter to reproduce the simulations are shown in appendix 11.1. If the time constants are equal (blue) the impedance spectrum does not provide any information about the amount of underlying processes. This especially becomes an issue if a measured spectrum shows two semicircles of similar time constants, because it is unclear if the high frequency semicircle has to be assigned to an electrode or to processes within the Solid Electrolyte Interphase on the anode. One method to overcome this issue for specific types of batteries is presented in chapter 4. Another possible model-based approach to predetermine the time constants of anode and cathode time constants is outlined within the results presented in chapter 5.

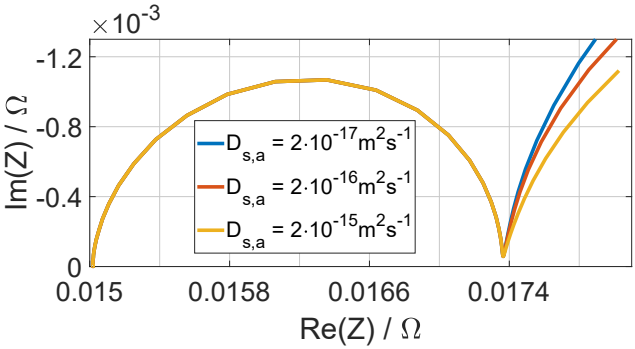

Figure 3.2: Impact of the diffusion coefficient $D_{s,a}$ on the simulated impedance spectrum assuming a constant value for $D_{s,c} = 2 \cdot 10^{-16} \mathrm{m}^2\mathrm{s}^{-1}$.

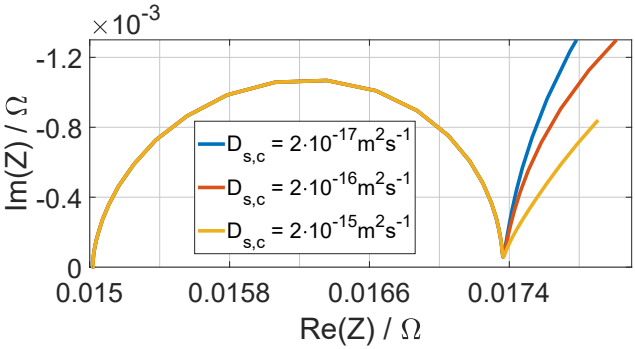

Figure 3.3: Impact of the diffusion coefficient $D_{s,c}$ on the simulated impedance spectrum assuming a constant value for $D_{s,a} = 2 \cdot 10^{-16} \mathrm{m}^2\mathrm{s}^{-1}$.

3.2 Diffusion Overlapping

The time constants in anode and cathode are not only similar for the charge transfer reaction occurring on both electrodes, as explained in section 3.1, but also the solid diffusion impedance results often can not be clearly assigned to anode or cathode. In comparison to the reaction kinetics analysing diffusion is more complex. Diffusion is driven by concentration gradients but for EIS the resulting voltage signal is evaluated. Therefore, the effect of concentration changes on the resulting voltages within the battery cell has an indirect impact on EIS via the reaction. The issue of the overlapping diffusion processes and the effect of the concentration changes on the impedance can be analysed by simulating impedance spectra of an electrochemical battery model with various diffusion coefficients. All model equations and the set of parameters are introduced in detail in section 5.3 and table 5.1, respectively. Figure 3.2 and 3.3 show simulations for a change of the anode and cathode diffusion coefficient respectively. Even though kinetic- and transport parameters of anode and cathode have been chosen to be equal, the sensitivity of the spectrum to a change of the two diffusion coefficients is different. This difference results from the two empirical equations which calculate the OCV of the anode and cathode depending on the surface concentration of the active material particles. For the anode the following equation has been used [65]:

$$\begin{aligned}\Phi_{OCV,a}(g_a) = 8.00229 + 5.0647 g_a - 12.578 g_a^{0.5} - 8.6322 \cdot 10^{-4} g_a^{-1} \\ +2.1765 \cdot 10^{-5} g^{1.5} - 0.46016 exp(0.9 - 15 g_a) \\ -0.55364 exp(-2.4326 g_a + 2.237992)\end{aligned} \tag{3.1}$$

With g_a being the insertion rate of the anode $g_a = {}^{c_a}/_{c_{max,a}}$. For the cathode [65]

$$\Phi_{OCV,c}(g_c) = 85.681g_c^6 - 357.7g_c^5 + 613.89g_c^4 - \\ 555.65g_c^3 + 281.06g_c^2 - 76.648g_c - 0.30987exp(5.657g_c^{115}) \tag{3.2}$$

with g_c being the insertion rate of the cathode $g_c = {}^{c_c}/_{c_{max,c}}$. A higher slope of the chosen OCV-curve at the chosen SoC causes a higher sensitivity of the impedance spectrum to a change in surface concentrations and therefore to a change of the diffusion impedance. In most LiBs graphite is chosen as anode material which has a flat OCV-curve over the whole SoC range. The OVC-curves used for the simulation are mathematically introduced in equation 3.1 and 3.2 and the resulting curves are displayed in figure 3.4 for the anode and cathode, respectively. At SoC 100 the slope of the cathode OCV-curve is significantly higher than the slope of the anode OCV-curve. Therefore, if the diffusion processes in anode and cathode are influenced, for example due to a change in the temperature, changes in the impedance spectrum at SoC 100 and for the given materials are most likely dominated by the cathode diffusion. Anode diffusion still takes place but does not significantly affect the total impedance. Assuming a case where both OCV-curves are known and the diffusion sensitivity of the impedance spectrum is measured at various SoCs it is theoretically possible to gain information about the diffusion coefficients of the system. Since the spectrum is highly sensitive to temperature changes and the exact concentrations of Lithium within the electrodes can currently not be determined, such analyses are error-prone. For this reason the low frequency range of the impedance spectrum was not used for the determination of ageing parameters in chapter 5.

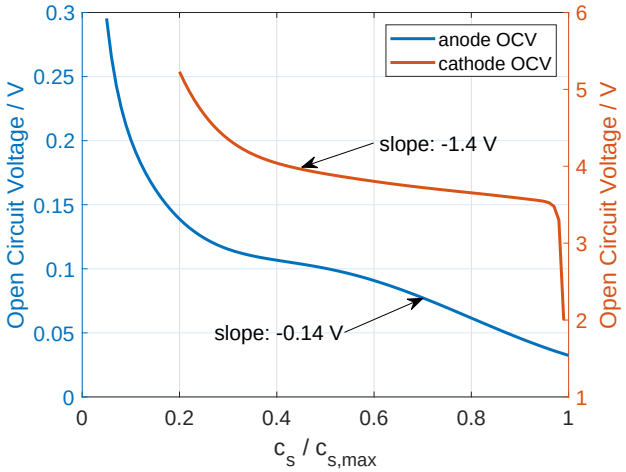

Figure 3.4: OCV curves of the anode and the cathode with their slopes at SoC 100 calculated for graphite and Lithium manganese dioxide

3.3 Identifiability of Parameters

The combination of impedance measurement data and the corresponding simulation data is a widely-spread method to identify battery parameters. **E**quivalent **C**ircuit **M**odels (ECM) or physico-chemical models are set up and their parameters are adjusted so that the simulated spectra agree with the measured ones. Depending on the chosen model such an agreement is achieved easily with a low divergence between measurement and simulation. Unfortunately, various ECMs can produce the same impedance output which makes the resulting parameter identification ambiguous if it can not be ensured that the chosen model represents the actual physics of the battery. In this work, physico-chemical models have been used, because they are more strict in their assignment of model equations to physical processes. Anyway, those models include a high amount of parameters, most of them unknown. If unknown parameters affect the same part of the impedance spectrum, unambiguous parameter identification is only possible with a certain uncertainty or even impossible. In order

to assess the possibility of unambiguous parameter identification, mathematical methods have been developed. The calculation of the Fisher Information Metric for instance provides information about the variance and the covariance of parameters being identified. In general, parameters affecting the impedance spectrum significantly can be identified more precisely. In chapter 5 variances and covariances are calculated to verify the uniqueness of the simulation results for the identification of kinetic-transport- and ageing parameters.

3.4 Concluding Remarks

Within this chapter three challenges of EIS have been outlined which apply if EIS is used on LiBs:

- Reactions with similar time constants
- Diffusion overlapping
- Identifiability of parameters

Only for the overlapping of impedance contributions of diffusion processes in anode and cathode, a brief idea on a possible method to overcome the limitation has been presented. The upcoming chapters 4 and 5 will demonstrate how to predetermine the time constants of anode and cathode reactions and how to identify anode and cathode contributions to the charge transfer reaction impedance with a specific measurement set-up. Chapter 6 focusses on the identifiability of parameters.

4 Temperature gradient Method for Electrode Discrimination

As outlined in the previous chapter the similar time constants of the main reaction at anode and cathode becomes an issue if impedance data is used to identify parameters of a battery model. Therefore, within this chapter a new measurement method is presented that enables the assignment from full-cell impedance spectra. To this end, temperature gradients are imprinted across the width of a single-layered Li-ion battery cell while impedance spectra are measured. The method exploits different dependences of the charge transfer processes at the electrodes on temperature. A simplified equivalent circuit model of RC-elements and the effect of temperature on the related electrode properties is discussed to demonstrate the feasibility of the method.

4.1 Introduction

Measured electrochemical impedance spectra are usually evaluated with physico-chemical models [63, 20] or, more frequently, with equivalent circuits [88, 89] to analyse internal processes of Li-ion battery (Lib) cells. The simulations use physico-chemical parameters, like reaction constants, or circuit elements, like the charge transfer resistance, to reproduce the measured impedance spectra of full-cells. It is very difficult to distinguish between effects of the anode and the cathode and to assign them to specific features of a spectrum. Usually half-cell measurements are used for this purpose but the results found on half cells can only be applied to full cells to some extent.

Many spectra of full cells include a distorted arc that is usually assigned to a superposition of two semicircles which represent charge transfer impedances at the anode and the cathode [63, 90]. Independent of the shape of the spectra, unambiguous allocation of the semicircles to their

respective electrodes requires prior knowledge, e.g. via half cell measurements or property variation of single electrodes. Correct allocation, however, is crucial if anode and cathode parameters of equivalent circuit models have to be identified unambiguously. Numerous studies have analysed half cells [22, 91, 92, 93, 94, 95], symmetrical cells [96, 97, 98, 99, 100, 101] or cells including a reference electrode [102, 103, 104, 105, 106] in order to investigate the impedances of an individual electrode rather than the full cell impedance. These studies show that the time constants of the main charge transfer reactions at anode and cathode are most often in the same order of magnitude, but not identical. This leads to the above mentioned two overlapping arcs in an impedance spectrum which are somewhat separated from each other. To the best of our knowledge, no study has yet shown how to identify anode and cathode impedance contributions from full-cell spectra without using reference electrodes or modifying one electrode. Such information, however, will be extremely helpful to understand processes in the battery: Changes of impedance spectra e.g. due to a change of the State of Charge (SoC) or the State of Health (SoH), can be assigned to changes of the properties of the anode or the cathode. Figure 4.1 shows measured impedance spectra of an anode half-cell, a cathode half-cell and the corresponding full cell of a Li-ion battery cell. The spectrum is reduced by fitting and subtracting inductive and diffusive parts, so that only the charge transfer impedances of anode and cathode, represented by the arcs, are visible. The sum of the half-cell impedances equals the full cell impedance. In order to illustrate the issue, the full cell spectrum is simulated by an equivalent circuit model with two constant phase elements (CPE) each in parallel to a charge transfer resistance R, which we denote by CPE||R (solid blue line). Simulations on this simple model are able to reproduce the measured spectrum but without half cell measurements it cannot be decided which of the two CPE||R elements must be assigned to the anode and which to the cathode.

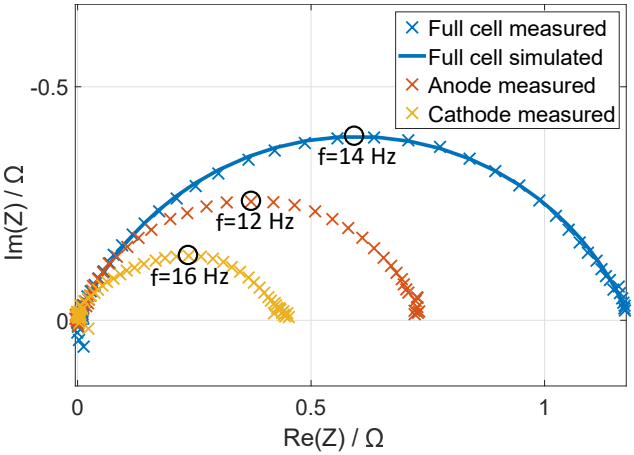

Figure 4.1: Nyquist plot of impedances of a 60 mAh Li-ion pouch cell (cell I) with the corresponding half cell impedances. Inductive and diffusive parts have been omitted.

A new measurement method is presented to address this problem by using Peltier elements to imprint a temperature gradient across the width of a single layered Li-ion cell. The basic idea to distinguish anode and cathode in the modelling of a full cell impedance spectrum is to measure impedance spectra $Z(f)$ at different anode and cathode temperatures. Cooling down one side of the cell while heating up the other side decelerates processes in the cold electrode while processes in the warm electrode are accelerated. Both effects will be visible in the resulting full cell impedance spectrum. A simple equivalent circuit model, consisting of two RC-elements in series has been used to analyse the corresponding full cell impedance spectra. It will be demonstrated how to assign the semicircles of the individual charge transfer reactions to the anode and the cathode. Troxler et al. [107] have used a similar set-up. However, they have set their focus on multi-layered cells which did not allow them to heat or cool the two electrodes separately. Therefore, an assignment of electrode contributions to anode and cathode has not been done yet. We verify the robustness of our method with measurements of two

batteries of the same type. The method is further supported by additional half-cell measurements. This investigation demonstrates a method to unambiguously identify the parameters of charge transfer processes at the electrodes in impedance based models. We will demonstrate that the new method can be used to assign parameters of simulations of full cell-spectra to the anode and the cathode. The study will demonstrate the feasibility of the method by assigning the temperature dependent relaxation times of two RC elements to the respective temperature dependent semi-circles of simulated impedance spectra.

4.2 Experimental

The experimental realisation has been done with the measurement setup depicted in figure 4.2. A single layered battery cell (graphite/NiMnCo-Oxide, NMC) has been placed between two Peltier elements. In figure 4.2, the anode is heated up and the cathode is cooled down. Temperatures have been measured with two PT 100 temperature sensors, which have been positioned between the Peltier elements and the anode and cathode side of the battery cell, respectively. Cooling rips and fans have been attached to the Peltier element at the cold side to increase the achievable temperature difference applied across the width of the cell. All measurements have been performed in a temperature chamber at 23 °C to ensure stable temperature. The temperature gradient across the cell is adjusted by the set temperature of the chamber and the current applied to the Peltier elements.

Two 60 mAh high energy density Lib cells produced by Custom Cells, denoted as cell I and cell II, with roughly 17 cm^2 NMC and graphite electrodes respectively have been analysed with a Gamry Reference 3000 potentiostat. Both cells had a Lithium titanate (LTO) reference electrode integrated for the half-cell measurements. All measurements have been performed at 50% SoC referred to the nominal capacity. Impedance spectra have been measured from $0.1\,\text{Hz} - 10^5\,\text{Hz}$ with an amplitude of 6 mA.

The cells have been stored at room temperature and 50% SoC between the measurements.

In a first measurement, the cathode was heated up while the anode was

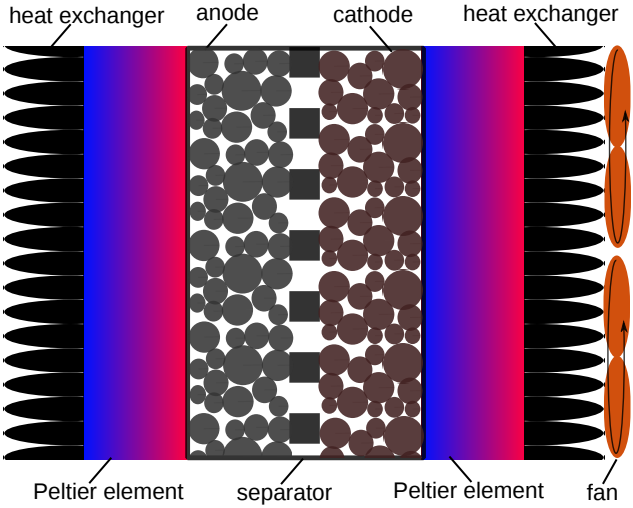

Figure 4.2: Schematic illustration of the measurement set-up

cooled down. An impedance spectrum has been measured after the measured temperatures had stabilised. This measurement is called Meas 1. Afterwards, the warm and cold sides have been switched and a second impedance spectrum has been measured, called Meas 2.

The actual temperature profile across the cell could not be measured but has been approximated from the temperature measurements at the battery surfaces. The Peltier elements were supplied with 6.6 A and 12 V, resulting in 74 °C at the hot side and 39 °C at the cold side.

4.2.1 Temperature distribution

Using the temperatures at the battery surfaces boundary conditions, the temperature profile within the cell can roughly be estimated. The results depend on the thermal conductivities and the thicknesses of the pouch cell bag and of the electrolyte soaked electrodes and the separator. Ther-

mal conductivities for similar cell materials have been used from literature. Based on the parameters presented in table 4.1, the temperature distribution shown in figure 4.3 has been calculated to roughly estimate the temperature distribution. Even though the temperature difference between anode and cathode is lower compared to the measured temperatures at the Peltier elements, it is still sufficient for our purpose because the impedance of a Li-ion cell is very sensitive to changes in temperature. Figure 4.3 shows that the estimated temperature of the anode (59 °C) is 5 °C higher than the temperature of the cathode (54 °C). The thermal conductivities of anode and cathode are similar and therefore the temperatures of the anode and cathode will approximately be switched after the pouch cell is turned between the Peltier elements.

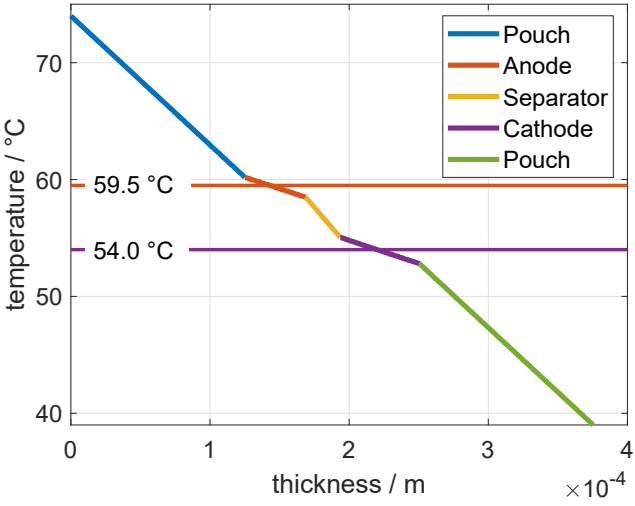

Figure 4.3: Estimated temperature profile across the width of a single layered Li-ion cell assuming a warm side of 74 °C and a cold side of 39 °C

4.3 Data Evaluation

The measurement results from Meas 1 and Meas 2 can not be evaluated directly. In the upcoming sections necessary simplifications and all steps

Material	conductivity $Wm^{-1}K^{-1}$	thickness μm
Pouch bag foil	0.25 [108]	500 [108]
Graphite	0.71 [109]	43.66 [71]
NMC	0.7 [109]	56.75 [71]
Separator	0.25 [108]	20 [71]

Table 4.1: Thermal conductivities and layer thicknesses within the LiB.

of the data evaluation are discussed. The data evaluation is additionally been displayed schematically in figure 4.5.

4.3.1 Simplifications

In order to be able to evaluate the experimental data, assumptions about the underlying physical processes have to be made to simplify the analysis. We assume that charge transfer at the anode and cathode depend differently on temperature. As a consequence, we expect that the change of the impedance at the anode and the change of the impedance at the cathode are likewise different if the temperatures of both electrodes are switched. Therefore, we have calculated the differences of the impedance spectra of the full cells Meas 1 and Meas 2 in terms of the moduli $|Z(f)|$ and the phases $\varphi(f)$ at each frequency f:

$$\Delta|Z|(f) = |Z_{Meas1}|(f) - |Z_{Meas2}|(f) \tag{4.1}$$

and

$$\Delta\varphi(f) = \varphi_{Meas1}(f) - \varphi_{Meas2}(f) \tag{4.2}$$

Note that henceforth we omit the frequency dependence of the impedances throughout this paper to improve readability. Following the definition of Meas 1 and Meas 2, the differences represent the effect of a warm cathode that is cooled down, superimposed by a cold anode that is heated up.

$$\Delta|Z| = (|Z_{\text{cold anode}} + Z_{\text{warm cathode}}|) - (|Z_{\text{warm anode}} + Z_{\text{cold cathode}}|) \tag{4.3}$$

$$\Delta\varphi = arctan\Big(\frac{(Im(Z)_{\text{cold anode}} + Im(Z)_{\text{warm cathode}})}{(Re(Z)_{\text{cold anode}} + Re(Z)_{\text{warm cathode}})}\Big) - \tag{4.4}$$

$$arctan\Big(\frac{(Im(Z)_{\text{warm anode}} + Im(Z)_{\text{cold cathode}})}{(Re(Z)_{\text{warm anode}} + Re(Z)_{\text{cold cathode}})}\Big)$$

Data evaluation is focused on the arc of the impedance spectrum that represents charge transfer across the electrolyte/electrode interfaces at the anode and the cathode. The shape of the measured arc is affected by several physico-chemical processes and properties of the cell. Basically, it is formed by the charge transfer resistances and the double layer capacitances, which would result in two superimposed semi-circles. However, solid state diffusion affects the low frequency part of the semi-circle and inductive and capacitive effects, induced by the wires or stray capacitances, can affect the high frequency part of the semicircle. Additionally, geometrical and material inhomogeneities lead to a distribution of time constants of the RC elements which flattens the arc [110], and the solid electrolyte interface at the electrode surface may further distort the arc. As a consequence, a comprehensive equivalent circuit to model the processes at the electrode is rather complex. For the purpose of this investigation we have to simplify the analysis of the spectra:

Reduction of measured spectra to charge transfer processes: Firstly, we have reduced the measured impedances of the full cells to extract the impedances of the charge transfer processes at the electrodes by subtracting impedance contributions caused by the internal resistance, diffusion and induction. Hereby, the frequency range is unchanged. These contributions were calculated with a parameter identification algorithm in Matlab which minimises the difference between the measured absolute impedances and the sum of the assumed impedance contributions. The charge transfer impedances are represented by a resistor in parallel to a constant phase element for this purpose [89]. The equivalent circuit for this extraction process is illustrated in figure 4.4a. Figure 4.4b shows the measurement results for Meas 1 and Meas 2 and the same results after

subtracting the impedance contributions of the internal resistance, diffusion and induction. The respective steps are depicted in the flow diagram in figure 4.5a.

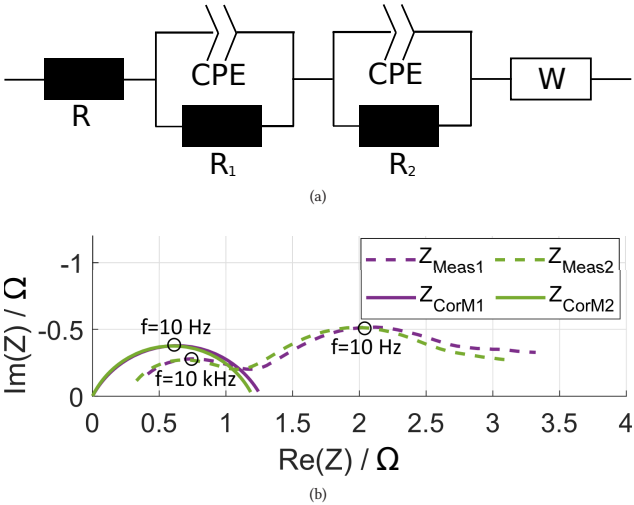

Figure 4.4: Reduction of electrochemical impedance spectra to charge transfer processes: a) Equivalent circuit model used to reduce the measured impedance to the charge transfer processes. b) Impedance of measurements 1 and 2 (dashed) and the corresponding reduced spectra after subtracting internal resistance, inductance and diffusion (solid)

We have further simplified the investigation hereafter by replacing the CPE, used to perform the reduction of the spectra, with two RC elements representing the two electrodes. Each of them consists of a charge transfer resistance R in parallel to a capacitance C. The latter is usually attributed to the double layer at the electrolyte/electrode interface. This simplification is done as the effect of a temperature change on the charge transfer processes at the electrodes can be understood more easily in terms of the charge transfer resistance and double layer capacitance compared to the rather abstract coefficients of CPE elements which cannot easily be assigned to physical quantities. Note that as the equivalent

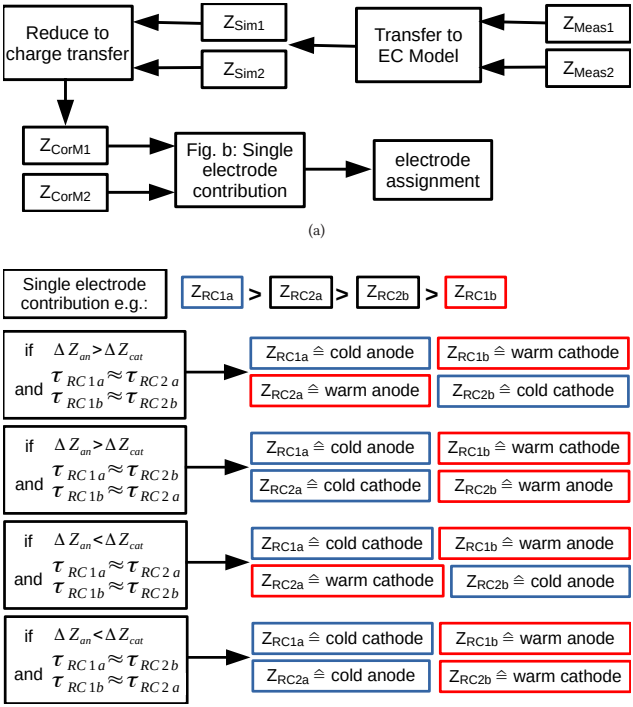

Figure 4.5: Schematic visualisation of the procedure to assign electrodes: a) Flow diagram from first measurement to electrode assignment. b) Block diagram: Four possible results for the differences of the impedances and the time constants (left) and the resulting electrode assignments (right).

circuit used to extract the electrode impedance (figure 4.4a) is only an approximation of the actual impedances of the processes in the cell, the reduced spectra, that are supposed to reflect just the electrode impedances, are subject to uncertainty. Likewise, the subsequent use of the simple RC elements introduces further uncertainty. These uncertainties are acceptable as the investigation only aims to identify the arcs of an impedance spectrum with respect to the anode and the cathode rather than providing an exact model of the cell impedances. We consider the reduced spectra and the simple RC model sufficient for the proof of concept in this manuscript, in particular, because we have substantiated the results by further validation steps in section 4.4.

4.3.2 Assumptions for temperature influence

In the following we will discuss the expected effects of a temperature change on electrodes that are modelled by RC elements.

Nonlinear temperature effects: Firstly, charge transfer reactions at an electrode and diffusion in the vicinity of the electrode/electrolyte interface accelerate with increasing temperature which decreases the charge transfer resistance of the electrode. We have measured the resistances of the charge transfer reactions of the electrodes of two cells with half-cell measurements at various temperatures and found a non-linear temperature dependence for the anode and the cathode. The results for temperatures between 5 °C and 26 °C are depicted in figure 4.6. It can be seen that the change in resistance due to a change in temperature is higher for high resistances than for low resistances. It has to be noted that the resistance of the two cells differ. We attribute this to the fact that they have been made exclusively for the purpose of this investigation. Cells produced in smaller numbers usually have higher cell to cell variations. Since the two cells are analysed independently of each other, the difference can be accepted for this study. The assignment of the electrode impedance contributions will be done for both cells.

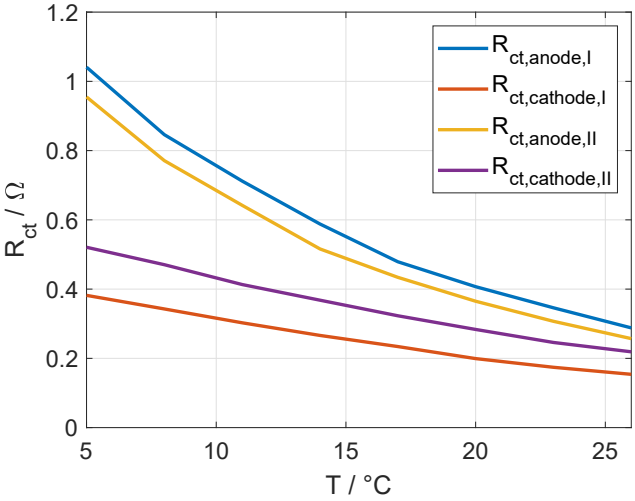

Figure 4.6: Charge transfer resistances of all electrodes of cell I and II at various temperatures.

Temperature dependence of parameters: Secondly, we assume that the temperature change mainly affects the charge transfer resistance rather than the double layer capacitance. The effect of temperature on the double layer capacitance is difficult to assess. The double layer forms to compensate differences in the chemical potentials of the electrode and the electrolyte at the electrode/electrolyte interface. These potentials also depend on temperature. However, the relative dependence of their difference on temperature is assumed significantly smaller than that of the charge transfer resistance. This assumption is supported by the findings of Ahmed and Bade Shresthra [111]. We did comparable calculations as Ahmed and Bade Shresthra for the half cell data of the cells used within this research and found a change of the double layer capacitance of only $\approx$ 5 % for each electrode after changing the temperature from 5 °C to 17 °C.

Temperature impact on time constants: Finally, we assume that the time constant related to the charge transfer process at the electrolyte/an-

ode interface and that related to the electrolyte/cathode interface are different but they are in the same order of magnitude. In other words, the relevant frequency ranges of the involved impedances which form the arc overlap significantly, but they are shifted against each other to some extent. This is a common property of full-cell impedance spectra.

4.3.3 Identification of the Electrodes

Based on the assumptions and the approach introduced in the previous sections, we will now describe the general procedure, how to identify the cathode and the anode in Z_{Meas1} and Z_{Meas2}, respectively. The measurements with the different temperature configurations Z_{Meas1} and Z_{Meas2} each include the impedance contributions of both, the anode and the cathode. As seen in equation 4.1, this leads to a total of four impedances affecting $\Delta|Z|$ and $\Delta\varphi$. This is exemplary shown in figure 4.7 for cell I. Z_{Meas1} is modelled with two RC-elements Z_{RC1a} and Z_{RC1b} in series, representing the two electrodes. Likewise, Meas 2 is modelled with Z_{RC2a} and Z_{RC2b}. A non-linear least square fitting procedure as proposed in [71] has been applied to minimise the difference between Z_{Meas1} and the sum of Z_{RC1a} and Z_{RC1b} as well as the difference between Z_{Meas2} and the sum of Z_{RC2a} and Z_{RC2b}. Please note that only the full cell experiments were used, not the half cell measurements. The simple model reproduces the experiments with sufficient accuracy for the analysis. Up to this point, Z_{RC1a}, Z_{RC1b}, Z_{RC2a} and Z_{RC2b} can not readily be assigned to the anode and cathode. This could easily be accomplished directly if the frequency ranges of the impedances contributing to the arcs do not overlap significantly. In this case, the investigation could be limited to one of the two frequency ranges. The RC-element with the impedance decreasing from Meas 1 to Meas 2 would be assigned to the anode and vice versa, because the anode has been heated up and the cathode been cooled down. However, usually the frequency ranges overlap significantly and the identification is more complex so that it cannot be decided unambiguously how the semi-circles have changed. Therefore, further steps must

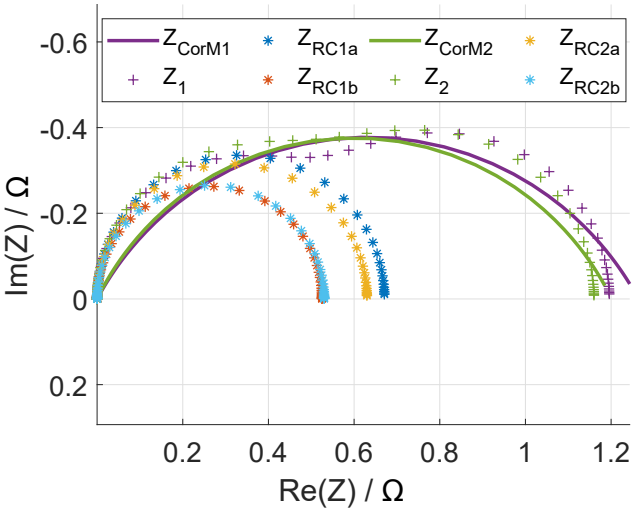

Figure 4.7: Reproduction of the reduced spectra from cell I: Z_{RC1a}, Z_{RC1b} represent the impedances of the RC elements of two electrodes of the first measurement, Z_1 their sum and Z_{CorM1} the corresponding (reduced) measured impedances. The impedances of the second measurement are denoted accordingly.

be considered in order to assign Z_{RC1a}, Z_{RC1b}, Z_{RC2a} and Z_{RC2b} to the electrodes and their corresponding temperature conditions. At low frequencies, the impedances of all four RC elements are dominated by the real part of the complex impedance. Hence, the behaviour of the real part of the impedances in this frequency range can aid in the identification process. The largest resistance must be assigned to a cold electrode, since its value must become smaller after heating up the electrode. Hence, if the largest resistance of Z_{RC1a}, Z_{RC1b}, Z_{RC2a} and Z_{RC2b} corresponds to measurement 1, where the cathode is heated, the cold anode must be assigned to the respective impedance. This is Z_{RC1a} in the example illustrated in figure 4.7. Consequently, Z_{RC1b} must obviously be assigned to the warm cathode. In turn, if the largest resistance corresponds to measurement 2 the cold cathode would be assigned accordingly. Next, the two remaining RC elements (Z_{RC2a} and Z_{RC2b} in our example) will be assigned which, at

this point, can not be uniquely attributed to cathode or anode since both fulfil the criterion that they are smaller than Z_{RC1a} and larger than Z_{RC1b}. To this end, the relaxation times $\tau = RC$ corresponding to each of the four impedances will be calculated from the resistances (R_{RC1a}, R_{RC1b}, R_{RC2a}, R_{RC2b}) and capacitances (C_{RC1a}, C_{RC1b}, C_{RC2a}, C_{RC2b}) that have been obtained from the fit. Since we assume that the double layer capacitance does not change significantly with temperature, we assign those impedances to the same electrode which has a similar capacitance. In our example the values shown in table 4.2 have been obtained. Thus, Z_{RC1a} and Z_{RC2a} are assigned to the anode and Z_{RC1b} and Z_{RC2b} are assigned to the cathode. The described procedure is schematically been shown in the block diagram in figure 4.5b.

	resistance Ω	capacitance F	time constant s	assignment
Z_{RC1a}	0.671	0.0311	$2.09 \cdot 10^{-2}$	cold anode
Z_{RC1b}	0.525	0.00466	$2.44 \cdot 10^{-3}$	warm cathode
Z_{RC2a}	0.630	0.0319	$2.00 \cdot 10^{-2}$	warm anode
Z_{RC2b}	0.530	0.00464	$2.46 \cdot 10^{-3}$	cold cathode

Table 4.2: Identified resistances and capacitances with the resulting time constants for cell I

4.3.4 Consistency Checks

Because of the uncertainties of the procedure that have been mentioned above, it is reasonable to conduct a few consistency checks to substantiate the results. First of all, it should be checked if the assigned impedance values comply with the expected temperature behaviour that we have described above. For frequencies $f \approx 0.1\,\mathrm{Hz}$, equation 4.3 can be ap-

proximated and rearranged such that

$$\begin{aligned}\Delta|Z| &= (|Z_{\text{cold anode}} + Z_{\text{warm cathode}}|) - (|Z_{\text{warm anode}} + Z_{\text{cold cathode}}|) \\ &\approx (R_{\text{cold anode}} + R_{\text{warm cathode}}) - (R_{\text{warm anode}} + R_{\text{cold cathode}}) \\ &= (R_{\text{cold anode}} - R_{\text{warm anode}}) + (R_{\text{warm cathode}} - R_{\text{cold cathode}})\end{aligned} \tag{4.5}$$

The first term on the right-hand side of equation 4.5 expresses the change of the resistance at the anode and the second term that of the cathode. Consequently, the sign of $\Delta|Z|$ is positive if the change of the resistance of the anode is greater than the change of the resistance of the cathode and vice versa. Thus, the RC element showing the larger change of the resistance must be assigned to the anode if $\Delta|Z|$ is positive. If $\Delta|Z|$ is negative it must be assigned to the cathode. Additionally, the cold electrode showing the larger resistance must show the larger change because of the non-linear temperature dependency described above. Looking at table 4.2, it can easily be checked that the assignments that we have made in our example comply with these requirements. $\Delta|Z|$ is positive at the low frequency end (calculated from equation 4.3), hence $R_{RC1a} - R_{RC1b}$ must be larger than $R_{RC2a} - R_{RC2b}$. This is schematically shown in figure 4.5b.

Finally, it should be verified if the measured frequency behaviour of $\Delta|Z|$ and $\Delta\varphi$ are consistent with the modelled frequency behaviour of the impedances of the RC elements and their assignments to the electrodes. This should further substantiate the results since the investigations have been based on the Nyquist-plots so far, which gives, besides the relaxations times, no direct information on the frequency behaviour of the involved impedances. To this end, $\Delta|Z|$ and $\Delta\varphi$ will first be calculated from Z_{RC1a}, Z_{RC1b}, Z_{RC2a} and Z_{RC2b}, and the assignments of these impedances to the warm and cold electrodes, using equation 4.3 are performed. The main features are depicted in figure 4.8, which shows the moduli of Z_1 and Z_2 and $\Delta|Z|$ on the left-hand side and their phases and $\Delta\varphi$ on the

right-hand side.

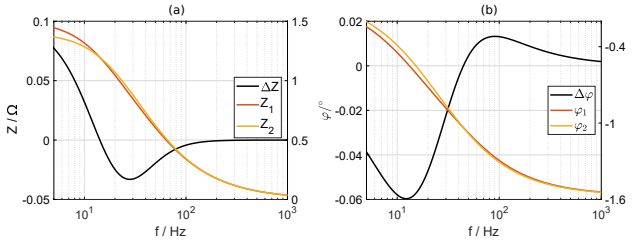

Figure 4.8: Simulation results of the introduced RC-element model. (a) Z_1 and Z_2 each represent the total impedance of two RC-elements and $\Delta|Z| = |Z_1| - |Z_2|$. The corresponding phases are depicted in (b).

The features of the individual RC elements (not shown) are well known. The moduli of the impedances start from the associated resistance values at low frequencies and level off to zero at the high frequency end, while the corresponding phases change from zero to $\pi/2$. The moduli and the phases of Z_1 and Z_2 show a similar behaviour. However, $\Delta|Z|$ and $\Delta\varphi$ can show quite different features, depending on the values of the involved resistances and capacitances. Figure 4.8 shows the features under the conditions that we have assumed, i.e.

- the resistance values are in the same order of magnitude
- the largest resistance is assigned to a cold anode
- the change of the resistance at the anode and the cathode is smaller than the difference of the anode and cathode resistance
- the double layer capacitance of the anode and the cathode are in the same order of magnitude
- the double layer capacitance at an electrode does not change significantly with temperature

The main features that can be observed are:

- $\Delta|Z|$ first decreases with increasing frequency. It is positive at the low frequency end because RC1a has been assigned to the cold

anode, i.e. the highest resistance. With increasing frequency, the moduli of Z_1 and Z_2 cross each other. As a consequence, their difference becomes negative, then it shows a minimum. At high frequencies, $\Delta|Z|$ gradually levels off to zero. If the highest resistance is assigned to the cold cathode, $\Delta|Z|$ would be negative at the low frequencies and it would show a maximum.

- $\Delta\varphi$ approaches zero at the low and high frequency end. It has a minimum at lower frequencies and a maximum at larger frequencies.

At the high frequency end, one could expect that ΔZ and $\Delta\varphi$ are dominated by the processes showing the smallest relaxation times, i.e. the warm electrodes since the slower processes do contribute less to the total impedance in this region. However, we have found that the significant overlap of the frequency ranges of the four impedances involved, including eight parameters, make is difficult to assign specific features seen in the high frequency range to the warm electrodes. In the next section, we will now apply the described data evaluation procedure to our measured data.

4.4 Method application to experimental data

We have performed the procedure described in section 4.2 and section 4.3 with two cells of the same type in order to verify the reproducibility. The spectra already shown in figures 4.4b and 4.7 depict the results of cell I. The spectra of cell II (not shown) have a comparable behaviour. Tables 4.2 and 4.3 list the identified values of the four RC impedances Z_{RC1a}, Z_{RC1b}, Z_{RC2a} and Z_{RC2b} for cell I and cell II, respectively. Following the reasoning of the simulations made in section 4.3.3, Z_{RC1a} and Z_{RC2a} of the measurement have to be assigned to the anode and Z_{RC1b} and Z_{RC2b} have to be assigned to the cathode. The absolute resistance and capacity values of the two cells differ to some extent due to manufacturing variability and possible additional errors from the simplifications described in sec-

	resistance Ω	capacitance F	time constant s	assignment
Z_{RC1a}	0.654	0.0282	$1.84 \cdot 10^{-2}$	cold anode
Z_{RC1b}	0.163	0.00534	$8.70 \cdot 10^{-4}$	warm cathode
Z_{RC2a}	0.595	0.0285	$1.70 \cdot 10^{-2}$	warm anode
Z_{RC2b}	0.172	0.00532	$9.15 \cdot 10^{-4}$	cold cathode

Table 4.3: Identified resistances and capacitances with the resulting time constants for cell II

tion 4.3.2.

Figures 4.9a and 4.9b show the frequency behaviour of $\Delta|Z|$ and $\Delta\varphi$ of cell I and cell II, respectively. Qualitatively, their frequency behaviours fit well to the simulation results illustrated in figure 4.8. $\Delta|Z|$ is positive at the low frequency end, decreases with increasing frequency, changes its sign in the mid frequency range and shows a minimum before its starts to level off. The phase difference shows a minimum and rises above zero to another maximum, which seems to be beyond the investigated frequency range for cell II. Therefore, the analysis of the frequency dependency of the measurement data supports or, at least, does not falsify the conclusion that the anodes in the measured cells have a higher charge transfer resistance and a higher time constant than the cathode. The frequency behaviour of $\Delta|Z|$ and $\Delta\varphi$ of both cells are qualitatively the same which substantiates the robustness of the procedure qualitatively.

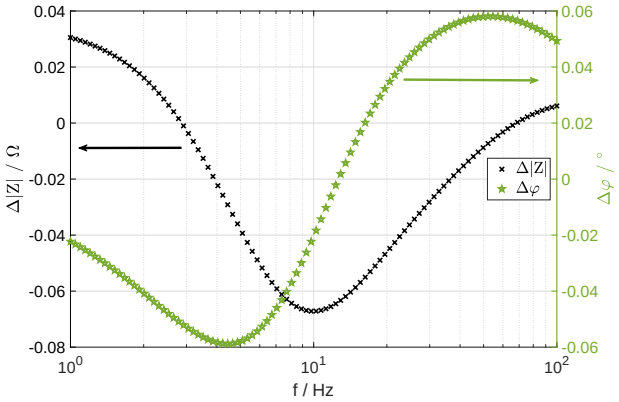

(a) Cell I

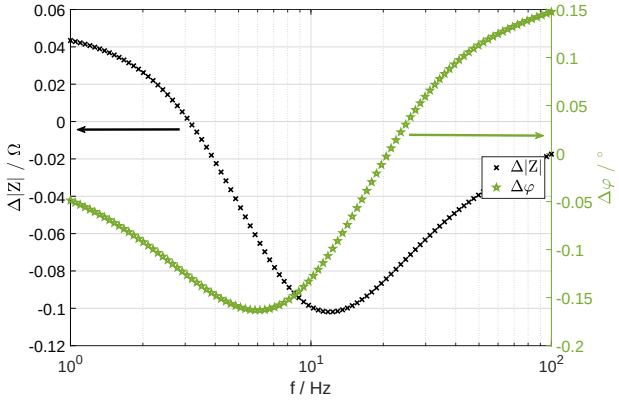

(b) Cell II

Figure 4.9: Differences between Meas 1 and Meas 2 for the impedance (black ✖, calculated with equation 4.1) and the phase angle (green ★, calculated with equation 4.2) with a temperature gradient from $\approx 54.0\,^{\circ}\mathrm{C} - 59.5\,^{\circ}\mathrm{C}$

4.5 Validation of the assignments with half cell measurements

Half-cell measurements have been additionally performed to verify the attribution of electrodes and thus our methodology. To this end, the anode and cathode impedances have been simultaneously measured with the impedances of the full cell to determine the relaxation times of the related charge transfer impedance independently. It should be noted that the sum of the imaginary parts of the half-cell measurements equal those of the corresponding full-cell measurements, which also holds for the sum of the real parts. This proves that the three-electrode arrangement cell can be used to split the measured full-cell impedances into the contributions of the individual electrodes. The untreated results are shown in figures 4.10a and 4.10b which depict the imaginary parts of the impedances over the frequency. The reciprocal of the characteristic frequency at the minimum of the imaginary part corresponds to the relaxation time of the charge transfer impedance of an electrode, assuming that it is determined by the behaviour of an RC element as described in section 4.3.1. Table 4.4 lists the relaxations times of the electrodes under warm and cold conditions and compares them to those derived by our method. The relaxation times derived from the half-cell measurements confirm the assignment of relaxations times to anode and cathode from the full-cell measurements. The differences in absolute values may be attributed to our simplifications as mentioned above. Nevertheless, the half-cell measurements support the simulated results, in particular, that the anode has a higher charge transfer resistance and a higher relaxation time.

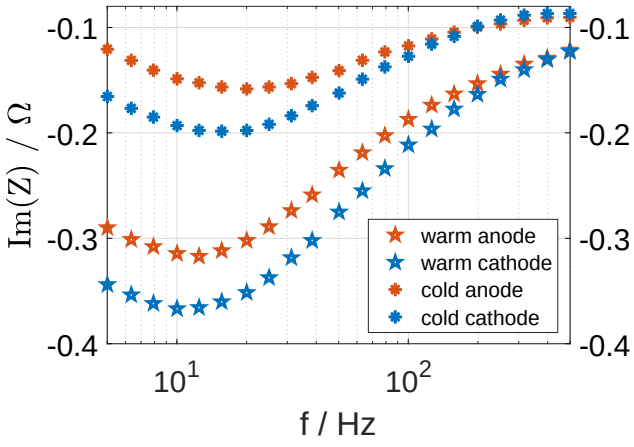

(a) Cell I

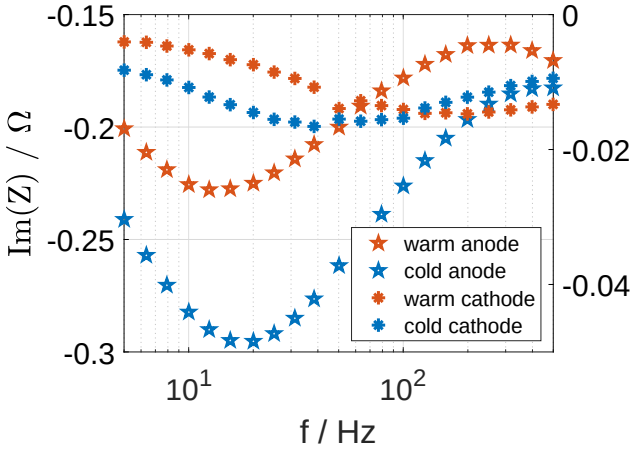

(b) Cell II

Figure 4.10: Imaginary part of the impedance for half cell measurements with a temperature distribution from $\approx$ 54 °C – 59 °C. Left axis shows anode values and right axis shows cathode values

	time constants of the simulation in seconds			
	cold cathode	warm anode	cold anode	warm cathode
Cell I	0.002	0.020	0.021	0.002
Cell II	0.001	0.017	0.018	0.001
	time constants of the experiment in seconds			
	cold cathode	warm anode	cold anode	warm cathode
Cell I	0.011	0.013	0.013	0.008
Cell II	0.004	0.011	0.008	0.002

Table 4.4: Comparison of measured and simulated relaxation times (all given in seconds) of both electrodes of both cells

4.6 Concluding Remarks

A new method which enables to assign anode and cathode impedance contributions solely with measurements on full cell LiBs has been introduced. A temperature gradient is applied on a single layered Li-ion battery cell and exploits different dependences of the anode and cathode charge transfer processes on temperature. Feasibility has been demonstrated by reproducing the measurement results with a simple model of RC elements showing that the method is suitable to decide if the identified parameters of an electrode process used for the simulation should be assigned to the anode or the cathode. The assignment has been substantiated by further consistency tests and been proven with half-cell measurements. Knowledge about the anode and cathode contributions to the overall full cell behaviour improves the possibility to evaluate various kinds of characterisation measurements. Impact of changes of the measurement conditions i.e. temperature, SoC or SoH can be assigned to a specific electrode more easily if the introduced method is applied in advance. The method might be optimised by increasing the temperature gradient across the cell, by decreasing the effects disturbing the electrode impedances or by measuring the impedances at various temperatures. However, once the impedance contribution of a specific process is assigned to its related electrode, this information can be used for more so-

phisticated models to simulate the impedance spectra of other cells of the same cell chemistry, cell balancing and electrode particle sizes.

5 Parameter identification in ageing LiBs[1]

In the previous chapter a method has been presented which can be used to identify anode and cathode contributions to full cell impedance spectra. Although it was made clear that such an assignment is essential, the presented method can only be applied to single-layered cells at the current state of research. Nevertheless, the successful assignment shows that suitable assumptions about the physical processes within a LiB can be used to identify the anode and cathode contributions. In the upcoming chapter, such an approach is used again. Instead of using the temperature dependency of the reactions, information about coupled reactions is used to make an assignment of full cell impedance spectra to the anode and cathode contributions. Electrochemical Impedance Spectroscopy measurements and simulations are performed on a NMC/graphite pouch cell. A physico-chemical continuum battery model is extended by a physical ageing model including a Solid Electrolyte Interphase. The model assumes a loss of electrochemically active surface area at anode and cathode as well as a growth of SEI layer thickness. These ageing parameters have been adjusted with an algorithm to achieve agreement between simulated and measured spectra. The results for a 28 mAh pouch cell show that the ageing model is suitable to correlate the change of the impedance spectrum with the degree of degradation of the cell. In detail, SEI thickness is shown to increase by 45 nm, while the anode and cathode loose 20 % and 57 % of their electrochemically active surface area, respectively. In addition, deviating measurement conditions and the End Of Life of the cell can be indicated by the parameter identification algorithm. Furthermore, it is demonstrated, that the change of the high and low frequency

[1] Part of this chapter was published in: Heinrich et al., "Physico-Chemical Modeling of a Lithium-Ion Battery: "An Ageing Study with Electrochemical Impedance Spectroscopy", *Batteries & Supercaps*, vol. 2, no. 2, pp. 530-540, 2019. The paper has been written by Marco Heinrich and Nicolas Wolff. Both authors contributed equally. The literature review and the discussion of the results was done by Marco Heinrich. The model derivation was done by Nicolas Wolff. The parameter identification was performed by Marco Heinrich and Nicolas Wolff. All measurements were conducted by Nina Harting.

semicircles can be assigned to the anode SEI and cathode respectively.

5.1 Introduction

Due to their high energy density, Lithium-ion batteries (LIBs) have a wide field of application as energy storage technologies and therefore have challenged many research groups to improve performance and to overcome current limitations. Efforts have been undertaken to increase the understanding of degradation processes to be able to increase the cells durability and long-term stability. Another key aspect is to know or at least to predict the End of Life (EoL) of cells in use. In most LIBs graphite is used as anode material since its redox potential versus Li+/Li as well as its costs are low. The electrolyte is operated outside its electrochemical stability window and it is therefore being reduced at the anode during cycling. The reduction reaction leads to the growth of a passivating Solid Electrolyte Interphase on the anode particles which protects the electrolyte from further reduction. This SEI is believed to be the dominating effect for an increase of cell impedance and a loss of capacity [10]. Therefore, most research neglects all other degradation processes and focuses on the impact of the SEI. Electrochemical Impedance Spectroscopy (EIS), as a widely used technique to characterise electrochemical systems, is able to reveal ageing induced changes. If processes with different time constants are affected by ageing, they can be revealed at their characteristic frequencies in the impedance spectrum. Impedance spectra of LIBs usually show one or two semicircles in the Nyquist plot. The semicircle with the smaller time constant is often assigned to processes in the SEI and the semicircle with the larger time constant to the charge transfer reactions in anode and cathode [23]. Non-linear frequency response is a further dynamic analysis method yielding complementary helpful insight into the battery state, i.e. State of Charge (SoC) and degradation [18]. However, interpretation of resulting spectra is more challenging than in EIS due to the lack of experience. Model-based analysis is presently used

to reveal the impact of cell design parameters on such spectra [112].

In order to gain deeper insight into the processes using EIS, two different types of model approaches are encountered in literature: On the one hand Equivalent Circuit Models (ECMs), and on the other hand continuum models based on physico-chemical equations. ECMs need low computational effort and can easily be used to fit simulations to measurement results, which enables an immediate parameter estimation. Nevertheless, ECMs are ambiguous in the assignment of electric circuit components to physical processes as they are phenomenological, empirical models. Continuum models are a more powerful and more physical alternative to get deeper insight into the cell. Also, physics-based models are less prone to over-fitting than ECMs, which is a crucial advantage for parameter identifications, as conducted in this chapter. Doyle et al. [113] have been the first to introduce a continuum model, known as the Newman-model, based on the theories of porous electrodes and concentrated solutions. In order to simulate EIS of such a physico-chemical model, the charging and discharging of double layers has to be included. This has been implemented by Ong et al. [114] and later by Legrand et al. [57].

To analyse ageing phenomena, such models need to be extended by an ageing model including a SEI that accounts for changes due to ageing. Most of the following works though do not analyse the ageing impact on the impedance spectrum. The common assumption that the SEI consists of a dense inner and a porous outer layer is based on the work of Peled et al. [115] in which the physical properties of the SEI are explained. Further, Peled et al. [115] achieved agreement between measured impedance results and an ECM. Based on this work, Gao et al. [116] used a Point Defect Model (PDM) which has been introduced by Macdonald [117] to describe transport processes within the SEI. Using this PDM, Gao has been able to simulate the influence of the SEI on metal surfaces on the impedance spectrum. In order to further analyse the SEI, Nainville et al. [118] developed a model which simulates the growth of the SEI on Lithium anodes. The model does not lead to a quantitative comparison

with any experimental results but describes the early growth of the SEI. Broussely et al. [119] extended the prior model and used a full Lithium-ion battery model focusing on calendar ageing. The work of Nainville and Broussely revealed how to store batteries with a minimum of capacity loss. In 2004, Christensen et al. [69] published results for the growth of the SEI at various states of charge with an isothermal physics-based calendar ageing model. At the same time, Ramadass and Ning introduced and applied the currently used model to simulate the growth of the SEI during cyclic ageing [120, 121, 64]. Based on the model introduced by Christensen, Colclasure et al. [122, 70] developed a thermodynamically consistent model considering the detailed chemistry of the SEI growth for a Single Particle (SP) model of the anode. This approach has been used by Röder who combined it with a kinetic Monte Carlo model to perform multi-scale simulations of the SEI formation [123]. Zavalis did not use a detailed model like Christensen and Colclasure but achieved agreement between simulations and measurement data during ageing [21]. In one of the few works including a model-based analysis of the ageing impact on the impedance spectrum, Xie et al. [20] adjusted simulation parameters of a battery model to investigate impedance data from cycle-aged coin cells. For their research Xie et al. [20] used the model for the SEI growth introduced by Ramadass et al. [120, 121] which does not include any transport phenomena nor any reactions within the SEI during an impedance simulation. The current research either focuses on the growth of the SEI and the transport processes within it or on the analysis of the change of battery parameters during ageing using EIS. A detailed model-based study of the ageing dependent processes at the SEI using impedance spectroscopy will combine the deep insights obtainable from both, physical modelling and EIS. To the best knowledge, here the first such study is presented.

In this chapter, it is aimed to determine and monitor ageing processes by applying a parameter identification (PI) algorithm with ageing-correlated parameters in order to correlate an exemplary set of measurement data at different States of Health (SoH) of an in-house made battery cell with the

simulation results. The detailed thermodynamic approach introduced by Colclasure [122] is used and the focus is set on the altering influence of the SEI on the impedance spectrum instead on the growth process itself. In contrast to the model presented by Colclasure, a full cell SP model with simplifications in the amount of considered reactions is used and diffusion processes in the SEI are neglected. Further, instead of using a side reaction current for the SEI growth, an ageing model is introduced and applied, in order to identify the progression of cell and ageing parameters with time, using EIS. The model includes a double layer at the SEI/electrolyte interface in addition to the double layer at the particle/SEI interface. The reactions, taking place at those interfaces, are coupled which is a drastic change compared to equivalent circuit modelling, where the impedance of each process is independent of every other process. Further, the loss of lithium during the formation and the loss of active material due to particle cracking and due to a loss of connectivity between the active materials and the current collectors are implemented. Both losses are assumed to change the allocation of lithium in anode and cathode. Therefore, the SoC changes and the resulting impedance spectrum is affected. In addition to that, the isolating effect of the SEI is considered in the model. The first impedance simulations on such a model are presented and the fact that the model is suitable to provide detailed information on the change of ageing parameters during degradation and enabling a physical-based interpretation of this change is shown. This approach enables a state estimation at various states of health and it might also be suitable to indicate the EoL of the cell. The focus of this chapter lies in the implementation of the new ageing model including the state estimation of an exemplary chosen cell. Validation of the model with various cycling conditions or predicting the exact capacity after a specific amount of cycles is open for future research. Nevertheless, it is shown that the method provides a significant improvement to the classical analysis of impedance and capacity values.

5.2 Experimental

The LiB pouch-cell used to obtain an exemplary set of experimental data consists of NMC as cathode and graphite as anode material. Only one cell is tested to gain experimental data from a well known cell. No comparison with different cycling conditions have been done since the scope of this work ends with the introduction of the novel ageing model and the state estimation of the used cell. All measurements have been conducted by Nina Harting. A detailed explanation of the cell and the measurement is given in [71].

Parameter	Anode	Separator	Cathode
Width δ / μm	43.66 (a)	20.00 (a)	56.75 (a)
Particle radius R_i / μm	6.83 (a)	-	6.40 (a)
Volume fraction solid ε_s / -	0.35 (b)	-	0.33 (b)
Volume fraction electrolyte ε_e / -	0.60 (b)	0.5 (b)	0.57 (b)
Max. solid concentration $c_{s,max}$ / $\frac{mol}{m^3}$	28605.42 (b)	-	50862.18 (b)
Electrolyte concentration c_e / $\frac{mol}{m^3}$	1000 (a)	1000 (a)	1000 (a)
Transfer coefficients α / -	0.50 (c)	-	0.50 (c)
Electrolyte phase diff. coeff. D_e / $\frac{m^2}{s}$	$2.6 \cdot 10^{-10}$ (c)	$2.6 \cdot 10^{-10}$ (c)	$2.6 \cdot 10^{-10}$ (c)
Solid phase diffusion coeff. D_s / $\frac{m^2}{s}$	$2.0 \cdot 10^{-16}$ (c)	-	$3.7 \cdot 10^{-16}$ (c)
Transference number t_p / -	0.37 (c)	-	0.37 (c)
Bruggeman's exponent β / -	1.50 (c)	1.50 (c)	1.50 (c)
Reaction rate constant $k_{f,a}$ / $\frac{m^{2.5}}{mol^{0.5}s}$	10^{-7} (d)		

Table 5.1: Fixed model parameters: (a) measured, (b) calculated according to [124] (c) literature value from [57], (d) literature value from [70]

5.3 Modeling[2]

A SP full cell battery model including a SEI (SP-SEI) at the anode side, schematically shown in figure 5.1, is derived in this section. The geometry underlying the model is illustrated in figure 5.1. It consists of a negative electrode, a positive electrode and a separator in between. Both electrodes are assumed to be porous. Electrodes and separator are not

[2]The initial model has been set up by Fridolin Röder and been extended in cooperative work with Nicolas Wolff who also provided the graphic shown in figure 5.1.

discretised in x-direction for this study to focus on the analysis of the main effects. Modelled spherical active material particles are radially discretised. On the anode side, an additional SEI layer is implemented as shown in figure 5.1b [125]. During the charging process a solvated Lithium-ion, originating from the electrolyte phase, enters the interfacial area (IFA) between liquid electrolyte and solid electrolyte, where it loses its solvate layer. This process is analogously described to a charge transfer reaction and is displayed in figure 5.1c as a potential drop. Next to the interfacial area, the SEI is present and an Ohmic potential distribution causing a linear potential drop is assumed. At the particle-SEI interface, Lithium electrochemically reacts and intercalates in a next step into the active material particle. The IFA, in contrary to the SEI, is not modelled with a dimension in x-direction since it is included in order to calculate the adsorption process only. Therefore the IFA does not have a thickness.

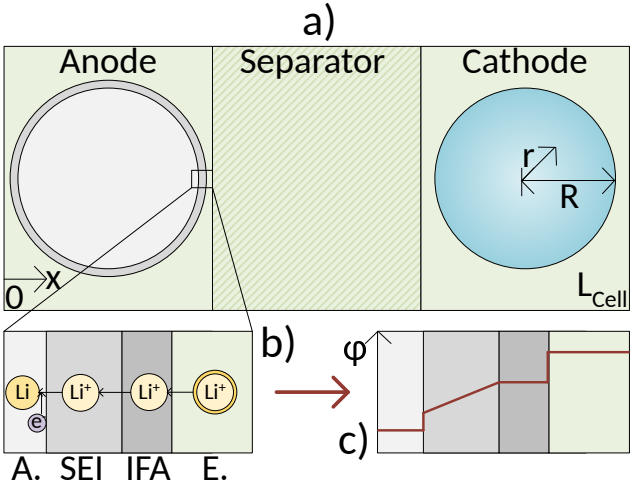

Figure 5.1: Schematic illustration of a) a SP-battery model including b) a magnified illustration of the anode particle/SEI/electrolyte interface region and c) the corresponding potential distribution

5.3.1 Single Particle Model

The phenomenon of solid state diffusion within active material particles is described by Fick's second law. It is formulated using radial coordinates with the radius r to account for the spherical shape of the active material particles.

$$\frac{\partial c_s}{\partial t} = \frac{1}{r^2}\frac{\partial}{\partial r}\left(D_s r^2 \frac{\partial c_s}{\partial r}\right) \tag{5.1}$$

Using c_s as solid concentration and D_s as solid Diffusion coefficient. At the center of the particle, $r = 0$, the concentration gradient is set to zero. The flux across the outer particle boundary, $r = R$, is set to the Lithium-ion reaction flux j_{Li}.

The charge flux J_k, by the species $k = \{Li^+, PF_6^-\}$, is calculated with a Nernst-Planck flux, with the convection term set to zero:

$$J_k = \underbrace{D_k \frac{\partial c_k}{\partial x}}_{\text{Diffusion}} + \underbrace{D_k^{\text{mig}} \frac{\partial \Phi}{\partial x}}_{\text{Migration}}, \tag{5.2}$$

with the potential Φ and the potential induced transport coefficient D_k^{mig}:

$$D_k^{\text{mig}} = \frac{z_k F c_k(x,t) D_k}{RT}, \tag{5.3}$$

with the valence of ions z_k, the Faraday constant F, the gas constant R and the cell temperature T. Combining equation 5.2 with the continuity equation

$$\frac{\partial c_k}{\partial t} = -\frac{\partial J_k}{\partial x}, \tag{5.4}$$

leads to a material balance equation for the species concentration c_k with $k = \{Li^+, PF_6^-\}$ in the bulk of the electrolyte:

$$\frac{\partial c_k}{\partial t} = \frac{\partial}{\partial x}\left(D_k \frac{\partial c_k}{\partial x}\right) + \frac{\partial}{\partial x}\left(D_k^{\text{mig}} \frac{\partial \Phi}{\partial x}\right) \tag{5.5}$$

A system with two oppositely charged species Li^+ and PF_6^- is present. Since electroneutrality $\sum z_k c_k = 0$ within the electrolyte is assumed, c_{Li^+}

and $c_{PF_6^-}$ are equal and the migration term cancels out [126]. To consider the effect of the Lithium reaction, a source term is added, which couples the equations for solid and electrolyte diffusion. Therefore, the overall change in electrolyte concentration c_e is provided by the material balance in equation 5.6.

$$\frac{\partial c_\mathrm{e}}{\partial t} = D_\mathrm{e}\frac{\partial^2 c_\mathrm{e}}{\partial x^2} + (1-t_\mathrm{p})\frac{j_{\mathrm{Li},m}}{F}, \tag{5.6}$$

with $m = \{\mathrm{c,a}\}$ for cathode and anode respectively. A concentration gradient of zero is assumed at $x = \{0, L_\mathrm{cell}\}$. The electrolyte diffusion coefficient D_e and the transference number t_p are being calculated as [113]:

$$D_\mathrm{e} = \frac{2D_{\mathrm{Li}^+}D_{PF_6^-}}{D_{\mathrm{Li}^+} + D_{PF_6^-}}, \tag{5.7}$$

$$t_\mathrm{p} = \frac{D_{\mathrm{Li}^+}}{D_{PF_6^-} + D_{\mathrm{Li}^+}}, \tag{5.8}$$

with the Diffusion coefficients of positively D_{Li^+} and negatively $D_{PF_6^-}$ charged species.

The flux of Lithium-ions $j_{\mathrm{Li,c}}$ at the cathode side in equation 5.6 is calculated with the Butler-Volmer equation.

$$j_{\mathrm{Li,c}} = a_{\mathrm{s,c}} j_{0,\mathrm{c}} \left(\exp\left(\alpha_\mathrm{c}\frac{\eta_\mathrm{c}\mathrm{F}}{\mathrm{R}T}\right) - \exp\left((1-\alpha_\mathrm{c})\frac{\eta_\mathrm{c}\mathrm{F}}{\mathrm{R}T}\right)\right), \tag{5.9}$$

with the cathode reaction symmetry factor α_c, the overpotential η_c and the specific surface area $a_{\mathrm{s,c}}$, which is defined as,

$$a_{\mathrm{s,m}} = \frac{3\varepsilon_{\mathrm{s,m}}}{R}, \tag{5.10}$$

with the solid phase volume fraction ε_s and the particle radius R.

A concentration dependent exchange current density $j_{0,\mathrm{c}}$ is implemented with respect to the maximum concentration in the cathode $c_{\mathrm{max,c}}$ [122].

$$j_{0,\mathrm{c}} = k_\mathrm{c}\mathrm{F}c_\mathrm{e}^{\alpha}\left(c_{\mathrm{max,c}} - c_{\mathrm{s,c}}\right)^{\alpha} c_{\mathrm{s,c}}^{1-\alpha}, \tag{5.11}$$

with k_c as the reaction rate constant, $c_{s,c}$ as the concentration in the cathode and c_e as Lithium concentration in the electrolyte.
At the interfaces between anode/SEI, electrolyte/SEI and cathode/electrolyte, shown in figure 5.1, the overall current splits up into a reaction current $j_{Li,i}$ and a double layer charge current $j_{DL,i}$. Therefore, additionally to the reaction flux, defined in equation 5.9, a flux into the double layer has to be calculated.

$$j_{DL,i} = a_{s,i} C^{DL_i} \frac{\partial \Delta\Phi_i}{\partial t}, \tag{5.12}$$

with C^{DL} as the active material area-related double layer capacitance and $\Delta\Phi$ as the potential difference between the two phases. The time derivation is causing a phase shift between current and voltage which leads to the imaginary parts in the impedance.

5.3.2 Implementation of the SEI

At the anode side of the model, a SEI is implemented. The entering of Lithium-ions into the interfacial area between solid and liquid electrolyte might be closely related to the skimming of their solvate layer [127]. Yamada et al. [128] reported that this might be the rate-determining step, but no further research on this topic has been reported yet. The reaction can be described as:

$$Li^+ + V_{Li} \rightleftharpoons Li^+_{IFA}, \tag{5.13}$$

with V_{Li} as vacancies at the IFA [122]. Afterwards the Lithium-ions enter the SEI from the IFA.

$$Li^+_{IFA} \rightleftharpoons Li^+_{SEI} + V_{Li} \tag{5.14}$$

This reaction is directly coupled with a charge-transfer reaction at the SEI/particle interface to enforce charge neutrality within the SEI.

$$Li^+ + e^- \rightleftharpoons Li \tag{5.15}$$

The ion flux resulting from these coupled processes is calculated with equation 5.16 according to [129],

$$j_{\mathrm{Li,a}} = \frac{c_{\mathrm{Li,a}}\gamma_{\mathrm{Li}}\lambda_{\mathrm{a,SEI}}\lambda_{\mathrm{SEI,IFA}} - c_{\mathrm{Li,IFA}}\gamma_{\mathrm{V}}\lambda_{\mathrm{SEI,a}}\lambda_{\mathrm{IFA,SEI}}}{\lambda_{\mathrm{SEI,a}} + \lambda_{\mathrm{SEI,IFA}}}, \tag{5.16}$$

with $c_{\mathrm{Li,IFA}}$ as Lithium-ion concentration at the interfacial area, $c_{\mathrm{Li,a}}$ as Lithium concentration at the surface of the active material particle and $j_{\mathrm{Li,a}}$ as the volume specific current generated by the coupled reactions 5.14 and 5.15. The activity coefficients of the Lithium γ_{Li} and the vacancies γ_{V} are calculated using a Redlich-Kister approach according to [122]:

$$\gamma_{\mathrm{Li}} = \exp\left(\frac{1}{\mathrm{R}T}\left(1-y_{\mathrm{a}}\right)^2 \sum_{i=1}^{11} A_i \left(2y_{\mathrm{a}}-1\right)^i \left(1+\frac{2iy_{\mathrm{a}}}{2y_{\mathrm{a}}-1}\right)\right), \tag{5.17}$$

$$\gamma_{\mathrm{V}} = \exp\left(\frac{1}{\mathrm{R}T} y_{\mathrm{a}}^2 \sum_{i=1}^{11} A_i \left(2y_{\mathrm{a}}-1\right)^i \left(1+\frac{2i(1-y_{\mathrm{a}})}{2y_{\mathrm{a}}-1}\right)\right), \tag{5.18}$$

with $y_{\mathrm{a}} = c_{\mathrm{a}}/c_{\mathrm{max,a}}$ and A_i as Redlich-Kister parameters, which are listed in the appendix 11.2. To solve equation 5.16, the reaction coefficients $\lambda_{\mathrm{a,SEI}}$, $\lambda_{\mathrm{SEI,a}}$, $\lambda_{\mathrm{SEI,IFA}}$ and $\lambda_{\mathrm{IFA,SEI}}$ are needed. The index a,SEI equals the forward and the index SEI,a the backwards main charge transfer reaction. The indices SEI,IFA and IFA,SEI are used in the same manner for the concentration dependent reaction. The following reaction kinetics are assumed:

$$\lambda_{a,SEI} = a_{s,a} \cdot k_{f,a} \exp\left(\alpha_a \Delta\Phi_a \frac{\mathrm{F}}{\mathrm{R}T}\right), \tag{5.19}$$

$$\lambda_{SEI,a} = a_{s,a} \cdot k_{b,a} \cdot \exp\left(-\left(1-\alpha_a\right)\Delta\Phi_a \frac{\mathrm{F}}{\mathrm{R}T}\right), \tag{5.20}$$

$$\lambda_{SEI,IFA} = a_{s,IFA} \cdot k_{f,SEI} \cdot \Theta_v, \tag{5.21}$$

$$\lambda_{IFA,SEI} = a_{s,IFA} \cdot k_{b,SEI}, \tag{5.22}$$

with the reaction rate constants $k_{f,a}$, $k_{b,a}$, $k_{f,SEI}$ and $k_{b,SEI}$ for each forward and backward reaction, α_a as reaction symmetry factor and with the vacant surface sites Θ_v.

The ion flux generated from the reaction in equation 5.13 can be expressed with the following equations by introducing the fraction of surface sites occupied by Lithium ions Θ_{Li}.

$$\begin{aligned} j_{\mathrm{Li,IFA}} &= \Theta_{\mathrm{v}} \cdot a_{\mathrm{s,IFA}} \cdot c_{\mathrm{Li,e}} \cdot k_{\mathrm{b,IFA}} \exp\left(-(1-\beta)\,\Delta\Phi\frac{\mathrm{F}}{\mathrm{R}T}\right) \\ &\quad -\Theta_{\mathrm{Li}} \cdot a_{\mathrm{s,IFA}} \cdot k_{\mathrm{f,IFA}} \exp\left(\beta\Delta\Phi\frac{\mathrm{F}}{\mathrm{R}T}\right) \end{aligned} \tag{5.23}$$

The reaction might not be exponentially dependent on the overpotential but linear dependent instead, but for impedance simulations no significant change in the results can occur since the excitation has to lead to a linear system response anyway. The assumption of an exponential potential depended transport of charged species from the liquid electrolyte to the solid electrolyte is based on the results presented by Kitazumi et al. [130].

5.3.3 Ageing Model

During ageing, the internal resistance of the cell increases. In order to account for this increase, the SEI thickness d_{SEI} is assumed to cause a potential drop which is dependent on the conductivity σ_{SEI}:

$$\Delta\Phi_{\mathrm{SEI}} = \frac{d_{\mathrm{SEI}}}{\sigma_{\mathrm{SEI}}} J_{\mathrm{Li}} \tag{5.24}$$

The initial thickness of the SEI, which is formed during the formation of the battery, is calculated according to:

$$d_{\mathrm{SEI,init}} = \frac{V_{\mathrm{SEI}} R_{\mathrm{a}}}{3\varepsilon_{\mathrm{s,a}} A_{\mathrm{cell}} d_{\mathrm{a}}} \tag{5.25}$$

The assumption, that 15 % of the Lithium, which deintercalates the cathode during the first charge will build up an initial SEI in the formation process instead of intercalating into the anode [131] is used. This initial

SEI is assumed to be composed of pure Lithium carbonate.

$$V_{\mathrm{SEI}} = \frac{n_{\mathrm{loss}} M_{\mathrm{Li_2CO_3}}}{2\rho_{\mathrm{Li_2CO_3}}}, \tag{5.26}$$

with the amount of lost mol Lithium n_{loss} and the molar mass and density of Lithium carbonate $M_{\mathrm{Li_2CO_3}}$ and $\rho_{\mathrm{Li_2CO_3}}$ respectively. The capacity decrease of the cell during cycling is accounted for by a loss of active material in anode and cathode of equal amount corresponding to a loss in active material fraction $\varepsilon_{\mathrm{loss}}$ at anode and cathode.

$$\varepsilon_{\mathrm{s,a,age}} = \varepsilon_{\mathrm{s,a}} - \varepsilon_{\mathrm{loss}}, \tag{5.27}$$

$$\varepsilon_{\mathrm{s,c,age}} = \varepsilon_{\mathrm{s,c}} - \varepsilon_{\mathrm{loss}}, \tag{5.28}$$

with the solid phase volume fraction after ageing $\varepsilon_{\mathrm{s,age}}$ and the lost solid phase volume fraction $\varepsilon_{\mathrm{loss}}$. Due to the loss of active material the SoC of the cell is affected. This has been accounted for by simulating one charge/discharge routine with the new amount of active material in order to set the initial values of the state variables at the shifted SoC 50.
Additionally to an increased SEI thickness and to the loss of a certain fraction of active material, ageing is assumed to affect the electrochemical reactions as well as the corresponding double layers. Reaction products can decrease the microporosity [132] and the loss of active material reduces the surface available for reaction. Surface film formation and further mechanical and chemical degradation of particles causes electrical isolation of particles [133] at anode and cathode, thereby influencing the active surface areas $a_{\mathrm{s,m}}$ [134] and therefore the reaction overpotentials. Due to this electrical isolation the charge transfer process is affected in any case while different scenarios are tested in order to find out if the corresponding double layer is affected as well. The priorly described ageing principle is illustrated in figure 5.2 for the isolations at the anode interfaces. Depicted is an example, where the double layer of the first interface is affected while the double layer of the second interface is unaffected by

the isolation. Within the SP model, the isolations are mathematically accounted for with isolations p_a, p_{IFA} and p_c, reducing the corresponding specific surface areas of the anode/SEI $a_{s,a,age}$, the IFA/electrolyte $a_{s,IFA,age}$ and the cathode/electrolyte interfaces:

$$a_{s,a,age} = a_{s,a} \cdot (1 - p_a), \tag{5.29}$$

$$a_{s,IFA,age} = a_{s,IFA} \cdot (1 - p_{IFA}) \tag{5.30}$$

$$a_{s,c,age} = a_{s,c} \cdot (1 - p_c) \tag{5.31}$$

The complete introduced ageing model includes several assumptions. Although, all of these assumptions are based on physical processes which have been reported for the ageing of Lithium-ion batteries in previous research, cross validation of the model to proof all assumptions is beyond the scope of this research. The focus of this work is set on a state estimation of one cell at different SoHs in order to show the applicability and the current limits of the model.

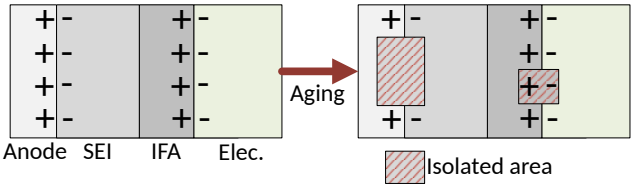

Figure 5.2: Schematic illustration of the ageing induced isolation exemplary shown at the two anode interfaces. The reaction is being blocked at both interfaces. At the inner interface charges are shifted by the isolation as well, which affects the related double layer.

5.3.4 Parameter Identification Algorithm

PI is conducted using a non-linear least square trust-region-reflective algorithm embedded in Matlab. The objective function $\chi^2(\omega, \vartheta)$, shown in equation 5.32, contains the relative error for the real part of the measurement and simulation for the investigated frequencies ω_i of the part of the spectrum which is fitted. Using the real part of the impedance for the objective function was found to lead to better results than using an

objective function combined of real and imaginary part or combined of phase and impedance. This is because of the use of a SP-model instead of a more discretised model. A SP-model calculates a defined deviation of the imaginary part of the impedance to the measured semicircles, since it calculates one perfect charge transfer process on each electrode, whereas e.g. a pseudo-two-dimensional (P2D) model or a model including a particle size distribution (PSD) simulate one charge transfer process for each modelled particle. If the charge transfer processes in such a model occur at different time constants, e.g. due to different local overpotentials for each particle, the resulting semicircle in the Nyquist plot will be flattened, while semicircles simulated on a SP model are always unmodified. It should be noted at this point that using a P2D model does not lead to a distribution of time constants similar to the actual one in the cell. This can be seen in the results presented by Tippmann et al. [66]. The usage of a model including a PSD would be a significant improvement but as long as the actual charge distribution within the cell is unknown the model includes an epistemic uncertainty. Since the described deviation is not physic-based but model-based, including the imaginary part or the phase of the impedance in the objective function will decrease the quality of the result. Thus, using the real part of the impedance avoids over-fitting, as the PI algorithm otherwise would try to fit a feature the model is not capable to simulate. Therefore, the function which the in Matlab implemented Trust Region Reflective Algorithm minimises is:

$$\chi(\omega, \vartheta) = \min \sum_{i}^{k} \left| \frac{Re_{\text{meas}}^{\omega_i} - Re_{\text{sim}}^{\omega_i}}{Re_{\text{meas}}^{\omega_i}} \right|^2 \tag{5.32}$$

ϑ represents the parameters to be identified and k the number of frequencies. Since the real part and imaginary part of the impedance are correlated by the Kramers-Kronig relations the results of the parameter identification still include an error due to the use of the single particle model.

5.4 Results and Discussion

This section starts by discussing EIS and capacity measurements. In the second part, the parameters of the unaged cell are identified and discussed. Afterwards, the ageing model is applied to investigate the change of the cell impedance during ageing. Finally, the ageing progress is discussed based on the evolution of ageing parameters during cycling. Matlab has been used to perform the simulations in time domain.

5.4.1 Measurement Results

In figure 5.3, the impedance spectra of the cycle-aged cell are shown in a Nyquist plot. At very high frequencies the system shows inductive behaviour which is induced by the wiring and not by the battery. Therefore, the inductive behaviour is not included in the model. The intersection of the measurement with the x-axis at high frequencies is magnified in the inset. The corresponding real part is assigned to the internal resistance of the cell and increases monotonously with increasing cycling number. In the frequency range from 0.3 Hz to 205 kHz, two semicircles are visible. The left and bigger one has a maximum imaginary part at 1.4 kHz and is attributed to the SEI, whereas the smaller one with a characteristic frequency of 7.2 Hz is attributed to the charge transfer reactions in anode and cathode [23]. During cyclic ageing the characteristic frequency of the SEI semicircle shifts from 1.4 kHz at the BoL to 1 kHz after 350 cycles while the characteristic frequency of the charge transfer reaction shifts from 7.2 Hz at the BoL to 2 Hz after 350 cycles. This indicates that both related processes decelerate due to the ageing of the cell. Next to the low frequency semicircle, in the low frequency range, the impedance rises linearly, as it is characteristic for semi-infinite diffusion processes. It is attributed to solid diffusion in the active material particles. Furthermore, with increasing cycle number, the spectra shift to higher real parts of the impedance due to an increase of the internal resistance of the cell. Moreover, the semicircle of the SEI as well as the semicircle of the charge

transfer reactions widen. The general trend of increasing impedances, visible in figure 5.3, which leads to a widening of the semicircles and to a right shift of the spectrum, has been reported in literature before [20].

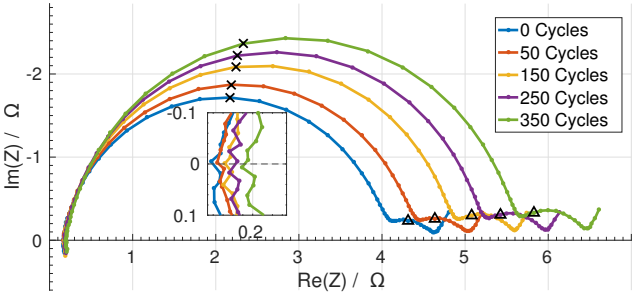

Figure 5.3: EIS measurements for a cycle-aged Lithium-ion battery at SoC 50%. × and △ indicate impedance points at 1.4 kHz and 7.2 Hz respectively.

In addition to the Nyquist plots in figure 5.3, the capacity fade and the impedance at the characteristic frequencies of the semicircles are displayed in figure 5.4. Within the first 350 cycles, the SoH decreases from 100 % to 83.33 %. During the last measured 50 cycles, the capacity decreases drastically by additional 73.5 %, indicating the EoL of the battery. The red graphs in figure 5.4 show the absolute values of the impedance at the characteristic frequencies of the two semicircles with increasing cycle number. Both impedances increase monotonously during the first 350 cycles due to the proceeding ageing of the cell. The increase at 7.2 Hz is more distinct because the impedance at lower frequencies includes the response of all faster processes whereas at high frequencies, the slower processes are not excited by the sinusoidal input. Therefore, at 7.2 Hz charge transfer and SEI influence is visible while at 1.4 kHz the impedance is only influenced by the internal resistance and the SEI. The measurement results further show, for example within the first 100 cycles, that the loss of capacity can not be correlated with the impedance of the cell. For the first 50 cycles almost no loss of capacity has been measured while the impedance of the cell rises. During the next 50 cycles the SoH decreases

more noticeable while the impedance rise is a bit lower.

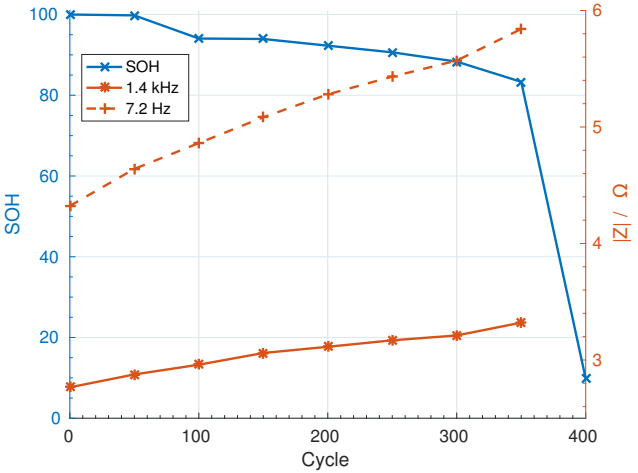

Figure 5.4: The State of Health (blue) and the impedances (red) at 7.2 Hz (dashed) and 1.4 kHz (solid) for the cycled battery

5.4.2 Identification of kinetic Parameters

In a next step, kinetic and transport parameters of the model are identified using the parameters presented in table 5.1 and the impedance measurement of the unaged cell. This step is performed prior to the analysis of the degradation in order to determine the unknown reaction rate constants k_{SEI}, k_{c} and k_{IFA} as well as the corresponding double layer capacitances C_a^{DL}, $C_{\mathrm{c}}^{\mathrm{DL}}$ and $C_{\mathrm{IFA}}^{\mathrm{DL}}$. Additionally, the thickness of the initial SEI $d_{\mathrm{SEI,init}}$ and the conductivity of the SEI σ_{SEI} are identified. The PI is performed sequentially in order to decrease the simulation time and to ensure uniqueness of the fit. For a detailed investigation of the limitation of parameter estimation from EIS data the reader is referred to the work of Alavi et al. [135]. Since parameters affect only a specific time constant of the spectrum, PI can be performed beginning from high frequencies to low frequencies without loss of accuracy. First, the volume of the initial SEI and the related thickness of the SEI are calculated with equations 5.25

and 5.26, giving a value of $d_{\mathrm{SEI,init}} = 184\,\mathrm{nm}$. The calculated value is higher than the reported values from Christensen [69] because the thickness is calculated from the Lithium being lost during the first cycles, while Christensen used reaction kinetics to determine the thickness. The result is strongly dependent on the assumption for the amount of Lithium being lost and on the material parameters of the SEI. In general, values for the thickness of the SEI reported in literature vary strongly which aggravates comparison. After determining the initial SEI thickness in a first step, the internal resistance of the cell is identified by adjusting the conductivity of the SEI σ_{SEI}. Afterwards, the high frequency semicircle is adjusted by identifying k_{IFA} and $C_{\mathrm{IFA}}^{\mathrm{DL}}$. The last step includes the identification of k_{SEI}, k_{c}, $C_{\mathrm{a}}^{\mathrm{DL}}$ and $C_{\mathrm{c}}^{\mathrm{DL}}$ with the impedance data from the low frequency semicircle. Since the coupled anode reactions are linked with the reaction at the interfacial area by the free surface sites on the IFA, the related time constant is lower than the time constant of the cathode reaction, which has also been reported by Illig et al. [136]. Using this information for the PI at the low frequency semicircle enables unambiguous results with four parameters. The resulting values for the identified parameters are given in table 5.2. At the anode side, double layer capacitances at both interfaces of the SEI differ by more than four orders of magnitude with the one at the electrolyte interface being significantly smaller. This discrepancy is reasonable since the related measured bigger semicircle has a much smaller time constant and is clearly separated from the low frequency semicircle. The double layer capacitance of the IFA is expectably much smaller than the anode double layer capacitance. In comparison to the capacity values found by Huang et al. [50] the value for the IFA in this work is very small while the identified value for the anode is higher than the one suggested by Huang et al. Additionally, the values presented in the works of Ong [114], Xie [20] and Tippmann [66] differ not only significantly to the ones presented in this chapter but also to the values which Huang suggested. Therefore, further research on reliable measurements of the double layer capacitance is needed. For the reaction rate constants at the anode and

interfacial area no comparison with literature values is possible since a novel approach to couple the SEI reactions according to equation 5.16 is used. The calculated cathode reaction rate constant is in agreement with the value presented by Colclasure et al. [70]. Experiment and the resulting

Parameter	IFA	SEI	Anode	Cathode
DL capacitance C^{DL} / $\frac{F}{m^2}$	$1.75 \cdot 10^{-3}$	-	17.89	1.70
Reac. rate const. k_f / $\frac{m^{2.5}}{mol^{0.5}s}$	1.85	$4.99 \cdot 10^{6}$	Table 5.1	$2.05 \cdot 10^{-10}$
SEI-Conductivity σ_{SEI} / $\frac{S}{m}$		$8.76 \cdot 10^{-5}$		

Table 5.2: Model parameters identified using the impedance spectrum measured on the unaged cell.

simulated EIS are shown in figure 5.5. The simulation matches the internal resistance well but is not able to meet the imaginary part at the peak of the high frequency semicircle as discussed in section 5.3.4. The Bode plots confirm this deviation and highlight that phase shift and impedance of the measurement are slightly shifted to higher frequencies in the range of the high frequency semicircle. Using the introduced model, the simulated high frequency semicircle includes only one time constant for the processes at the SEI/electrolyte interface. Therefore, the flattening of the high frequency semicircle can not be reproduced perfectly. The algorithm for the PI is able to reproduce the low frequency semicircle well, since the two characteristic frequencies for the two main charge transfer reactions at anode and cathode are in this frequency range. Another deviation is visible at the diffusion part of the impedance spectrum at low frequencies. Due to the low slope of the anode OCV-curve the anode does not show any diffusion impedance [136]. The remaining cathode diffusion impedance, simulated with a SP model, always increases with a 45 ° slope, while the measured impedance increases with a higher slope, since multiple diffusion processes with different time constants take place [137].

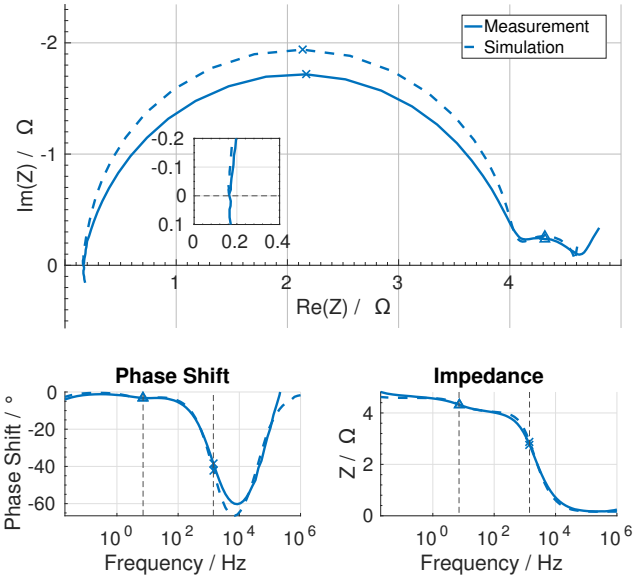

Figure 5.5: Experimental (solid line) and simulated (dashed line) EIS for an unaged Lithium-ion battery at SoC 50% and $T = 25\,^{\circ}\mathrm{C}$. × and △ indicate impedance points at 1.4 kHz and 7.2 Hz respectively.

5.4.3 Identification of ageing Parameters

The ageing process is analysed using the SP-SEI model via identifying changes in the loss of active material $\varepsilon_{\mathrm{loss}}$, the SEI-thickness d_{SEI}, the isolation of the SEI/electrolyte interface p_{IFA}, the isolation of the particle/SEI interface p_{a} and the isolation of the cathode surface p_{c} using the observed change in the impedance spectra. Starting from the parameters of the unaged cell, the PI algorithm is applied for every aged impedance spectrum sequentially by extracting the relevant ageing parameters from the capacity and the internal resistance, than from the high frequency semicircle and in the end from the low frequency semicircle. This routine is similar to the one introduced by Zavalis et al. [21]. The change of the capacity of the cell during ageing is simulated by a change of the available active material. Therefore, the solid phase volume fraction is

reduced following equation 5.27. It is assumed that the loss of active material takes place at both electrodes and that the lost active material is fully lithiated, because the mechanical stress within the particles is at a maximum if the maximum possible amount of lithium is intercalated. Then the thickness of the SEI is adjusted to reproduce the experimentally observed change of the internal resistance. Afterwards the isolation at the SEI/electrolyte interface is identified using the high frequency semicircle. Since the time constant of the high frequency semicircle increases during ageing, better agreement with the experiment is achieved when assuming that the related double layer of the SEI/electrolyte interface is unaffected by the isolation. This assumption is physically based on the idea that the absolute value of the double layer might change but not the area weighted value which has been used for the simulations [21]. The resulting increase of the time constant of the high frequency semicircle shifts the time constant of the low frequency semicircle as well, because the related reactions are coupled. For the low frequency semicircle which is characterised by the charge transfer at anode and cathode, several degradation options were evaluated regarding their ability to reproduce the changes in EIS. In order to determine the physically most reasonable option for the ageing model all possible options are simulated and the results of the PI algorithm are evaluated. The options differ in the interfaces which are isolated and whether the related double layer capacitance is affected by the isolation, using the equations 5.29-5.31, or not. table 5.3 shows the normalized residuum of the objective function and the resulting isolations for all twelve model options extracted from the low frequency semicircle after 350 cycles.

affected double-layer capacitance	isolated interfaces: both electrodes	anode only	cathode only
both electrodes	$\mathbf{3.52 \cdot 10^{-4}}$ **0 / 57.39**	$2.5 \cdot 10^{-3}$ 21.31 / fixed 0	$3.52 \cdot 10^{-4}$ fixed 0 / 57.39
anode only	$1.2 \cdot 10^{-3}$ 16.49 / 50.16	$2.5 \cdot 10^{-3}$ 21.31 / fixed 0	$3.8 \cdot 10^{-3}$ fixed 0 / 60.52
cathode only	$\mathbf{3.52 \cdot 10^{-4}}$ **0 / 57.39**	$1.1 \cdot 10^{-3}$ 34.58 / fixed 0	$\mathbf{3.52 \cdot 10^{-4}}$ **fixed 0 / 57.39**
both DL unaffected	$4.61 \cdot 10^{-4}$ 28.31 / 43.4	$1.1 \cdot 10^{-3}$ 34.58 / fixed 0	$3.8 \cdot 10^{-3}$ fixed 0 / 60.52

Table 5.3: Impact of the model options on the parameter identification at the low frequency semicircle after 350 cycles. The first value in each cell is the normalized residuum of the objective function. Second and third values show the calculated isolations in percent for anode and cathode, respectively.

With table 5.3 three options in bold can be identified to produce the best possible agreement with the experimental data. All three options have zero anode isolation. For the first two of these options, both interfaces are affected by isolations. In the last option, the PI algorithm can only adjust the cathode isolation. The second best result was achieved with an isolation on both interfaces which do not affect the related double layer capacitances leading to isolations of 28 % and 43 % for anode and cathode respectively. Since the PI algorithm leads to optimal results for zero anode isolation and to good results with significantly higher cathode isolation, the algorithm clearly suggests, that mainly or only cathode isolation took place as previously shown by Abraham et al. [22, 102]. The low frequency semicircle changes are thus mainly attributed to an isolation at the cathode. Since the high frequency semicircle is changing its size due to an isolation at the SEI/electrolyte interface as discussed previously, the results point out that the change of the high and low frequency semicircles can be referred to degradation at the anode and cathode respectively. Furthermore, the high frequency semicircle is influenced by degradation at the SEI/electrolyte interface, while the low frequency semicircle is affected by degradation at the cathode/electrolyte interface. As such the model-

based analysis suggest that the two interfaces facing the electrolyte are being isolated during ageing and thus affecting the impedance spectrum, while the electrode/SEI interface has a negligible impact.

Using the above described sequentially applied parameter identification with the chosen model options leads to the results presented in figure 5.6. It shows that the applied ageing model can reproduce the experimentally observed ageing effects on EIS. The simulation results for the Nyquist and Bode plots, displayed as dotted lines, are in a good agreement with the solid lines representing the measurement results. The widening of the two semicircle, as well as the increase of the internal resistance, is indeed reproduced very accurately. However, for the low frequency semicircle, it can be seen that reproduction of the experiment by the model decreases with increasing cycle number, while the differences of the impedance between measurement and simulation at the high frequency semicircle are not higher than for the previous cycles. Considering the fact that the SoH of the cell decreases drastically from 350 cycles to 400 cycles, as presented in figure 5.4, it is assumed that an additional ageing process, e.g. a loss of electrical connectivity between the current collector and the active material, occurs. As the model can not reproduce the effect of this process on the impedance of the system, it seems that the occurring ageing process is not included in the model. Since this process only occurs close to the EoL of the cell at 400 cycles, it may well be responsible for the EoL. In this case, the discrepancy between model and experiment may indeed be a good indication for the nearing EoL. As the change of the low frequency semicircle has been assigned to degradation processes in the cathode, the results in figure 5.6 indicate that the additional ageing process rather affects the cathode than the anode. In conclusion, the occurrence of an undefined, not included ageing phenomenon seems to be detectable with the model and it may allow to predict the EoL.

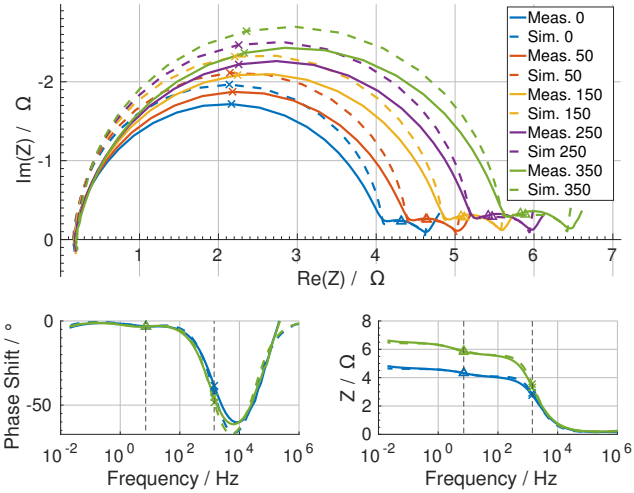

Figure 5.6: Measured and simulated EIS for the cycling aged Lithium-ion battery at SoC 50% and $T = 25\,^{\circ}\mathrm{C}$. × and △ indicate impedance points at 1.4 kHz and 7.2 Hz respectively.

As the reproduction of the ageing effects on EIS was successful, this allows to interpret the progression of the underlying ageing parameters with respect to the cycle number herein given in figure 5.7. All ageing parameters increase during the cyclic ageing except for the particle/SEI isolation which is zero at all cycles as discussed previously. The increase of the SEI thickness of approximately 50 nm is in agreement with several research results [138, 69, 139, 140]. Due to equation 5.24 which is used to calculate the potential distribution across the SEI, the increasing SEI-thickness accounts for the rise of the internal resistance of the cell during ageing. It should be noted, that the introduced ageing model can overestimate the thickness of the SEI if an increase of the internal resistance is not solely caused by the SEI which is likely to occur at the EoL of the cell. By extending the model with more ageing processes which influence the internal resistance as well, the thickness of the SEI could be determined more precisely. However, a separation of different ohmic loss contributions to the internal resistance is barely possible. Within this research, a

model extension, e.g. with a ageing-dependent electrolyte resistance, has not been implemented and the determined values for the SEI-thickness are therefore affected by an epistemic uncertainty. The surface isolation of the SEI/electrolyte interface as well as the thickness of the SEI show a constant increase within the overall cycle range. This monotonous increase occurs in agreement with the capacity loss, the increase of the internal resistance and the monotonously increase of the impedance, shown in figure 5.4, during cycling. For the cathode a high degree of isolated area is identified. Analysing the low frequency semicircle shows, that the diameter increases by approximately 57 % during the first 350 cycles. Since EIS is a linear method, a cathode isolation of 57 % after 350 cycles is therefore consistent if the isolation is the only degradation process, which affects the diameter. In contrast, to adjust the high frequency semicircle, a lower degree of isolated surface area, approximately 20 %, is needed. The high frequency semicircle is bigger than the low frequency semicircle, but its percental change during ageing is lower. To the best knowledge, no values for the surface isolations of the interfaces have been published yet, but observing a higher impact of the cathode degradation on the impedance spectrum is in agreement with the results presented by Heins et al. [141] and the reported sensitivity of the cathode to internal resistance changes [124]. Further analysis of the cathode surface isolation shows an unexpected high value at 100 cycles. The low frequency semicircle for 100 cycles has a larger diameter than the upcoming ones which can neither be seen in the Nyquist diagram nor in the analysis in figure 5.4 but is revealed by the resulting ageing parameters. This result is accounted to a temporary decrease of the ambient temperature during this measurement which increases the impedance of the low frequency semicircle. As reported by Heins et al. [142], the temperature affects the charge transfer semicircle more than the SEI semicircle which could explain why the cathode isolation shows unexpected high values for 100 cycles, while the SEI/electrolyte isolation is unaffected. The last curve shows the loss of active material during cycling following equation 5.27.

The loss corresponds to the loss of capacity shown in figure 5.4. After 350 cycles, approximately 13 % of the anode and cathode active material is assumed to be lost in order to adjust the simulated capacity to the measured value. The percental loss of active material after 350 cycles (13.27 %) is not in complete agreement with the measured percentage loss of the SoH (16.67 %) of the cell until this cycle, because it is assumed to loose active material at both anode and cathode, while the loss of the limiting electrode has a higher impact on the capacity change. Nevertheless, even if the loss of active material at the two electrodes does not have an equal impact on the capacity and impedance of the cell, it is reported to occur on the anode due to SEI isolations [143, 144, 145] and on both electrodes due to particle cracking and loss of connectivity between active material and current collector [146, 131]. In conclusion, the values for the identified ageing parameters might not be completely exact, because the newly introduced ageing model has not been validated yet and might not include all relevant ageing processes, but it could be shown, that the chosen set of ageing parameters is not only sufficient to reproduce the measured change in the impedance spectrum but is also in the right order of magnitude and can be reasonably well correlated to physical processes.

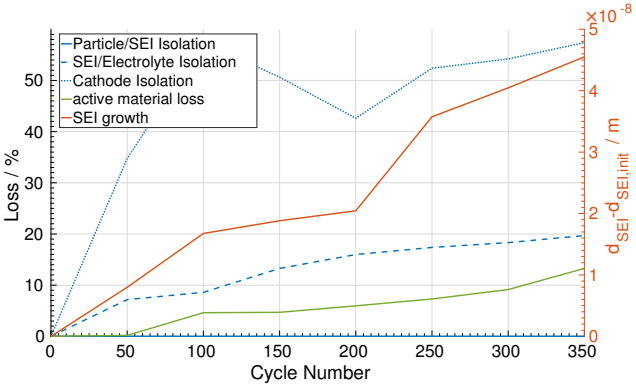

Figure 5.7: Ageing parameters of the simulated EIS for a cycled Lithium-ion battery

5.5 Conclusions

A physico-chemical single particle battery model has been extended with a new ageing model including a SEI in order to analyse the ageing state of Lithium-ion batteries. Impedance and capacity measurements during cyclic ageing of a NMC/graphite pouch full cell are performed to parameterise the model. Afterwards, parameter identification was conducted on different versions of the introduced ageing model. The study has shown that the model version which assumes SEI growth besides an isolation of the cathode surface is suitable to reproduce the experimentally observed changes in the impedance spectrum as well as the change of the capacity of the cell during ageing. The changes of the high and low frequency semicircles could be attributed to anode and cathode degradation, respectively and the two interfaces facing the electrolyte have been identified to be the decisive factors to reproduce the ageing effects on the impedance spectrum, while the anode/SEI interface has a negligible affect. Furthermore, decreasing quality of the reproduction of the low frequency semicircle close to the end of life indicates additional ageing phenomena not covered by the model. These findings may also be used to predict the EoL of Lithium-ion cells. Although, state estimation for the analysed cell using the introduced ageing model has been successful, model validation with different cells and different cycling conditions has to be done to validate the model assumptions. For future research it is suggested to extend the model by P2D characteristics, with a particle size distribution to enable more precise parameter identification by using the impedance instead of the real part of the impedance in the objective function. Cross validation as described and extension of the model with more degradation processes will show if the current model overestimates the values for the SEI thickness and the isolations.

6 Parameter Uncertainty Effects[1]

In the previous chapter, a parameter identification algorithm has been used to determine the values of kinetic, transport and ageing parameters. As described in section 3.3, the differences between the measured impedance and the simulated impedance might be caused by the uncertainty of the measurement device. Depending on the likeliness that the differences are caused by the uncertainty of the measurement device, a uncertainty of the identified parameters, quantified by their variance, can be calculated. To evaluate these variances and the correlation between all identified parameters the Fisher Information Metric, as introduced in section 2.5, has been calculated. Evaluation of the results of parameter identification algorithms applied to LiB models using the FIM is a well established practice for pyhsico-chemical models [75, 76, 77, 78, 79, 80, 81] and for ECMs [82, 83]. The FIM is not only used to quantify variances and covariances of identified parameters but also to maximise their identifiability by varying the model input [79, 78]. This work focusses on the evaluation and interpretation of the variances and covariances because the model input signals are fixed for EIS. In section 6.1 the FIM and the related covariance matrix are calculated for the kinetic- and transport parameters determined in section 5.4.2. Afterwards, the procedure has been applied again on the ageing parameters determined in section 5.4.3.

6.1 Kinetic- and Transport Parameters

The parameter vector for the kinetic and transport parameters is defined as $\vec{\theta} = [k_{f,c}, k_{f,SEI}, k_{f,IFA}, C_a^{DL}, C_{IFA}^{DL}, C_c^{DL}, \sigma_{SEI}]$. All 67 frequencies are evaluated with the simulated real and imaginary parts of the impedance to calculate the Fisher Information Metric as introduced in equation 2.30,

[1] The initial Matlab implementation for the calculation of the FIM has been developed by Shenliang Xu as part of his master thesis "Untersuchung der Sensitivität elektrochemischer Impedanzspektren mittels Monte-Carlo-Simulationen" at the TU Braunschweig.

which leads to the following FIM:

$$\mathbf{F} = \frac{1}{\sigma_{Re}^2} \begin{pmatrix} \sum_{i=1}^{67} \left(\frac{\partial Z_{Re}(f_i)}{\partial \theta_1}\right)^2 & \sum_{i=1}^{67} \frac{\partial Z_{Re}(f_i)}{\partial \theta_1} \frac{\partial Z_{Re}(f_i)}{\partial \theta_2} & \cdots & \sum_{i=1}^{67} \frac{\partial Z_{Re}(f_i)}{\partial \theta_1} \frac{\partial Z_{Re}(f_i)}{\partial \theta_7} \\ \sum_{i=1}^{67} \frac{\partial Z_{Re}(f_i)}{\partial \theta_2} \frac{\partial Z_{Re}(f_i)}{\partial \theta_1} & \sum_{i=1}^{67} \left(\frac{\partial Z_{Re}(f_i)}{\partial \theta_2}\right)^2 & \cdots & \sum_{i=1}^{67} \frac{\partial Z_{Re}(f_i)}{\partial \theta_2} \frac{\partial Z_{Re}(f_i)}{\partial \theta_7} \\ \vdots & \vdots & \ddots & \vdots \\ \sum_{i=1}^{67} \frac{\partial Z_{Re}(f_i)}{\partial \theta_7} \frac{\partial Z_{Re}(f_i)}{\partial \theta_1} & \sum_{i=1}^{67} \frac{\partial Z_{Re}(f_i)}{\partial \theta_7} \frac{\partial Z_{Re}(f_i)}{\partial \theta_2} & \cdots & \sum_{i=1}^{67} \left(\frac{\partial Z_{Re}(f_i)}{\partial \theta_7}\right)^2 \end{pmatrix} + \frac{1}{\sigma_{Im}^2} \begin{pmatrix} \sum_{i=1}^{67} \left(\frac{\partial Z_{Im}(f_i)}{\partial \theta_1}\right)^2 & \sum_{i=1}^{67} \frac{\partial Z_{Im}(f_i)}{\partial \theta_1} \frac{\partial Z_{Im}(f_i)}{\partial \theta_2} & \cdots & \sum_{i=1}^{67} \frac{\partial Z_{Im}(f_i)}{\partial \theta_1} \frac{\partial Z_{Im}(f_i)}{\partial \theta_7} \\ \sum_{i=1}^{67} \frac{\partial Z_{Im}(f_i)}{\partial \theta_2} \frac{\partial Z_{Im}(f_i)}{\partial \theta_1} & \sum_{i=1}^{67} \left(\frac{\partial Z_{Im}(f_i)}{\partial \theta_2}\right)^2 & \cdots & \sum_{i=1}^{67} \frac{\partial Z_{Im}(f_i)}{\partial \theta_2} \frac{\partial Z_{Im}(f_i)}{\partial \theta_7} \\ \vdots & \vdots & \ddots & \vdots \\ \sum_{i=1}^{67} \frac{\partial Z_{Im}(f_i)}{\partial \theta_7} \frac{\partial Z_{Im}(f_i)}{\partial \theta_1} & \sum_{i=1}^{67} \frac{\partial Z_{Im}(f_i)}{\partial \theta_7} \frac{\partial Z_{Im}(f_i)}{\partial \theta_2} & \cdots & \sum_{i=1}^{67} \left(\frac{\partial Z_{Im}(f_i)}{\partial \theta_7}\right)^2 \end{pmatrix} \tag{6.1}$$

θ_i is the element of the parameter vector $\vec{\theta}$ at the respective position and σ_{Re} and σ_{Im} are the standard deviations of the real and imaginary part of the impedance. $\sigma_{Re} = 0.0015\ \Omega$ and $\sigma_{Im} = 0.0055\ \Omega$ can be calculated from the values for the noise of the measurement sensor in accordance to [147, 148]. The resulting FIM given with equation 6.1 is calculated with Matlab using the script provided in appendix 11.3. As a first result it can be stated that the FIM for the kinetic and transport parameters can be inverted which means that all seven parameters can be identified. Using equation 2.32, the inverse of the FIM is calculated. The resulting covariance matrix of the parameters showing all correlations between the identified parameters and the variance of the parameters σ^2 on the diagonal of the matrix. The variance can be used to calculated the standard deviation which is the square root of the variance.

6.1.1 Standard Deviation and Relative Error

As introduced in section 2.5, the relative error according to equation 2.33 is calculated using the standard deviation. Table 6.1 shows the standard

deviation and the relative error for all identified parameters.

Parameter	identified value	σ	relative error
$k_{f,\mathrm{c}}$	2.05×10^{-10}	3.63×10^{-12}	5.32%
$k_{f,\mathrm{SEI}}$	4.99×10^{6}	1.10×10^{4}	0.66%
$k_{f,\mathrm{IFA}}$	1.85	8.82×10^{-4}	0.14%
$C_{\mathrm{a}}^{\mathrm{DL}}$	17.89	0.60	10.11%
$C_{\mathrm{IFA}}^{\mathrm{DL}}$	1.75×10^{-3}	5.50×10^{-7}	0.094%
$C_{\mathrm{c}}^{\mathrm{DL}}$	1.7	0.040	7.03%
σ_{SEI}	8.76×10^{-5}	2.05×10^{-7}	0.70%

Table 6.1: Absolute value, variance and relative error of the identified kinetic and transport parameters

The values in table 6.1 clarify that the relative errors of the seven parameters do not exceed 10.11%, even with a 3σ-confidence interval. Furthermore, the parameters can be divided into two groups with respect to their relative error made at the parameter identification in chapter 5. The relative errors for $k_{f,c}$, C_a^{DL} and C_c^{DL} are significantly larger than the remaining relative errors. The probability densities can be illustrated if the calculated standard deviations are used to describe each identified parameter as a standard normally distributed random variable with the identified values as the estimated values. In figures 6.1 these probability density functions are displayed for $k_{f,c}$, C_a^{DL} and C_c^{DL} along with their 3σ-confidence intervals denoted with dotted vertical lines. In order to be able to compare the parameter uncertainties the estimated values are scaled to one. This form of presentation highlights the difference between the parameters with high relative error and the parameters with low relative error because the integral over the whole range of a parameter value is equal for each probability density function. Therefore, higher maximum values for the probability density in figure 6.2 compared to the values in figure 6.1 correlate with narrower curves and smaller relative errors.

For the parameters $k_{f,c}$, C_a^{DL} and C_c^{DL}, shown in figure 6.1, the confi-

dence intervals are wide due to their high relative error. This result is reasonable, because all those three parameters affect the low frequency semicircle in the Nyquist diagram. For the impedance of the analysed cell the low frequency semicircle is smaller than the high frequency semicircle. Assuming equal relative sensitivity of both semicircles to changes of the corresponding parameters the absolute impedance change of the bigger semicircle would be larger than for the smaller semicircle. Therefore, parameters affecting the smaller semicircle are tendentially harder to identify. In addition, the low frequency semicircle is affected by more parameters than the high frequency semicircle which makes their identifiability more difficult.

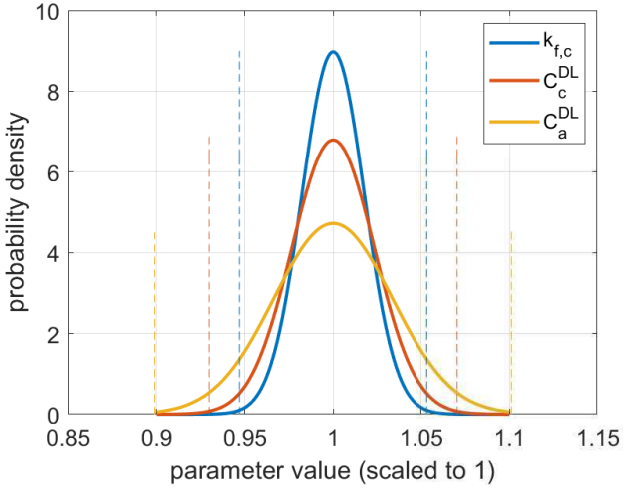

Figure 6.1: Probability density functions of the transport and kinetic parameters with high relative error $k_{f,c}$, C_c^{DL} and C_a^{DL}

The conductivity and the reaction rate constant of the SEI have to be discusses separately. A change of the conductivity of the SEI has no impact on the imaginary part of the impedance, but it shifts all frequency points on the real part axis. Since the relative error is calculated with the sen-

sitivity of both, the real- and the imaginary part of the impedance, its value is of medium size as can be seen in table 6.1 and in the corresponding probability density function in figure 6.2. The reaction rate constant $k_{f,SEI}$ is also unique in its affect on the simulated impedance spectrum. Since the corresponding reaction is coupled with the anode reaction the effect of a change of $k_{f,SEI}$ can not be assigned directly to the high or low frequency semicircle but the probability density function in figure 6.2 shows that the $k_{f,SEI}$ can be identified with a similar precision than σ_{SEI}. The remaining parameters shown in figure 6.2 $k_{f,IFA}$ and C_{IFA}^{DL} have the smallest relative errors and therefore the smallest confidence intervals. These parameters are the only ones of the seven parameters which affect the size and shape of the high frequency semicircle in the Nyquist diagram. Since a smaller amount of parameters lead to a better identifiability of them, the resulting relative errors are very small and the correlating probability functions very narrow.

For transport and kinetic parameters a maximum relative error of 10.11% with a 3σ-confidence interval is acceptable for this research since the focus is set to the ageing studies in order to correlate the change of ageing parameters to the SoH of the cell and not to a maximum precise determination of kinetic and transport parameters.

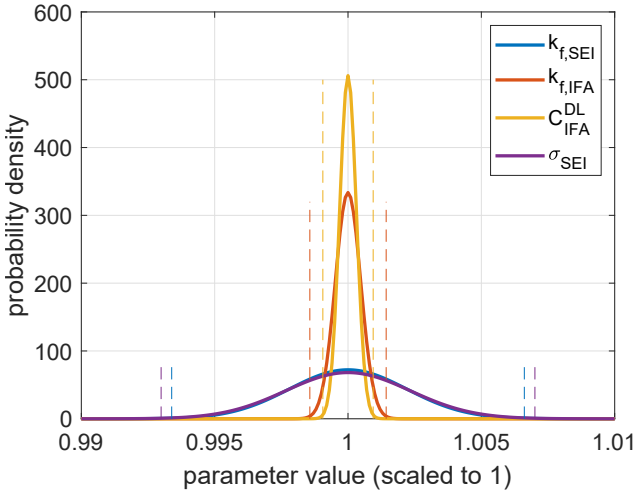

Figure 6.2: Probability density functions of the transport and kinetic parameters with low relative error $k_{f,\mathrm{SEI}}$, $k_{f,\mathrm{IFA}}$, $C_{\mathrm{IFA}}^{\mathrm{DL}}$ and σ_{SEI}

6.1.2 Covariance of transport and kinetic Parameters

The covariance matrix can be used to calculate correlation coefficients via equation 2.34. These values for the correlation coefficients give information about the correlation between the parameters as does the covariance matrix. The advantage of the correlation coefficients is that the values are scaled to values between -1 and 1. All correlation coefficients are listed in table 6.2.

The first result is that all reaction rate constants are positively correlated to each other which is plausible since they all affect the diameter of one of the two semicircles. The values increase for correlations between reaction rate constants with higher impact on the spectrum and for reaction rate constants affecting the bigger high frequency semicircle rather than the smaller low frequency semicircle.

Secondly, the conductivity of the SEI σ_{SEI} is positively correlated to the reaction rate constants and negatively correlated to the double layer ca-

pacitances. This is also plausible since an increase of σ_{SEI} shifts the whole spectrum to lower real parts of the impedance. An increase of the reaction rate constants also shifts frequency points to lower real parts but not for the whole spectrum.

Increasing the double layer capacitances decelerate the corresponding processes while increasing the reaction rate constants accelerates the corresponding processes. Therefore, reaction rate constants and double layer capacitances tend to be correlated negatively. This effect can be mitigated by the overlaying effect that an increase of the double layer capacitance can shift frequency points of the spectrum to lower real parts which also occurs for increasing reaction rate constants as mentioned before.

It is noticeable that the correlation coefficients of the double layer capacitance of the anode C_a^{DL} are high, especially the ones for the correlation to the reaction rate constants. Since these values are not physically explainable is must be assumed that the high relative error of C_a^{DL} and the corresponding low impact of the parameter on the impedance spectrum causes non interpretable values for the correlation coefficient.

The analysis of the correlation coefficients shows that most values can be explained physically and quantify the correlation of the parameters. Due to the fact that double layer capacitances do not affect the impedance spectrum straight forward as reaction rate constants and conductivities, their correlation to other parameters is harder to interpret and the resulting values have to be used carefully.

	$k_{f,\mathrm{c}}$	$k_{f,\mathrm{SEI}}$	$k_{f,\mathrm{IFA}}$	$C_{\mathrm{a}}^{\mathrm{DL}}$	$C_{\mathrm{IFA}}^{\mathrm{DL}}$	$C_{\mathrm{c}}^{\mathrm{DL}}$	σ_{SEI}
$k_{f,\mathrm{c}}$	1	0.25	0.67	-0.85	-0.13	0.24	0.20
$k_{f,\mathrm{SEI}}$	0.25	1	0.48	-0.57	-0.11	0.24	0.14
$k_{f,\mathrm{IFA}}$	0.67	0.48	1	-0.93	-0.29	-0.23	0.18
$C_{\mathrm{a}}^{\mathrm{DL}}$	-0.85	-0.57	-0.93	1	0.26	-0.05	-0.29
$C_{\mathrm{IFA}}^{\mathrm{DL}}$	-0.13	-0.11	-0.29	0.26	1	0.19	-0.42
$C_{\mathrm{c}}^{\mathrm{DL}}$	0.24	0.24	-0.23	-0.05	0.19	1	-0.10
σ_{SEI}	0.20	0.14	0.18	-0.29	-0.42	-0.10	1

Table 6.2: Correlation coefficients for transport- and kinetic parameters

6.2 Application to Ageing Parameters

In this section the method applied in section 6.1 is used again but this time to ageing parameters. All ageing parameters except for the loss of active material $\varepsilon_{\text{loss}}$ are combined in the parameter vector $\vec{\theta} = [d_{\text{SEI}}, p_{\text{IFA}}, p_{\text{c}}]$. The loss of active material is left out because it affects the capacity and not the impedance of the cell in the used model. The remaining ageing parameters change with the amount of cycles the battery cell has run for. Exemplary, in this section the ageing parameters after 350 cycles are analysed. First of all the numerical form of the Fisher-Information Metric is set up. Since three parameters are to be analysed at this point a 3×3 instead of a 7×7-Matrix as in the previous section is calculated. The resulting Fisher-Informations Metric proofs to be invertible which means that all three ageing parameters are identifiable. Analogous to the approach in section 6.1 the covariance matrix is calculated with the inverse of the Fischer-Information Metric. The values on the diagonal quantify the variance of σ^2 of the ageing parameters.

6.2.1 Standard Deviation and Relative Error

Table 6.3 lists the identified parameters along with the resulting values for the standard deviation and the relative error after 350 cycles. The calculations have been performed equivalent to the ones in the previous section.

parameter	identified value	σ	relative error
d_{SEI}	2.24×10^{-7}	4.37×10^{-10}	0.59%
p_{IFA}	19.92%	7.34×10^{-5}	0.11%
p_{c}	56.23%	1.23×10^{-3}	0.66%

Table 6.3: Standard deviation and relative error of the ageing parameters after 350 cycles

For the ageing parameters of the battery model after 350 cycles the standard deviations and the relative errors for each ageing parameter are distinctly blow 1%. This means that the applied parameter identification

algorithm calculates reliable values for the ageing parameters. This is caused by the fact that each ageing parameter has a unique and significant effect on the impedance spectrum which enables a very precise parameter identification. It has to be noted that during ageing more than three parameters change. In this work the kinetic- and transport parameters are assumed to stay constant during cycling. Instead, the effects of ageing on the impedance spectrum are condensed to the change of the three introduced ageing parameters. The resulting low relative errors show that describing the ageing processes with fewer parameters leads to a better identifiability of these parameters. Therefore, for the desired correlation between the change of ageing parameters with the SoH of a cell, the reduction of the amount of ageing parameters for a better identifiability is suitable as long as all physical processes affecting the impedance and the SoH are still considered. This has been shown in the previous chapter where the EOL of the analysed cell has been predicted with the introduced ageing model including only introduced ageing parameters.

6.3 Concluding remarks

Within the previous sections of this chapter an algorithm to calculate the FIM has been used in order to quantify the identifiability of model parameters of a LiB model with EIS. In section 6.1 the results of the FIM show that the issue of limited identifiability applies for example for the double layer capacitance of the anode which can only be identified with an uncertainty of 10%. Since all calculated uncertainties are minimum values which only include the uncertainty of the measurement device, these parameters can only be used under specific conditions. The poor identifiability can be accepted if the identified values are used for impedance simulations exceptionally because even an uncertainty of 10% of these parameters does not affect the resulting impedance spectrum significantly. Still, the identified set of parameters should be checked on its impact on discharge simulations before used for such simulations. It has to be

noted, that kinetic and transport parameter, especially double layer capacitances, have only small effects on discharge curves since the capacity of the cell is dominantly affected by the amount and type of active material.

In section 6.2, the results show that the all ageing parameters, identified in section 5.4.3, can be determined with a relative error of less than 1%. Comparing the identifiability of kinetic and transport parameters with the identifiability of ageing parameters shows that precise identifiability of model parameters using impedance data is facilitated by two conditions. First, the amount of parameters being identified at once with one impedance spectrum should be as low as possible. Second, parameter with strong and unique impact on the impedance spectrum can be identified more precisely.

Summarising, the results of the FIM have clarified that a set of three ageing parameters can be identified very precisely using EIS but the results should only be used for correlating the values of the ageing parameters to the current SoH of a cell.

7 Summary and Conclusion

The main reason for research on the presented topics is the need for a fast and precise method to determine the **S**tate **o**f **H**ealth of a **L**ithium-**i**on **B**attery. **E**lectrochemical **I**mpedance **S**pectroscopy is chosen as the measurement technique, because it is relatively fast and easy to apply. In order to be able to interpret results of EIS measurements physical insight into the LiB is needed which can be achieved by using a physico-chemical LiB model and by simulating EIS with this model. If model results and experimental results can be brought into agreement the chosen parameters for the battery model give insight to the actual SoH of the cell. The presented work has shown that impedance measurements can be simulated with a physico-chemical model and identified model parameters can correlated to the SoH. In addition, methods to overcome the challenges such as the overlapping of anode and cathode impedance contributions at similar frequencies or the general identifiability of model parameters are presented.

Chapter 3 focusses on these challenges and outlines how information about the slope of the OCV curves of anode and cathode can be used to relate diffusive impedance contributions to the respective electrodes. Subsequently, in chapter 4 it is outlined how a temperature distribution applied to single-layered cells can be used to assign anode and cathode charge transfer impedance contributions. For the analysed cells the charge transfer reaction and double layer charging and discharging occurs at a lower time constant at the cathode than at the anode.

Such an assignment is used in the main part of the thesis in order to be able to identify ageing parameters and their relation to the SoH of a LiB. In chapter 5 a detailed ageing model is introduced and a parameter identification algorithm is applied to determine the change of ageing parameters during cyclic ageing. The successful application of the ageing model shows that the assumed physics at the anode, including a SEI and

an adsorption layer with an additional double layer, is suitable to simulate the ageing of a LiB. The resulting values for the thickness of the SEI, the loss of active material and the isolations of the reaction surfaces have successfully been related to the SoH indicating that the increase of cell impedance is caused by a loss of surface area while the loss of capacity is caused by a loss of active material at the anode and cathode. The identified change of the ageing parameters give insight into the processes and even enabling a possible prediction of the EOL of the analysed cell.

Results presented in the last chapter 6 evaluate the accuracy of the identified parameters showing that some kinetic parameters e.g. the double layer capacitance of the anode can not be determined with a relative error of less than 10% while the identification of the ageing parameters is very precise with a relative error of $\approx$ 1% for all ageing parameters. Therefore, the amount of parameters to be identified simultaneously using EIS should be as low as possible. Poor identifiability indicates a low impact of the related parameter to the impedance spectrum.

Summarising, this thesis does not only show that the change of impedance spectra of LiBs during ageing can be modelled with a physico-chemical battery model but also focusses on the challenges which apply when using this approach. Various options to separate the different anode and cathode impedance contributions to the full cell spectrum are outlined and the identifiability of the model parameters have been shown including a calculated value for the standard deviation of each identified parameter.

In future, the new ageing model, which extends the basic Doyle-Newman model, should be extended to a pseudo two dimensional model with a particle size distribution in order to be able to reproduce the actual distribution of time constants of the processes in the cell. For the new presented measurement setup and routine applicability to various cell formats must be analysed. In addition, the possibility to use the found assignments of the electrodes should be checked on cells of similar cell chemistry in future research. The mathematical analysis using the FIM should be further

substantiated with discharge simulations and by applying similar methods like kinetic Monte Carlo simulations.

8 List of Abbreviations

BMS - Battery Management System

BoL - Beginning of Life

DMC - DiMethyl Carbonate

EC - Ethylene Carbonate

ECM - Equivalent Circuit Model

EIS - Electrochemical Impedance Spectroscopy

EoL - End of Life

EV - Electric Vehicle

FIM - Fisher Information Metric

LiB - Lithium-ion Battery

LTO - Lithium Titanate

NMC - Nickel Manganese Cobald

OCV - Open Circuit Voltage

PI - Parameter Identification

SEI - Solid Electrolyte Interphase

SISO - Single-Input Single-Output

SoC - State of Charge

SoH - State of Health

9 List of Symbols

a	activity coefficient, mol m^{-3}
a_s	specific surface area, m^{-1}
A	area, m^2
B	Redlich-Kister parameter, J mol^{-1}
c	concentration, mol m^{-3}
C_{DL}	double layer capacitance, C $m-2$
d	thickness, m
D	diffusion coefficient, m^2 s^{-1}
D^{mig}	transport coefficient, C mol m^{-3} kg^{-1}
E_0	standard potential, V
f	frequency, s^-1
F	Faraday constant, C mol^{-1}
$\mathbf{F}$	Fisher Information Metric
g	insertion rate, -
i	current, A
Im	imaginary part of complex impedance, Ω
j	current density, A m^{-3}
j_0	exchange current density, A m^{-2}
J	charge flux, A m^{-2}
k	reaction rate constant, m^4 mol^{-1} s^{-1}
L	thickness of cell, m
$L()$	Likelihood function
M	molar mass, kg mol^{-1}
n	amount of substance, mol
N	number of analysed frequencies, -
p	isolation, -
r	reaction rate, A m^{-3}
R	real gas constant, J mol^{-1} K^{-1}

R	radius, m
Re	real part of complex impedance, Ω
t	time, s
t_p	transference number, -
T	temperature, K
$u()$	input signal
V	amount of vacancy sites, -
x	spacial coordinate, m
$\vec{x}$	state variable
Z	complex impedance
y	Lithium insertion rate, -
$y()$	model output signal
$\hat{y}$	measurement output signal
z	valence of ions, -
α	reaction symmetry factor, -
β	reaction symmetry factor, -
β	Bruggeman's exponent, -
γ	activity coefficient, -
δ	width , m
Δ	difference, -
ε	volume fraction, -
$\varepsilon()$	model error
η	reaction overpotential , V
θ	parameter vector
Θ	amount of surface sites, -
λ	reaction coefficient, A mol^{-1}
μ	expected value
ρ	density, kg $\mathrm{m}^{-}3$
σ	conductivity, S m^{-1}
σ	standard deviation
τ	time constant, s
φ	phase angle, $^\circ$

Φ	electrical potential, V
$\chi()$	objective function for the PI
ω	angular frequency, $s^{-}1$

10 Superscripts and Subscripts

0	particle surface
0	initial value
1	inner SEI
2	outer SEI
a	anode
Ads	adsorption layer
age	aged cell
b	backwards
c	cathode
ct	charge transfer
cap	capacitance
cell	cell
CorM	corrected Measurement
DL	double layer
e	electrolyte phase
f	forward
if	SEI/Electrolyte interface
IFA	interfacial area
Li	Lithium
Li^+	cation
Li_2CO_3	Lithium carbonate
max	maximum value
Meas	Measurement
mig	migration
n	negatively charged
o	oxidation
OCV	open circuit potential
p	positively charged

PF6	hexafluorophosphate
r	reduction
RC	resistance and capacitance in parallel
s	solid phase
S	SEI
SEI	SEI phase
tot	total
ε	error function
ω	angular frequency
v	vacancy
+	positively charged
-	negatively charged
0	initial value

Bibliography

[1] R. Korthauer, *Handbuch Lithium-Ionen-Batterien*. Berlin, Heidelberg: Springer Vieweg, 2013.

[2] A. Lewandowski and A. Świderska-Mocek, "Ionic liquids as electrolytes for Li-ion batteries-An overview of electrochemical studies," *Journal of Power Sources*, vol. 194, no. 2, pp. 601–609, 2009.

[3] M. Kilic, M. Bazant, and A. Ajdari, "Steric effects in the dynamics of electrolytes at large applied voltages. I. Double-layer charging," *Physical Review E*, vol. 75, no. 2, p. 021502, 2007.

[4] S. S. Zhang, T. R. Jow, K. Amine, and G. L. Henriksen, "LiPF 6 ±EC±EMC electrolyte for Li-ion battery," *Journal of Power Sources*, vol. 107, pp. 18–23, 2002.

[5] H.-J. Butt and M. Kappl, *Surface and Interfacial Forces*. Weinheim: Wiley-VCH, 2010.

[6] P. Delahay, *Double layer and electrode kinetics*. New York: Interscience Publishers, 1965.

[7] J. Vetter, P. Novák, M. R. Wagner, C. Veit, K. C. Müller, J. O. Besenhard, M. Winter, M. Wohlfahrt-Mehrens, C. Vogler, and A. Hammouche, "Ageing mechanisms in lithium-ion batteries," *Journal of Power Sources*, vol. 147, no. 1-2, pp. 269–281, 2005.

[8] P. Verma, P. Maire, and P. Novák, "A review of the features and analyses of the solid electrolyte interphase in Li-ion batteries," *Electrochimica Acta*, vol. 55, no. 22, pp. 6332–6341, 2010.

[9] R. R. Jaini, B. P. Setzler, A. G. Star, and T. F. Fuller, "Investigating the Solid Electrolyte Interphase Formed by Additive Reduction Using

Physics-Based Modeling," *Journal of The Electrochemical Society*, vol. 163, no. 10, pp. A2185—-A2196, 2016.

[10] P. B. Balbuena and Y. Wang, *Lithium-Ion Batteries - Solid-Electrolyte Interphase*, vol. 1. London: Imperial College Press, 2004.

[11] D. Wang, X. Wu, Z. Wang, and L. Chen, "Cracking causing cyclic instability of LiFePO4 cathode material," *Journal of Power Sources*, vol. 140, no. 1, pp. 125–128, 2005.

[12] Q. Kellner, D. Worwood, A. Barai, W. D. Widanage, and J. Marco, "Duty-cycle characterisation of large-format automotive lithium ion pouch cells for high performance vehicle applications," *Journal of Energy Storage*, vol. 19, no. May, pp. 170–184, 2018.

[13] A. Barré, B. Deguilhem, S. Grolleau, M. Gérard, F. Suard, and D. Riu, "A review on lithium-ion battery ageing mechanisms and estimations for automotive applications," *Journal of Power Sources*, vol. 241, pp. 680–689, 2013.

[14] C. Uhlmann, J. Illig, M. Ender, R. Schuster, and E. Ivers-Tiffée, "In situ detection of lithium metal plating on graphite in experimental cells," *Journal of Power Sources*, vol. 279, pp. 428–438, 2015.

[15] J. N. Illig, *Physically based Impedance Modelling of Lithium-ion Cells*. PhD thesis, ., 2014.

[16] M. E. Orazem and B. Tribollet, *Electrochemical Impedance Spectroscopy*, vol. 48. Hoboken: Wiley, 2008.

[17] E. Barsoukov and J. R. Macdonald, *Impedance Spectroscopy: Theory, Experiment, and Applications*. Hoboken: Wiley, 2005.

[18] N. Harting, N. Wolff, F. Röder, and U. Krewer, "Nonlinear Frequency Response Analysis (NFRA) of Lithium-Ion Batteries," *Electrochimica Acta*, vol. 248, pp. 133–139, 2017.

[19] N. Wolff, N. Harting, F. Röder, M. Heinrich, and U. Krewer, "Understanding nonlinearity in electrochemical systems," *European Physical Journal: Special Topics*, vol. 227, no. 18, 2019.

[20] Y. Xie, J. Li, and C. Yuan, "Mathematical Modeling of the Electrochemical Impedance Spectroscopy in Lithium Ion Battery Cycling," *Electrochimica Acta*, vol. 127, pp. 266–275, 2014.

[21] T. Zavalis, M. Klett, M. Kjell, M. Behm, R. Lindström, and G. Lindbergh, "Aging in Lithium-Ion Batteries: Model and Experimental Investigation of Harvested LiFePO4 and Mesocarbon Microbead Graphite Electrodes," *Electrochimica Acta*, vol. 110, pp. 335–348, 2013.

[22] D. P. Abraham, J. L. Knuth, D. W. Dees, I. Bloom, and J. P. Christophersen, "Performance degradation of high-power lithium-ion cells-Electrochemistry of harvested electrodes," *Journal of Power Sources*, vol. 170, no. 2, pp. 465–475, 2007.

[23] D. Aurbach, B. Markovsky, I. Weissman, E. Levi, and Y. Ein-Eli, "On the Correlation Between Surface Chemistry and Performance of Graphite Negative Electrodes for Li Ion Batteries," *Electrochimica Acta*, vol. 45, no. 1, pp. 67–86, 1999.

[24] A. K. Hjelm and G. Lindbergh, "Experimental and theoretical analysis of LiMn2O4 cathodes for use in rechargeable lithium batteries by electrochemical impedance spectroscopy (EIS)," *Electrochimica Acta*, vol. 47, no. 11, pp. 1747–1759, 2002.

[25] T. Jacobsen and K. West, "Diffusion impedance in planar, cylindrical and spherical symmetry," *Electrochimica Acta*, vol. 40, no. 2, pp. 255–262, 1995.

[26] J. P. Schmidt, P. Berg, M. Schönleber, A. Weber, and E. Ivers-Tiffée, "The distribution of relaxation times as basis for generalized

time-domain models for Li-ion batteries," *Journal of Power Sources*, vol. 221, pp. 70–77, 2013.

[27] P. Vyroubal and T. Kazda, "Equivalent circuit model parameters extraction for lithium ion batteries using electrochemical impedance spectroscopy," *Journal of Energy Storage*, vol. 15, pp. 23–31, 2018.

[28] Q. K. Wang, Y. J. He, J. N. Shen, X. S. Hu, and Z. F. Ma, "State of Charge-Dependent Polynomial Equivalent Circuit Modeling for Electrochemical Impedance Spectroscopy of Lithium-Ion Batteries," *IEEE Transactions on Power Electronics*, vol. 33, no. 10, pp. 8449–8460, 2018.

[29] A. Zaban, E. Zinigrad, and D. Aurbach, "Impedance Spectroscopy of Li Electrodes. 4. A General Simple Model of the Li—Solution Interphase in Polar Aprotic Systems," *The Journal of Physical Chemistry*, vol. 100, no. 8, pp. 3089–3101, 1996.

[30] C. Zou, L. Zhang, X. Hu, Z. Wang, T. Wik, and M. Pecht, "A review of fractional-order techniques applied to lithium-ion batteries, lead-acid batteries, and supercapacitors," *Journal of Power Sources*, vol. 390, no. February, pp. 286–296, 2018.

[31] Y. Zhang, R. Zhao, J. Dubie, T. Jahns, and L. Juang, "Investigation of current sharing and heat dissipation in parallel-connected lithium-ion battery packs," *ECCE 2016 - IEEE Energy Conversion Congress and Exposition, Proceedings*, pp. 1–8, 2016.

[32] J. Schmitt, A. Maheshwari, M. Heck, S. Lux, and M. Vetter, "Impedance change and capacity fade of lithium nickel manganese cobalt oxide-based batteries during calendar aging," *Journal of Power Sources*, vol. 353, pp. 183–194, 2017.

[33] S. Buteau and J. R. Dahn, "Analysis of thousands of electrochemical impedance spectra of lithium-ion cells through a machine learn-

ing inverse model," *Journal of the Electrochemical Society*, vol. 166, no. 8, pp. A1611—-A1622, 2019.

[34] F. Kohlrausch and W. A. Nippoldt, "Über die Gültigkeit der Ohm´schen Gesetze für Electrolyte und eine numerische Bestimmung des Leitungswiderstandes der verdünnten Schwefelsäure durch alternirende Ströme," *Annalen der Physik*, vol. 214, no. 10, pp. 280–289, 1869.

[35] O. Heaviside, *Electromagnetic Theory*. London: Macmillan & Co., 1894.

[36] E. Warburg, "Ueber das Verhalten sogenannter unpolarisirbarer Elektroden gegen Wechselstrom," *Annalen der Physik*, vol. 303, no. 3, pp. 493–499, 1899.

[37] J. E. B. Randles, "Kinetics of rapid electrode reactions," *Discussions of the Faraday Society*, vol. 1, pp. 11–19, 1947.

[38] T. Osaka, D. Mukoyama, and H. Nara, "Review-Development of diagnostic process for commercially available batteries, especially lithium ion battery, by electrochemical impedance spectroscopy," *Journal of the Electrochemical Society*, vol. 162, no. 14, pp. A2529–A2537, 2015.

[39] T. Kalogiannis, M. S. Hosen, M. A. Sokkeh, S. Goutam, J. Jaguemont, L. Jin, G. Qiao, M. Berecibar, and J. Van Mierlo, "Comparative study on parameter identification methods for dual-polarization lithium-ion equivalent circuit model," *Energies*, vol. 12, no. 21, pp. 1–35, 2019.

[40] A. Eddahech, O. Briat, and J. M. Vinassa, "Performance comparison of four lithium-ion battery technologies under calendar aging," *Energy*, vol. 84, pp. 542–550, 2015.

[41] S. Guo, R. Xiong, K. Wang, and F. Sun, "A novel echelon internal heating strategy of cold batteries for all-climate electric vehicles application," *Applied Energy*, vol. 219, no. 5, pp. 256–263, 2018.

[42] T. Stanciu, D. I. Stroe, R. Teodorescu, and M. Swierczynski, "Extensive EIS characterization of commercially available lithium polymer battery cell for performance modelling," *2015 17th European Conference on Power Electronics and Applications, EPE-ECCE Europe 2015*, pp. 1–10, 2015.

[43] C. Fleischer, W. Waag, H. M. Heyn, and D. U. Sauer, "On-line adaptive battery impedance parameter and state estimation considering physical principles in reduced order equivalent circuit battery models: Part 1. Requirements, critical review of methods and modeling," *Journal of Power Sources*, vol. 260, pp. 276–291, 2014.

[44] R. Raccichini, M. Amores, and G. Hinds, "Critical Review of the Use of Reference Electrodes in Li-Ion Batteries: A Diagnostic Perspective," *Batteries*, vol. 5, no. 1, p. 12, 2019.

[45] B. Stiaszny, J. C. Ziegler, E. E. Krauß, J. P. Schmidt, and E. Ivers-Tiffée, "Electrochemical characterization and post-mortem analysis of aged LiMn 2O4-Li(Ni0.5Mn0.3Co 0.2)O2/graphite lithium ion batteries. Part I: Cycle aging," *Journal of Power Sources*, vol. 251, pp. 439–450, 2014.

[46] F. Dion and A. Lasia, "The use of regularization methods in the deconvolution of underlying distributions in electrochemical processes," *Journal of Electroanalytical Chemistry*, vol. 475, no. 1, pp. 28–37, 1999.

[47] S. Rodrigues, N. Munichandraiah, and A. K. Shukla, "AC impedance and state-of-charge analysis of a sealed lithium-ion rechargeable battery," *Journal of Solid State Electrochemistry*, vol. 3, no. 7-8, pp. 397–405, 1999.

[48] Q. A. Huang, Y. Shen, Y. Huang, L. Zhang, and J. Zhang, "Impedance Characteristics and Diagnoses of Automotive Lithium-Ion Batteries at 7.5% to 93.0% State of Charge," *Electrochimica Acta*, vol. 219, pp. 751–765, 2016.

[49] R. Xiong, J. Tian, H. Mu, and C. Wang, "A systematic model-based degradation behavior recognition and health monitoring method for lithium-ion batteries," *Applied Energy*, vol. 207, pp. 372–383, 2017.

[50] J. Huang, Z. Li, and J. Zhang, "Dynamic electrochemical impedance spectroscopy reconstructed from continuous impedance measurement of single frequency during charging/discharging," *Journal of Power Sources*, vol. 273, pp. 1098–1102, 2015.

[51] S. E. Li, B. Wang, H. Peng, and X. Hu, "An electrochemistry-based impedance model for lithium-ion batteries," *Journal of Power Sources*, vol. 258, pp. 9–18, 2014.

[52] J. Huang, Z. Li, B. Y. Liaw, and J. Zhang, "Graphical analysis of electrochemical impedance spectroscopy data in Bode and Nyquist representations," *Journal of Power Sources*, vol. 309, pp. 82–98, 2016.

[53] S. Buller, *Impedance-Based Simulation Models for Energy Storage Devices in Advanced Automotive Power Systems*. Shaker Verlag GmbH, 2003.

[54] M. Oldenburger, B. Bedürftig, A. Gruhle, F. Grimsmann, E. Richter, R. Findeisen, and A. Hintennach, "Investigation of the low frequency Warburg impedance of Li-ion cells by frequency domain measurements," *Journal of Energy Storage*, vol. 21, no. December 2018, pp. 272–280, 2019.

[55] J. Song and M. Z. Bazant, "Effects of Nanoparticle Geometry and Size Distribution on Diffusion Impedance of Battery Electrodes,"

Journal of The Electrochemical Society, vol. 160, pp. A15—-A24, nov 2013.

[56] J. Song and M. Z. Bazant, "Electrochemical Impedance of a Battery Electrode with Anisotropic Active Particles," *Electrochimica Acta*, vol. 131, pp. 214–227, 2014.

[57] N. Legrand, S. Raël, B. Knosp, M. Hinaje, P. Desprez, and F. Lapicque, "Including double-layer capacitance in lithium-ion battery mathematical models," *Journal of Power Sources*, vol. 251, pp. 370–378, 2014.

[58] J. Huang, Z. Li, J. Zhang, S. Song, Z. Lou, and N. Wu, "An Analytical Three-Scale Impedance Model for Porous Electrode with Agglomerates in Lithium-Ion Batteries," *Journal of The Electrochemical Society*, vol. 162, no. 4, pp. A585–A595, 2015.

[59] J. B. Robinson, J. A. Darr, D. S. Eastwood, G. Hinds, P. D. Lee, P. R. Shearing, O. O. Taiwo, and D. J. Brett, "Non-uniform temperature distribution in Li-ion batteries during discharge - A combined thermal imaging, X-ray micro-tomography and electrochemical impedance approach," *Journal of Power Sources*, vol. 252, pp. 51–57, 2014.

[60] S. P. Rangarajan, Y. Barsukov, and P. P. Mukherjee, "In operando impedance based diagnostics of electrode kinetics in Li-ion pouch cells," *Journal of the Electrochemical Society*, vol. 166, no. 10, pp. A2131–A2141, 2019.

[61] R. Premanand, A. Durairajan, B. Haran, R. White, and B. Popov, "Studies on Capacity Fade of Spinel-Based Li-Ion Batteries," *Journal of The Electrochemical Society*, vol. 149, no. 1, p. A54, 2000.

[62] T. Osaka, S. Nakade, M. Rajamäki, and T. Momma, "Influence of capacity fading on commercial lithium-ion battery impedance," *Journal of Power Sources*, vol. 119-121, pp. 929–933, 2003.

[63] M. Doyle, J. P. Meyers, and J. Newman, "Computer Simulations of the Impedance Response of Lithium Rechargeable Batteries," *Journal of The Electrochemical Society*, vol. 147, no. 1, p. 99, 2000.

[64] G. Ning and B. N. Popov, "Cycle Life Modeling of Lithium-Ion Batteries," *Journal of The Electrochemical Society*, vol. 151, no. 10, p. A1584, 2004.

[65] K. a. Smith, C. D. Rahn, and C. Y. Wang, "Control oriented 1D electrochemical model of lithium ion battery," *Energy Conversion and Management*, vol. 48, no. 9, pp. 2565–2578, 2007.

[66] S. Tippmann, D. Walper, L. Balboa, B. Spier, and W. G. Bessler, "Low-temperature charging of lithium-ion cells part I: Electrochemical modeling and experimental investigation of degradation behavior," *Journal of Power Sources*, vol. 252, pp. 305–316, 2014.

[67] Y. Tao, J. Ye, X. Li, Q. Zhang, A. Pan, Q. Liao, and X. Yang, "Ageing study of 26650 type li-ion batteries module at the charge-discharge rates of 1 C," *AIP Conference Proceedings*, vol. 2154, no. September, 2019.

[68] Y. Olofsson, J. Groot, T. Katrašnik, and G. Tavčar, "Impedance spectroscopy characterisation of automotive NMC/graphite Li-ion cells aged with realistic PHEV load profile," *2014 IEEE International Electric Vehicle Conference, IEVC 2014*, 2015.

[69] J. Christensen and J. Newman, "A Mathematical Model for the Lithium-Ion Negative Electrode Solid Electrolyte Interphase," *Journal of The Electrochemical Society*, vol. 151, no. 11, p. A1977, 2004.

[70] A. Colclasure, K. Smith, and R. Kee, "Modeling Detailed Chemistry and Transport for Solid-Electrolyte-Interface (SEI) Films in Li-Ion Batteries," *Electrochimica Acta*, vol. 58, no. 1, pp. 33–43, 2011.

[71] M. Heinrich, N. Wolff, N. Harting, V. Laue, F. Röder, S. Seitz, and U. Krewer, "Physico-Chemical Modeling of a Lithium-Ion Battery: An Ageing Study with Electrochemical Impedance Spectroscopy," *Batteries & Supercaps*, vol. 2, no. 2, pp. 530–540, 2019.

[72] S. Dobre, T. Bastogne, and A. Richard, *Global sensitivity and identifiability implications in systems biology*, vol. 11. IFAC, 2010.

[73] J. A. Jacquez and T. Perry, "Parameter estimation: Local identifiability of parameters," *American Journal of Physiology - Endocrinology and Metabolism*, vol. 258, no. 4 21-4, pp. 727–736, 1990.

[74] J. Morio, "Global and local sensitivity analysis methods for a physical system," *European Journal of Physics*, vol. 32, no. 6, pp. 1577–1583, 2011.

[75] J. C. Forman, S. J. Moura, J. L. Stein, and H. K. Fathy, "Genetic parameter identification of the Doyle-Fuller-Newman model from experimental cycling of a LiFePO4 battery," *Proceedings of the 2011 American Control Conference*, pp. 362–369, 2011.

[76] J. C. Forman, S. J. Moura, J. L. Stein, and H. K. Fathy, "Genetic identification and fisher identifiability analysis of the Doyle-Fuller-Newman model from experimental cycling of a LiFePO4cell," *Journal of Power Sources*, vol. 210, pp. 263–275, 2012.

[77] X. Lin and A. G. Stefanopoulou, "Analytic Bound on Accuracy of Battery State and Parameter Estimation," *Journal of the Electrochemical Society*, vol. 162, no. 9, pp. A1879–A1891, 2015.

[78] S. Mendoza, M. Rothenberger, A. Hake, and H. Fathy, "Optimization and experimental validation of a thermal cycle that maximizes entropy coefficient fisher identifiability for lithium iron phosphate cells," *Journal of Power Sources*, vol. 308, pp. 18–28, 2016.

[79] S. Mendoza, M. Rothenberger, J. Liu, and H. K. Fathy, "Maximizing Parameter Identifiability of a Combined Thermal and Electrochemical Battery Model Via Periodic Current Input Optimization," *IFAC-PapersOnLine*, vol. 50, no. 1, pp. 7314–7320, 2017.

[80] A. P. Schmidt, M. Bitzer, Á. W. Imre, and L. Guzzella, "Experiment-driven electrochemical modeling and systematic parameterization for a lithium-ion battery cell," *Journal of Power Sources*, vol. 195, no. 15, pp. 5071–5080, 2010.

[81] A. Sharma and H. K. Fathy, "Fisher identifiability analysis for a periodically-excited equivalent-circuit lithium-ion battery model," *Proceedings of the American Control Conference*, pp. 274–280, 2014.

[82] M. J. Rothenberger, J. Anstrom, S. Brennan, and H. K. Fathy, "Maximizing Parameter Identifiability of an Equivalent-Circuit Battery Model Using Optimal Periodic Input Shaping," *ASME 2014 Dynamic Systems and Control Conference*, p. V001T19A004, 2014.

[83] M. J. Rothenberger, D. J. Docimo, M. Ghanaatpishe, and H. K. Fathy, "Genetic optimization and experimental validation of a test cycle that maximizes parameter identifiability for a Li-ion equivalent-circuit battery model," *Journal of Energy Storage*, vol. 4, pp. 156–166, 2015.

[84] M. Joshi, A. Seidel-Morgenstern, and A. Kremling, "Exploiting the bootstrap method for quantifying parameter confidence intervals in dynamical systems," *Metabolic Engineering*, vol. 8, no. 5, pp. 447–455, 2006.

[85] R. Schenkendorf, X. Xie, M. Rehbein, S. Scholl, and U. Krewer, "The impact of global sensitivities and design measures in model-based optimal experimental design," *Processes*, vol. 6, no. 4, 2018.

[86] L. Ljung, *Ljung L System Identification: Theory for User*, vol. 25. New Jersey: Prentice-hall, 1987.

[87] T. McWhorter and L. L. Scharf, "Cramer-Rao Bounds for Deterministic Modal Analysis," *IEEE Transactions on Signal Processing*, vol. 41, no. 5, pp. 1847–1866, 1993.

[88] M. D. Levi and D. Aurbach, "Simultaneous Measurements and Modeling of the Electrochemical Impedance and the Cyclic Voltammetric Characteristics of Graphite Electrodes Doped with Lithium," *The Journal of Physical Chemistry B*, vol. 101, no. 23, pp. 4630–4640, 1997.

[89] R. W. J. M. Huang, F. Chung, and E. M. Kelder, "Impedance Simulation of a Li-Ion Battery with Porous Electrodes and Spherical Li+ Intercalation Particles," *Journal of The Electrochemical Society*, vol. 153, no. 8, p. A1459, 2006.

[90] G. Sikha and R. E. White, "Analytical Expression for the Impedance Response for a Lithium-Ion Cell," *Journal of the Electrochemical Society*, vol. 155, no. 12, pp. A893–A902, 2008.

[91] P. Shafiei Sabet and D. U. Sauer, "Separation of predominant processes in electrochemical impedance spectra of lithium-ion batteries with nickel–manganese–cobalt cathodes," *Journal of Power Sources*, vol. 425, pp. 121–129, 2019.

[92] P. Shafiei Sabet, G. Stahl, and D. U. Sauer, "Non-invasive investigation of predominant processes in the impedance spectra of high energy lithium-ion batteries with Nickel-Cobalt-Aluminum cathodes," *Journal of Power Sources*, vol. 406, pp. 185–193, 2018.

[93] S. Schindler and M. A. Danzer, "Influence of cell design on impedance characteristics of cylindrical lithium-ion cells: A model-based assessment from electrode to cell level," *Journal of Energy Storage*, vol. 12, pp. 157–166, 2017.

[94] A. S. Mussa, A. Liivat, F. Marzano, M. Klett, B. Philippe, C. Tengstedt, G. Lindbergh, K. Edström, R. W. Lindström, and P. Svens,

"Fast-charging effects on ageing for energy-optimized automotive LiNi 1/3 Mn 1/3 Co 1/3 O 2 /graphite prismatic lithium-ion cells," *Journal of Power Sources*, vol. 422, pp. 175–184, 2019.

[95] M. Guo, W. Meng, X. Zhang, X. Liu, Z. Bai, S. Chen, Z. Wang, and F. Yang, "Electrochemical behavior and self-organization of porous Sn nanocrystals@acetylene black microspheres in lithium-ion half cells," *Applied Surface Science*, vol. 470, pp. 36–43, 2019.

[96] J. Illig, T. Chrobak, M. Ender, J. Schmidt, D. Klotz, and E. Ivers-Tiffée, "Studies on LiFePO 4 as cathode material in Li-ion batteries," *ECS Transactions*, vol. 28, no. 30, pp. 3–17, 2010.

[97] B. Tong, J. Wang, Z. Liu, L. Ma, Z. Zhou, and Z. Peng, "Identifying compatibility of lithium salts with LiFePO4 cathode using a symmetric cell," *Journal of Power Sources*, vol. 384, pp. 80–85, 2018.

[98] K. Kisu, S. Aoyagi, H. Nagatomo, E. Iwama, M. T. H. Reid, W. Naoi, and K. Naoi, "Internal resistance mapping preparation to optimize electrode thickness and density using symmetric cell for high-performance lithium-ion batteries and capacitors," *Journal of Power Sources*, vol. 396, pp. 207–212, 2018.

[99] J. Conder, C. Villevieille, S. Trabesinger, P. Novák, L. Gubler, and R. Bouchet, "Electrochemical impedance spectroscopy of a Li–S battery: Part 1. Influence of the electrode and electrolyte compositions on the impedance of symmetric cells," *Electrochimica Acta*, vol. 244, pp. 61–68, 2017.

[100] R. Petibon, N. N. Sinha, J. C. Burns, C. P. Aiken, H. Ye, C. M. Vanelzen, G. Jain, S. Trussler, and J. R. Dahn, "Comparative study of electrolyte additives using electrochemical impedance spectroscopy on symmetric cells," *Journal of Power Sources*, vol. 251, pp. 187–194, 2014.

[101] C. H. Chen, J. Liu, and K. Amine, "Symmetric cell approach and impedance spectroscopy of high power lithium-ion batteries," *Journal of Power Sources*, vol. 96, no. 2, pp. 321–328, 2001.

[102] D. P. Abraham, S. D. Poppen, A. N. Jansen, J. Liu, and D. W. Dees, "Application of a lithium-tin reference electrode to determine electrode contributions to impedance rise in high-power lithium-ion cells," *Electrochimica Acta*, vol. 49, no. 26, pp. 4763–4775, 2004.

[103] H. Nara, D. Mukoyama, T. Yokoshima, T. Momma, and T. Osaka, "Impedance Analysis with Transmission Line Model for Reaction Distribution in a Pouch Type Lithium-Ion Battery by Using Micro Reference Electrode," *Journal of The Electrochemical Society*, vol. 163, no. 3, pp. A434–A441, 2016.

[104] J. L. Gómez-Cámer and P. Novák, "Electrochemical impedance spectroscopy: Understanding the role of the reference electrode," *Electrochemistry Communications*, vol. 34, pp. 208–210, 2013.

[105] M. Dondelinger, J. Swanson, G. Nasymov, C. Jahnke, Q. Qiao, J. Wu, C. Widener, A. M. Numan-Al-Mobin, and A. Smirnova, "Electrochemical stability of lithium halide electrolyte with antiperovskite crystal structure," *Electrochimica Acta*, vol. 306, pp. 498–505, 2019.

[106] L. H. J. Raijmakers, M. J. G. Lammers, and P. H. L. Notten, "A new method to compensate impedance artefacts for Li-ion batteries with integrated micro-reference electrodes," *Electrochimica Acta*, vol. 259, pp. 517–533, 2018.

[107] Y. Troxler, B. Wu, M. Marinescu, V. Yufit, Y. Patel, A. J. Marquis, N. P. Brandon, and G. J. Offer, "The effect of thermal gradients on the performance of lithium-ion batteries," *Journal of Power Sources*, vol. 247, pp. 1018–1025, 2014.

[108] O. S. Burheim, M. a. Onsrud, J. G. Pharoah, F. Vullum-Bruer, and P. J. S. Vie, "Thermal Conductivity, Heat Sources and Tempera-

ture Profiles of Li-Ion Batteries," *ECS Transactions*, vol. 58, no. 48, pp. 145–171, 2014.

[109] F. Richter, P. J. Vie, S. Kjelstrup, and O. S. Burheim, "Measurements of ageing and thermal conductivity in a secondary NMC-hard carbon Li-ion battery and the impact on internal temperature profiles," *Electrochimica Acta*, vol. 250, pp. 228–237, 2017.

[110] T. Kaplan, L. J. Gray, and S. H. Liu, "Self-affine fractal model for a metal-electrolyte interface," *Physical Review B*, vol. 35, no. 10, pp. 5–7, 1987.

[111] S. H. Ahmed and S. O. Bade Shrestha, "Temperature Dependence of Double Layer Capacitance in Lithium-Ion Battery," *Proceedings of the 116th IIER International Conference*, no. 9, pp. 7–10, 2017.

[112] N. Wolff, N. Harting, M. Heinrich, F. Röder, and U. Krewer, "Nonlinear Frequency Response Analysis on Lithium-Ion Batteries: A Model-Based Assessment," *Electrochimica Acta*, vol. 260, pp. 614–622, 2018.

[113] M. Doyle, F. Fuller, and J. Newman, "Modeling of Galvanostatic Charge and Discharge of the Lithium/Polymer/Insertion Cell," *Journal of The Electrochemical Society*, vol. 140, no. 6, p. 1526, 1993.

[114] I. Ong and J. Newman, "Double-Layer Capacitance in a Dual Lithium Ion Insertion Cell," *Journal of The Electrochemical Society*, vol. 146, no. 12, p. 4360, 1999.

[115] E. Peled, D. Golodnitsky, G. Ardel, and V. Eshkenazy, "The SEI Model - Application to Lithium Polymer Electrolyte Batteries," *Electrochimica Acta*, vol. 40, no. 13-14, pp. 2197–2204, 1995.

[116] L. Gao and D. Macdonald, "Characterization of Irreversible Processes at the

Li/Poly[bis(2,3di(2Methoxyethoxy)Propoxy)Phosphazene] Interface on Charge Cycling," *Journal of The Electrochemical Society*, vol. 144, no. 4, pp. 1174–1179, 1997.

[117] D. Macdonald, "The Point Defect Model for the Passive State," *Journal of The Electrochemical Society*, vol. 139, no. 12, p. 3434, 1992.

[118] I. Nainville, A. Lemarchand, and J. P. Badiali, "Passivation of a Lithium Anode: A Simulation Model," *Electrochimica Acta*, vol. 41, no. 18, pp. 2855–2863, 1996.

[119] M. Broussely, S. Herreyre, P. Biensan, P. Kasztejna, K. Nechev, and R. J. Staniewicz, "Aging Mechanism in Li Ion Cells and Calendar Life Predictions," *Journal of Power Sources*, vol. 97-98, pp. 13–21, 2001.

[120] P. Ramadass, B. Haran, R. White, and B. N. Popov, "Mathematical modeling of the capacity fade of Li-ion cells," *Journal of Power Sources*, vol. 123, no. 2, pp. 230–240, 2003.

[121] P. Ramadass, B. Haran, P. M. Gomadam, R. White, and B. N. Popov, "Development of First Principles Capacity Fade Model for Li-Ion Cells," *Journal of The Electrochemical Society*, vol. 151, no. 2, p. A196, 2004.

[122] A. Colclasure and R. Kee, "Thermodynamically Consistent Modeling of Elementary Electrochemistry in Lithium-Ion Batteries," *Electrochimica Acta*, vol. 55, no. 28, pp. 8960–8973, 2010.

[123] F. Röder, R. D. Braatz, and U. Krewer, "Multi-Scale Simulation of Heterogeneous Surface Film Growth Mechanisms in Lithium-Ion Batteries," *Journal of The Electrochemical Society*, vol. 164, no. 11, pp. E3335–E3344, 2017.

[124] G. Lenze, F. Röder, H. Bockholt, W. Haselrieder, A. Kwade, and U. Krewer, "Simulation-Supported Analysis of Calendering Im-

pacts on the Performance of Lithium-Ion-Batteries," *Journal of The Electrochemical Society*, vol. 164, no. 6, pp. A1223–A1233, 2017.

[125] J. P. Meyers, M. Doyle, R. M. Darling, and J. Newman, "The Impedance Response of a Porous Electrode Composed of Intercalation Particles," *Journal of The Electrochemical Society*, vol. 147, no. 8, p. 2930, 2000.

[126] J. Newman and K. E. Thomas-Alyea, *Electrochemical Systems*. Electrochemical Society series, Hoboken: John Wiley & Sons, 2004.

[127] M. R. Busche, T. Drossel, T. Leichtweiss, D. A. Weber, M. Falk, M. Schneider, M. L. Reich, H. Sommer, P. Adelhelm, and J. Janek, "Dynamic formation of a solid-liquid electrolyte interphase and its consequences for hybrid-battery concepts," *Nature Chemistry*, vol. 8, no. 5, pp. 426–434, 2016.

[128] Y. Yamada, F. Sagane, Y. Iriyama, T. Abe, and Z. Ogumi, "Kinetics of Lithium-Ion Transfer at the Interface between Li0.35La0.55TiO3 and Binary Electrolytes," *Journal of Physical Chemistry C*, vol. 113, pp. 14528–14532, 2009.

[129] F. G. Helfferich, *Comprehensive Chemical Kinetics - Kinetics of Homogeneous Multistep Reactions*. London: Elsevier, 38 ed., 2001.

[130] Y. Kitazumi, O. Shirai, M. Yamamoto, and K. Kano, "A model of the potential-dependent adsorption of charged redox-active species at the electrode surface," *Electrochimica Acta*, vol. 259, pp. 542–551, 2018.

[131] P. Arora, R. E. White, and M. Doyle, "Capacity Fade Mechanisms and Side Reactions in Lithium-Ion Batteries," *Journal of The Electrochemical Society*, vol. 145, no. 10, p. 3647, 1998.

[132] M. Broussely, P. Biensan, F. Bonhomme, P. Blanchard, S. Herreyre, K. Nechev, and R. J. Staniewicz, "Main Aging Mechanisms in Li

Ion Batteries," *Journal of Power Sources*, vol. 146, no. 1-2, pp. 90–96, 2005.

[133] M. Koltypin, D. Aurbach, L. Nazar, and B. Ellis, "More on the Performance of LiFePO4 Electrodes - The Effect of Synthesis Route, Solution Composition, Aging, and Temperature," *Journal of Power Sources*, vol. 174, no. 2, pp. 1241–1250, 2007.

[134] U. Tröltzsch, O. Kanoun, and H. R. Tränkler, "Characterizing aging effects of lithium ion batteries by impedance spectroscopy," *Electrochimica Acta*, vol. 51, no. 8-9, pp. 1664–1672, 2006.

[135] S. M. Alavi, C. R. Birkl, and D. a. Howey, "Time-domain fitting of battery electrochemical impedance models," *Journal of Power Sources*, vol. 288, pp. 345–352, 2015.

[136] J. Illig, J. P. Schmidt, M. Weiss, A. Weber, and E. Ivers-Tiffée, "Understanding the impedance spectrum of 18650 LiFePO4-cells," *Journal of Power Sources*, vol. 239, pp. 670–679, 2013.

[137] C. Gabrielli, "Identification of electrochemical processes by frequency response analysis," Tech. Rep. 004/84, ., 1984.

[138] A. Andersson, A. Henningson, H. Siegbahn, U. Jansson, and K. Edström, "Electrochemically Lithiated Graphite Characterised by Photoelectron Spectroscopy," *Journal of Power Sources*, vol. 119-121, pp. 522–527, 2003.

[139] M. Nie, D. Chalasani, D. Abraham, Y. Chen, A. Bose, and B. Lucht, "Lithium Ion Battery Graphite Solid Electrolyte Interphase Revealed by Microscopy and Spectroscopy," *The Journal of Physical Chemistry C*, vol. 117, no. 3, pp. 1257–1267, 2013.

[140] S. Shi, Y. Qi, H. Li, and L. Hector, "Defect Thermodynamics and Diffusion Mechanisms in Li2CO3 and Implications for the Solid Electrolyte Interphase in Li-Ion Batteries," *Journal of Physical Chemistry C*, vol. 117, no. 17, pp. 8579–8593, 2013.

[141] T. P. Heins, N. Schlüter, and U. Schröder, "Electrode-Resolved Monitoring of the Ageing of Large-Scale Lithium-Ion Cells by using Electrochemical Impedance Spectroscopy," *ChemElectroChem*, vol. 4, no. 11, pp. 2921–2927, 2017.

[142] T. P. Heins, N. Harms, L. Schramm, and U. Schröder, "Development of a new Electrochemical Impedance Spectroscopy Approach for Monitoring the Solid Electrolyte Interphase Formation," *Energy Technology*, vol. 4, pp. 1–6, 2016.

[143] G. Sikha, B. N. Popov, and R. E. White, "Effect of Porosity on the Capacity Fade of a Lithium-Ion Battery," *Journal of The Electrochemical Society*, vol. 151, no. 7, p. A1104, 2004.

[144] R. Fu, S. Y. Choe, V. Agubra, and J. Fergus, "Modeling of degradation effects considering side reactions for a pouch type Li-ion polymer battery with carbon anode," *Journal of Power Sources*, vol. 261, pp. 120–135, 2014.

[145] D. Aurbach, M. D. Levi, E. Levi, and A. Schechter, "Failure and Stabilization Mechanisms of Graphite Electrodes," *The Journal of Physical Chemistry B*, vol. 101, no. 12, pp. 2195–2206, 1997.

[146] L. Shi and U. Kunz, "Mechanical Behavior during Electrochemical and Mechanical Deactivation of an Aged Electrode in a Lithium-Ion Pouch Cell," *Energy Technology*, vol. 4, no. 12, pp. 1520–1530, 2016.

[147] F. Ciucci, T. Carraro, W. C. Chueh, and W. Lai, "Reducing error and measurement time in impedance spectroscopy using model based optimal experimental design," *Electrochimica Acta*, vol. 56, no. 15, pp. 5416–5434, 2011.

[148] F. Ciucci, "Revisiting parameter identification in electrochemical impedance spectroscopy: Weighted least squares and optimal experimental design," *Electrochimica Acta*, vol. 87, pp. 532–545, 2013.

11 Appendix

11.1 Effect of the Time Constants on the Impedance of a double RC-Element

The internal resistance $R_i = 0.015\ \Omega$. The resistance of the charge transfer reactions for the anode $R_{ct,a} = 0.0012\ \Omega$ and for the cathode $R_{ct,a} = 0.0012\ \Omega$. At the anode the double layer capacitance $C_a^{DL} = 1$ F. All these parameters stay constant for all three simulations. The double layer capacitance of the cathode C_c^{DL} changes from 1 to 0.1 to 0.01 in order to deviate the time constants by the respective factor. Now the frequency dependent impedance can be calculated in accordance to:

$$Z(f) = R_i + \frac{R_a}{1 + 2\pi f i C_a R_a} + \frac{R_c}{1 + 2\pi f i C_c R_c} \tag{11.1}$$

With i being the imaginary unit.

11.2 Anode Redlich-Kister Parameters

B_1:	-35.80	B_7:	-28.79
B_2:	-35.01	B_8:	-14.98
B_3:	-35.25	B_9:	-39.91
B_4:	-35.69	B_{10}:	-96.17
B_5:	-38.63	B_{11}:	-63.26
B_6:	-35.91		

Table 11.1: Redlich-Kister parameters in kJ mol^{-1} [70]

11.3 Matlab Code for FIM Simulations

```
% ---------------
% FIM Calculation
% ---------------
```

```
clear all;
close all;
clc;

load('MeasMatrix000.mat'); %load measurement data
fExp = MeasMatrix000(:,1); %frequencies used in the experiment
ReZOhm = MeasMatrix000(:,2).*cos(MeasMatrix000(:,3),...
.*((2*pi)/360)); % calculate real part from magnitude
ImZOhm = MeasMatrix000(:,2).*sin(MeasMatrix000(:,3),...
.*((2*pi)/360)); % calculate imaginary part from magnitude
```

Uncertainty

```
% measurement uncertainty of the absolute value
% and phase of the impedance
sigma_Z = 0.002/28.39*15;
%given by the manufacturer of the measurement device
sigma_theta = 0.1*2*pi/360;
%given by the manufacturer of the measurement device

% uncertainty of the real part and
% the imaginary part of the impedance
variance_Re = (sigma_Z*cos(MeasMatrix000(:,3).*2*pi/360)),...
.2+(sigma_theta*sin(MeasMatrix000(:,3).*2*pi/360),...
.*MeasMatrix000(:,2)).2;
variance_Im = (sigma_Z*sin(MeasMatrix000(:,3).*2*pi/360)),...
.2+(sigma_theta*cos(MeasMatrix000(:,3),...
.*2*pi/360).*MeasMatrix000(:,2)).2;

% standard deviations
sigma_Re = sqrt(mean(variance_Re));
sigma_Im = sqrt(mean(variance_Im));
```

Parameter

```
capMeas = 28.39; % capcity of the battery

% initial values for the parameters to be identified
CapInFit = -1.07625980671179e-07;
conFit = 9.11999223134431;
AdsFit = 1.02622969811620;
ElFit = [1.57645948620546 4.43575923226899,...
1.39710182519778 0.859748438279257];
CircFit = 0;
RestFit = [0 0];

% parameterisation of the battery model
par = parametersetMobile4e_Fit_to_MeasVarArgInSEI,...
(conFit,AdsFit,ElFit,CircFit,RestFit);

% parameter of interest to normalise results
par_norm = [par.kc par.k_f_SEI par.k_f_Ads par.C_DL_a,...
par.C_DL_Ads par.C_DL_c par.SEIcon];
```

Parameter set

```
% initialization
parameterset = zeros(7,14);
% reaction rate cathode
parameterset(:,1) = par_norm(1)*ones(7,1);
parameterset(:,8) = par_norm(1)*ones(7,1);
parameterset(1,1) = par_norm(1)*(1+0.05/100);
parameterset(1,8) = par_norm(1)*(1-0.05/100);
% reaction rate SEI
parameterset(:,2) = par_norm(2)*ones(7,1);
parameterset(:,9) = par_norm(2)*ones(7,1);
```

```
parameterset(2,2) = par_norm(2)*(1+0.05/100);
parameterset(2,9) = par_norm(2)*(1-0.05/100);
% reaction rate IFA
parameterset(:,3) = par_norm(3)*ones(7,1);
parameterset(:,10) = par_norm(3)*ones(7,1);
parameterset(3,3) = par_norm(3)*(1+0.05/100);
parameterset(3,10) = par_norm(3)*(1-0.05/100);
% double layer capacity anode
parameterset(:,4) = par_norm(4)*ones(7,1);
parameterset(:,11) = par_norm(4)*ones(7,1);
parameterset(4,4) = par_norm(4)*(1+0.05/100);
parameterset(4,11) = par_norm(4)*(1-0.05/100);
% double layer capacity IFA
parameterset(:,5) = par_norm(5)*ones(7,1);
parameterset(:,12) = par_norm(5)*ones(7,1);
parameterset(5,5) = par_norm(5)*(1+0.05/100);
parameterset(5,12) = par_norm(5)*(1-0.05/100);
% double layer capacity cathode
parameterset(:,6) = par_norm(6)*ones(7,1);
parameterset(:,13) = par_norm(6)*ones(7,1);
parameterset(6,6) = par_norm(6)*(1+0.05/100);
parameterset(6,13) = par_norm(6)*(1-0.05/100);
% SEI layer conductivity
parameterset(:,7) = par_norm(7)*ones(7,1);
parameterset(:,14) = par_norm(7)*ones(7,1);
parameterset(7,7) = par_norm(7)*(1+0.05/100);
parameterset(7,14) = par_norm(7)*(1-0.05/100);
```

FIM Calculation

```
for i = 1:7
% right variation of variable
par.kc = parameterset(i,1);
```

```
par.k_f_SEI = parameterset(i,2);
par.k_f_Ads = parameterset(i,3);
par.C_DL_a = parameterset(i,4);
par.C_DL_Ads = parameterset(i,5);
par.C_DL_c = parameterset(i,6);
par.SEIcon = parameterset(i,7);

% SP battery model is solved an parameters identified
y_r = sim_SP_thermIfSEI(par,fExp,0,1,0,1,CapInFit,capMeas);
X_Start = y_r.Y(end,:);
y_r = sim_SP_thermIfSEI,...
(par,fExp,1/15,2,X_Start,1,CapInFit,capMeas);

% left variation of variable
par.kc = parameterset(i,8);
par.k_f_SEI = parameterset(i,9);
par.k_f_Ads = parameterset(i,10);
par.C_DL_a = parameterset(i,11);
par.C_DL_Ads = parameterset(i,12);
par.C_DL_c = parameterset(i,13);
par.SEIcon = parameterset(i,14);

% SP battery model is solved an parameters identified
y_l = sim_SP_thermIfSEI(par,fExp,0,1,0,1,CapInFit,capMeas);
X_Start = y_l.Y(end,:);
y_l = sim_SP_thermIfSEI,...
(par,fExp,1/15,2,X_Start,1,CapInFit,capMeas);

% sensitivity of real and imagine part
a(i,:) = (y_r.real(:,1)-y_l.real(:,1))/(2*0.05/100);
b(i,:) = (y_r.imagine(:,1)-y_l.imagine(:,1))/(2*0.05/100);
end
```

```
FIM = zeros(7,7); %initialisation of the vector

for j=1:67
%calculate the FIM
FIM=FIM+(a(:,j)*a(:,j)')/sigma_Re2+(b(:,j)*b(:,j)')/sigma_Im2;
end

% Cramer-Rao inequality und covariance matrix calculation
covmatrix = FIM\eye(7,7);
% relative, absolute standard deviation and error of parameters
sigma = sqrt(diag(covmatrix));
sigma_absoulte = sigma.*par_norm';
error = 3*sigma;

% korrelation coefficient caculation
for ii = 1:7
for jj = 1:7
rou(ii,jj) =,...
covmatrix(ii,jj)/sqrt(covmatrix(ii,ii)*covmatrix(jj,jj));
end
end
```